Lehigh University
Lehigh Preserve

Theses and Dissertations

2012

A Study of the Electrical Polarizability of Colloidal Particles in Liquid Suspensions

Jingyu Wang
Lehigh University

Follow this and additional works at: http://preserve.lehigh.edu/etd

Recommended Citation
Wang, Jingyu, "A Study of the Electrical Polarizability of Colloidal Particles in Liquid Suspensions" (2012). *Theses and Dissertations.* Paper 1096.

This Dissertation is brought to you for free and open access by Lehigh Preserve. It has been accepted for inclusion in Theses and Dissertations by an authorized administrator of Lehigh Preserve. For more information, please contact preserve@lehigh.edu.

A Study of the Electrical Polarizability of Colloidal Particles in Liquid Suspensions

by

Jingyu Wang

A Dissertation

Presented to the Graduate and Research Committee

of Lehigh University

in Candidacy for the Degree of

Doctor of Philosophy

in

Department of Physics

Lehigh University

August 5th 2012

© 2012 Copyright
Jingyu Wang

Approved and recommended for acceptance as a dissertation in partial fulfillment of the requirements for the degree of Doctor of Philosophy

Jingyu Wang
A Study of the Electrical Polarizability of Colloidal Particles in Liquid Suspensions

_____

May 9th, 2012

_____

Dissertation Director

_____

Approved Date

Committee Members:

_____

Dr. H. Daniel Ou-Yang

_____

Dr. Volkmar Dierolf

_____

Dr. Arnold H. Kritz

_____

Dr. Dimitrios Vavylonis

_____

Dr. James F. Gilchrist

TABLE OF CONTENTS

List of figures vii
Abstract 1
1 Introduction 2
1.1 Electric double layer models 2
1.2 Thickness of double layer 5
1.3 Double layer movement outside colloidal particles 6
1.4 Double layer movement above planar conductive electrodes 7
1.5 Polarization of double layer 9
1.6 E^2-dependent AC electrokinetics 10
1.6.1 Dielectrophoresis 11
1.6.2 AC electroosmosis 12
1.7 Polarization of rods 13
1.8 Structure of this thesis 15
2 Experimental techniques 16
2.1 Colloidal suspensions 16
2.1.1 Colloidal samples 16
2.1.2 Medium conductivity measurements 17
2.2 Microelectrode chamber design and fabrication 18
2.2.1 Microelectrode substrate 18
2.2.2 Microelectrode chamber 18
2.2.3 Coordinates 19
2.3 Optical tweezers-based single-particle force spectroscopy 20
2.3.1 Gradient force and scattering force 20
2.3.2 Characterization and calibration of trapping energy 21
2.3.3 Optical Setup 22
2.3.4 Particle tracing and image analysis 24
2.3.5 Determination of k_{OT} 25
3 Separation of dielectrophoresis and AC electroosmosis 29
3.1 Introduction 29
3.2 Experimental details 30
3.2.1 Particle motion calculation 30
3.2.2 Experimental hardware connections and control by Labview 33
3.2.3 Trapping an individual particle with optical tweezers 34
3.3 Results and discussion 35
3.3.1 Analysis of E^2-dependent forces 35
3.3.2 Isolated DEP crossover frequencies for polystyrene probes 37

3.3.3 Isolated AC electroosmotic flow 39
3.4 Conclusions 40
4 Low-frequency dielectrophoretic response of a colloidal particle 41
4.1 Introduction 41
4.1.1 α-relaxation 42
4.1.2 DEP and α-relaxation 42
4.2 Results and discussions 44
4.2.1 Particle size dependence of DEP crossover frequency 44
4.2.2 Medium viscosity dependence of DEP crossover frequency 46
4.2.3 Temperature dependence of DEP crossover frequency 47
4.3 Conclusions and outlook 48
5 Mapping of the flow field of AC electroosmosis 51
5.1 Introduction 51
5.2 Experimental details 52
5.2.1 Frequency dependence of AC electroosmosis 52
5.2.2 Spatial dependence of AC electroosmosis 53
5.3 Results and discussion 55
5.3.1 2D mapping of the AC electroosmotic flow field 55
5.3.2 Comparison of ACEO between experiments and theory 56
5.3.3 AC electroosmotic flow field in high electrolyte concentration 58
5.4 Conclusions and outlook 59
6 Optophoresis of SWCNTs 60
6.1 Introduction 60
6.2 Experimental details 61
6.2.1 Optical setup 62
6.2.2 SWCNT suspensions for Raman spectroscopy 64
6.2.3 Sample preparation 65
6.3 Results and discussion 65
6.3.1 DOC-SWCNT suspensions (1% DOC) 66
6.3.2 DOC-SWCNT suspensions (variable DOC concentration) 67
6.3.3 ssDNA-SWCNTs suspensions 69
6.3.4 Concentration and Orientation of SWCNTs 71
6.4 Conclusions and outlook 72
7. Conclusions and outlook 73
7.1 DEP crossover frequency in electrolytes 73
7.1.1 Medium conductivity 73
7.1.2 Hofmeister series 74
7.2 Mapping of the flow field of ACEO above the electrodes 74
7.3 Optical trapping induced orientation of SWCNTs 75

7.3.1 Optical setup 75
7.3.2 Fluorescence Spectroscopy on ssDNA-SWCNT suspensions 76
Appendices 79
Appendix A 79
Appendix B 81
Appendix C 83
Appendix D 87
Appendix E 91
Appendix F 93
Appendix G 96
Appendix H 105
Appendix I 107
References 109
Curriculum Vitae 111

LIST OF FIGURES

Fig. 1 Electrical double layer models 3

Fig. 2 Modified Gouy-Chapman Model of over-charged electric double layer 4

Fig. 3 The electric double layer in different geometries 5

Fig. 4 A diagram of electrophoresis and dielectrophoresis 7

Fig. 5 Diagrams of induced-charge electrokinetics 9

Fig. 6 Polarized electric double layer 10

Fig. 7 The chirality of a single-walled carbon nanotube 14

Fig. 8 Schematic diagram of the sample chamber 18

Fig. 9 Top view of the electrode chamber 20

Fig. 10 Optical trapping of a micron-sized single particle 21

Fig. 11 The Gaussian potential well of optical tweezers 22

Fig. 12 Setup of optical tweezers-based single-particle force spectroscopy 24

Fig. 13 Fitting of $D(\omega)$ 27

Fig. 14 Fitting of $\phi(\omega)$. 28

Fig. 15 Top view of optical tweezers-based force sensor 33

Fig. 16 Experimental hardware connections and control by Labview software 34

Fig. 17 Data analysis for strong E^2-dependent forces 36

Fig. 18 Data analysis for weak E^2-dependent forces 37

Fig. 19 Apparent crossover frequencies 38

Fig. 20 A spherical particle near to a non-slip wall 39

Fig. 21 DEP crossover frequency vs. particle size 45

Fig. 22 DEP crossover freqeuncy vs. 1/Visocisty 47

Fig. 23 DEP crossover freqeuncy vs. Temperature/Viscosity 48

Fig. 24 X-component of the ACEO flow velocity vs. frequency 53

Fig. 25 X-component of the ACEO velocity field in the x-z plane 54

Fig. 26 ACEO velocity field in the x-z plane 55

Fig. 27 Extrapolation of the ACEO velocity near the electrode tip 58

Fig. 28 Optical setup of Raman spectroscopy with optical tweezers 63

Fig. 29 Diagram of a focused Gaussian beam 64

Fig. 30 The Raman signal of sample 1 66

Fig. 31 The Raman signal of sample 2 67

Fig. 32 The Raman signal of sample 3 68

Fig. 33 The Raman signal of sample 4 69

Fig. 34 The Raman signal of sample 5 70

Fig. 35 The Raman signal of sample 6 70

Fig. 36 Possible behavior of ssDNA-SWCNTs in optical tweezers 71

Fig. 37 Optical setup of Raman and fluorescence spectroscopy and confocal microscopy for quantifications of the SWCNT concentration and orientation. 76

Fig. 38 Possible behavior of labeled ssDNA-SWCNTs in optical tweezers 77

Fig. 39 Fluorescence spectrsocopy on labeled ssDNA-SWCNTs 78

Fig. 40 A standard process of photolithography 82

Fig. 41 Fluid flux continuity 94

Fig. 42 Electric double layer as a dielectric layer 98

Fig. 43 Electrode chamber drawn with CAD 99

Fig. 44 The right planar electrode drawn with CAD 100

Fig. 45 Interior and exterior boundary conditions 101

Fig. 46 Meshing of subdomains 102

Fig. 47 Simulated x-component of the electric field 103

Fig. 48 Simulated z-component of the electric field 104

Table 1 DEP crossover frequencies for different-sized polystyrene beads 45

Table 2 X-components of the ACEO flow velocity at different locations (x_n, z_j) 93

Table 3 Linear extension of Table 2 along the x axis 94

Table 4 Specifics of the SWCNT suspension samples 108

Table 5 Specifics of Raman spectroscopy 108

ABSTRACT

AC electrokinetic forces experienced by polarizable colloidal particles in liquid suspensions, such as dielectrophoresis (DEP) and AC electroosmosis (ACEO), have been widely investigated for the purpose of transporting, sorting and positioning samples in microfluidic devices. However, independent studies of DEP and ACEO were impeded by the fact that the two mechanisms can both occur in the same experimental/application environment. To provide a more complete theoretical basis for the electrical polarizability of colloidal particles, and their interaction with the external electric field, we propose an isolation technique based on optical tweezers-based force spectroscopy and lock-in phase sensitive detection. This method extracts individual contributions from ACEO and DEP on a single spherical probe particle. From there we examined the relaxation process of a polarized particle with its associated electrical double layer in DEP. We also obtained an unambiguous velocity field of ACEO, mapped by a group of different-sized probes. We extended our studies to electrically polarized rod-shaped particles. We focused on a specific type of rod of great academic and industrial interest, single-walled carbon nanotubes (SWCNT), and studied their migration and orientation at optical frequencies.

1 INTRODUCTION

1.1 Electric double layer models

When a particle that carries partial charges on its surface is immersed in a solution containing electrolytes, counterions that uniformly disperse in the solution will accumulate at the particle-solvent interface to form a layer of ionic cloud. This process is a result of charge balance, during which opposite charges counteract each other to form an overall neutral solution. The layer of the ionic cloud is commonly referred to as the electric double layer.

The notion of electric double layer was first introduced by Helmholtz,[1] who modeled the interfacial charge distribution as a capacitor, as shown in Fig. 1. In the Helmholtz model, an immobilized double layer is absorbed on the charged surface of an colloidal particle. While simple, the model failed to explain electrokinetic mechanisms such as electrophoresis and electroosmosis, both driven by the migration of the interfacial ionic species referenced to the solid surface.[2]

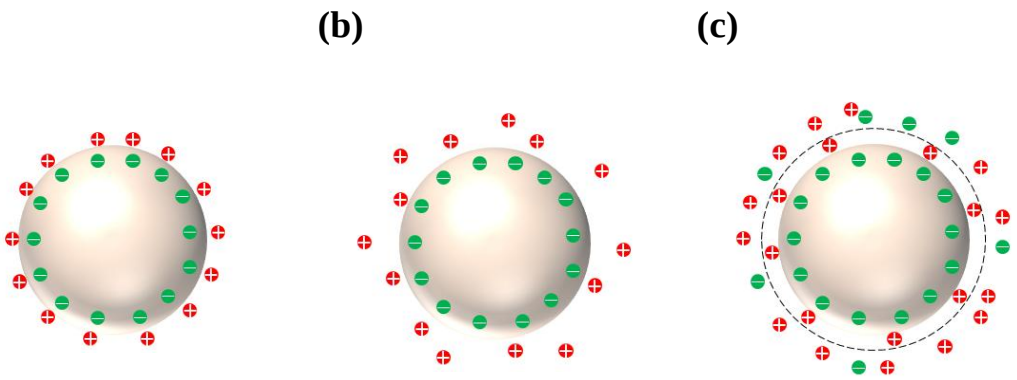

Fig. 1 Electrical double layer models

(a) The Helmholtz model of the electric double layer outside a negatively charged colloidal particle (grey sphere). Non-mobile counterions are absorbed at the surface of the particle. Red and green small circles denote positive and negative charges, respectively. (b) The Gouy-Chapman Model of the electric double layer outside a negatively charged colloidal particle. Diffusive counterions are free to move along the surface of the particle. (c) The Modified Gouy-Chapman Model of the electric double layer outside a negatively charged colloidal particle. A diffuse layer composed of diffusive counterions freely moves along the surface of the particle, while a Stern layer composed to less mobile counterions is absorbed at the surface of the particle. The diffuse layer and the Stern layer are separated by a Stern plane, as illustrated by a dashed line.

A significant correction, the Gouy-Chapman (G-C) model,[3,4,5] treats the double layer as a diffusive layer, as shown in Fig. 1. (b). In this model, the counterion distribution follows the Boltzmann distribution function, and therefore creates an exponential decay of the electric potential away from the interface to the bulk solution. Zeta potential, is defined as the potential difference between the surface that separates the free fluid in the bulk solution from the stagnant fluid attached to the interface, and a point at infinity in the bulk solution. It is widely used to characterize the amount of the electric charge within the double layer (proportionate to the zeta potential). A particle suspension with a large zeta potential (>25mV, a typical value calculated from $e\zeta = k_BT$, where e is the elementary charge, k_B is the Boltzmann constant and T is the absolute temperature) is an electrically stabilized system. In this system, the particle-liquid interface is highly charged to create a strong particle-particle Coulomb

repulsion, which creates a potential barrier preventing the short-range Van der Waals attraction, and thus avoiding particle aggregation.

G-C model failed to account for the sign reversal of the zeta potential in highly concentrated electrolytes (eg. a negative zeta potential on a positively charged surface). Further correction was made by Stern[6] to explain the zeta potential sign reversal by combining the Helmholtz and the G-C models. As shown in Fig. 1. (c), the double layer is divided into an absorbed Stern layer, which closely attaches to the charged surface, and an attracted diffuse layer, which is allowed to freely diffuse. The double layer can be over charged in solutions with abundant cations and anions, as shown in Fig. 2.

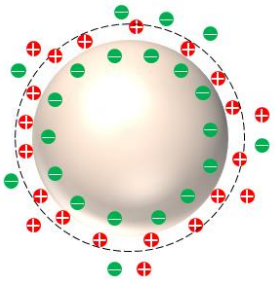

Fig. 2 Modified Gouy-Chapman Model of over-charged electric double layer

The Modified Gouy-Chapman Model of an over-charged electric double layer outside a negatively charged colloidal particle (grey sphere). A Stern layer composed of abundant non-mobile counterions (the cations confined by the dashed line) is absorbed at the surface of the particle. The surface charge density of the cations within the Stern layer is higher than that of the negative charges at the surface of the particle, so that the zeta potential is positive instead of negative.

The electric double layer plays a significant role in all electrokinetic mechanisms.[7] These mechanisms involve a fluid flow driven by the tangential motion of the diffuse layer along the charged surface. Depending on the geometry of the interface, electrokinetics may be characterized in two categories: a type that is related to the double layer movement outside colloidal particles, as shown in Fig. 3 (a), and

the other type related to the double layer movement along a planar electrode surface, as shown in Fig. 3 (b).

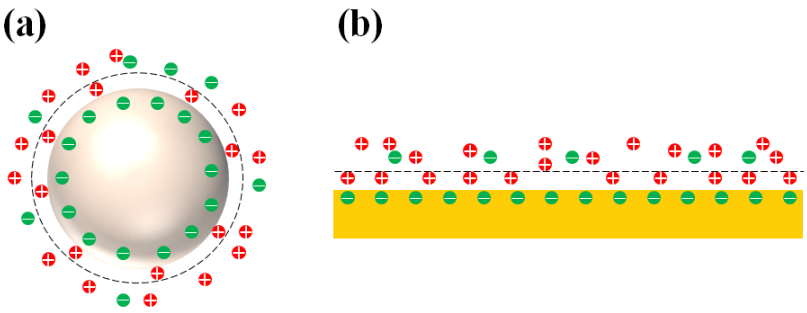

Fig. 3 The electric double layer in different geometries

The electric double layer (a) outside a negatively charged colloidal particle (grey sphere) and (b) on the surface of a piece of negatively charged electrode (yellow block). The diffuse layer and the Stern layer are separated by a Stern plane, as illustrated by a dashed line.

1.2 Thickness of double layer

The characteristic thickness of the electric double layer is called the Debye length, which commonly follows the notation of κ^{-1} or λ_D. The Debye length[8] in an electrolyte is given by $\lambda_D = \left(\frac{\varepsilon_0 \varepsilon_m k_B T}{2 N_A e^2 I} \right)^{\frac{1}{2}}$, where ε_0 is the vacuum permittivity, ε_m is the relative permittivity of the fluid medium, N_A is Avogadro's number and I is the ionic strength of the electrolyte in molar (mol/m^3). In aqueous solutions, by assuming ε_m = 78 and room temperature T = 300 K, we derive a simplified expression $\lambda_D = \frac{0.304}{\sqrt{I}}$ (λ_D in nm, and I in molar). This indicates that the typical Debye length may vary from several to hundreds of nanometers depending on the ionic strength, or in other words, electrolyte concentration. The Debye length in highly deionized water can be up to ~1000 nm.

1.3 Double layer movement outside colloidal particles

A colloid is a chemical system, in which one substance is microscopically dispersed evenly throughout another medium substance of a continuous phase. Colloidal systems that are commonly seen in our daily life include foams (gas particles dispersed in liquid medium), creams and emulsions (liquid particles dispersed in liquid medium), and smokes (solid particles dispersed in gas medium). From these examples we notice that dispersed particles can consist of any kind of material including solid, liquid or gas. The size restriction of colloidal particles, which can be from several to thousands of nanometers, is related to the stabilization of the colloidal system. A stabilized system requires the non-continuously dispersed particles not to settle out (sedimentation) or float to the top of the medium (creaming) due to gravity. Microscopically, particles don't aggregate when the electrostatic repulsion between neighboring charged particles (with their associated double layer) prevent particles from close encounter where Van der Waals attraction dominates.

When a colloidal suspension is placed in an external electric field, the field induces the double layer to move along the colloidal particle surface by exerting Coulomb forces on the counterions. Depending on the uniformity of the electric field, particles may experience electrophoresis (EP) or dielectrophoresis (DEP). In a spatially uniform electric field, the relative motion of charged particles to their surrounding medium is called electrophoresis,[9] as shown in Fig. 4. (a). In a spatially non-uniform electric field, the frequency-dependent motion of a dielectric particle along the gradient of the square of the field is called dielectrophoresis, as shown in Fig. 4. (b).[9,10,11] (More details follow in Section 1.6.1.)

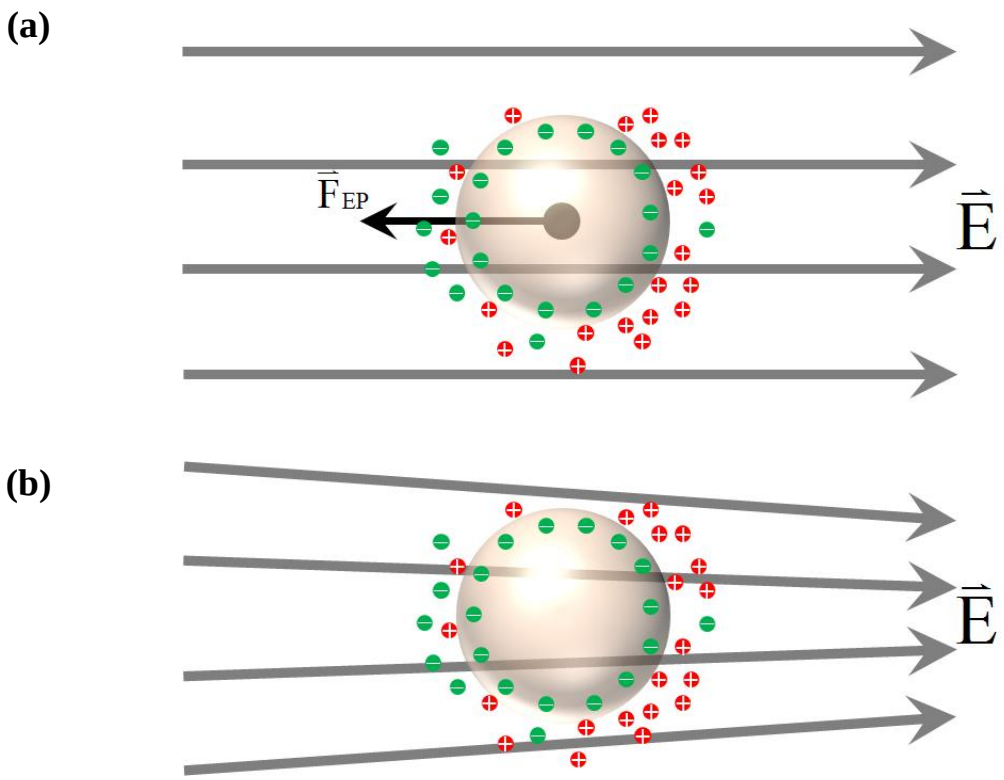

Fig. 4 A diagram of electrophoresis and dielectrophoresis

(a) Dlectrophoresis as the motion of charged particles in a uniform electric field. When a negatively charged colloidal particle (grey sphere) experiences an electrostatic force along the direction against the electric field, its associated positive electric double layer experiences a Coulomb force along the opposite direction. (b) A colloidal particle with its associated electric double layer experiences dielectrophoresis along the direction of the gradient of the square of the electric field in a nonuniform electric field, which is indicated by the grey arrows.

1.4 Double layer movement above planar conductive electrodes

A metallic surface usually does not carry partial charges, therefore, an electric potential applied to the surface is necessary for the double layer to form. When a tangential (relative to the surface plane) electric field is applied to the electrode-liquid interface, the field induces the double layer to move along the planar surface. Electrokinetic mechanisms such as electroosmosis (EO), AC electroosmosis (ACEO) and streaming current are referred to as induced-charge electrokinetics. Electroosmosis is a fluid flow induced by the motion of the double layer, which is

driven by an external electric field along a solid wall, as shown in Fig. 5. (a).[7] AC electroosmosis is an electrokinetic flow due to the interaction of the double layer with the tangential component of a nonuniform AC electric field, as shown in Fig. 5. (b).[12] (More details in Section 1.6.2.) The major difference between EO and ACEO is that: in the former case, the formation of the double layer doesn't depend on the external field; while in the latter case, the double layer is formed by the normal component of the applied field. As shown in Fig. 5. (c), streaming current is a net charge transport driven by the motion of the double layer along with the pressure-driven fluid flow.[7]

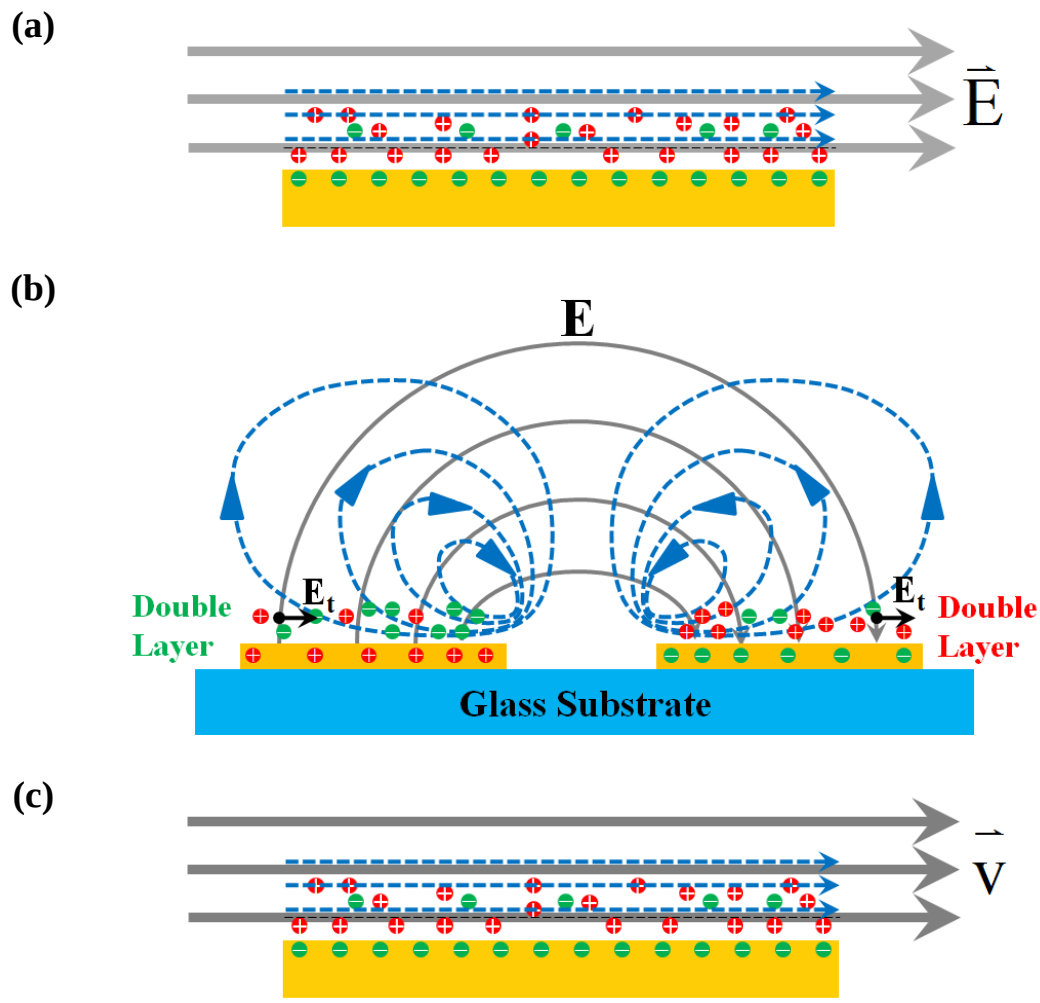

Fig. 5 Diagrams of induced-charge electrokinetics

(a) An electroosmotic flow (dashed blue arrows) induced by the electrical double layer movement driven by the external electric field (grey arrows) along the surface of a piece of negatively charged electrode (yellow block). (b) An AC electroosmotic flow (dashed blue lines) induced by the electrical double layer movement driven by the tangential electric field along the electrode surface. The direction of the flow is indicated by the blue arrows. Solid grey lines show the electric field during a half cycle of the AC electric field generated by oppositely charged planar electrodes. The tangential components of the electric field are indicated by the black arrows. (c) A surface current (dashed blue arrows) induced by the electrical double layer movement driven by the external flow field (grey arrows) along on the surface of a piece of negatively charged electrode.

1.5 Polarization of double layer

Electrokinetics is often modeled as the interaction of a three-phase system (colloid/electrode, electric double layer, liquid solution) with the external electric field.

While the electrical properties of the solid and liquid phases may be defined; it is difficult to directly quantify the double layer. The characterization of a polarized double layer by the field is especially complicated, when an asymmetric distortion of counterion distribution forms outside colloidal particles or above electrodes, as shown in Fig. 6. Moreover, the polarizability of the double layer has a strong dependence on the field frequency. Difficulty in predicting properties such as the electric conductivity σ and relative permittivity ε, presents challenges in fully understanding most electrokinetic mechanisms.

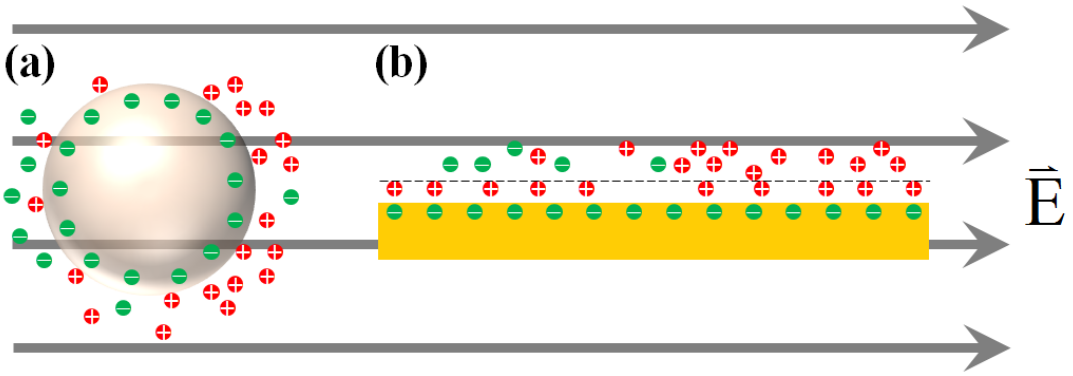

Fig. 6 Polarized electric double layer

Polarization of the electric double layer (a) outside a colloidal particle and (b) above a planar electrode surface. Within the double layer, cations migrate along the electric field whereas anions against the electric field. They each aggregate locally to form an asymmetric distortion of counterion distribution.

1.6 E^2-dependent AC electrokinetics

In this thesis we present studies of two electrokinetic mechanisms: dielectrophoresis and AC electroosmosis. We determine the role played by the electric double layer in the resulting motion of either a particle or the fluid. Both DEP and ACEO are most significant in AC electric fields. When they are applied to lab-on-a-chip systems, a small peak-to-peak electric potential typically of several

Volts is necessary to create a sufficiently strong driving force for transporting particles. Compared to traditional mechanical pumps, DEP[13,14,15,16,17,18,19] and ACEO[20,21] are widely considered to be effective for manipulation of micron- and nano- scale objects (cells, bacteria, viruses, DNA, proteins and carbon nanotubes).

1.6.1 Dielectrophoresis

DEP is a directed motion of electrically polarizable particles in a nonuniform electric field,[9,10,11] as shown in Fig. 4. (b). In an AC electric field the time-averaged DEP force on a spherical particle is proportional to the gradient of the square of the electric field,[9]

$$F_{DEP} = 2\pi r^3 \varepsilon_0 \varepsilon_m \, \mathrm{Re}\{K(\omega)\} \nabla |\vec{E}|^2 \qquad (1)$$

where r is the particle radius, ε_0 is the vacuum permittivity, ε_m is the relative permittivity of the medium, and ω is the angular frequency of the electric field $\vec{E}$. $\mathrm{Re}\{K(\omega)\}$ is the real part of the Clausius-Mossotti factor for a spherical particle in a uniform medium:[9]

$$K(\omega) = \frac{\tilde{\varepsilon}_p(\omega) - \tilde{\varepsilon}_m(\omega)}{\tilde{\varepsilon}_p(\omega) + 2\tilde{\varepsilon}_m(\omega)} \qquad (2)$$

where $\tilde{\varepsilon}_p$ and $\tilde{\varepsilon}_m$ are complex permittivities of the particle and of the liquid medium, respectively. Complex permittivity as a function of angular frequency is defined as $\tilde{\varepsilon}(\omega) \equiv \varepsilon - j\cdot(\sigma/\omega)$ where ε is the real part of the permittivity, $j \equiv (-1)^{1/2}$, and σ is the conductivity. As described in Section 1.1.1, for a charged colloidal particle in aqueous suspension, an electric double layer forms at the interface of the particle and the liquid. In this case $\tilde{\varepsilon}_p$ is the permittivity of the particle with its associated double layer, and correction to the conventional Clausius-Mossotti form is necessary to describe the $K(\omega)$

term. At a specific frequency known as the DEP crossover frequency, relaxation of the double layer causes the direction of the DEP force to reverse,[11] corresponding to a sign change of the real part of $K(\omega)$. Near this frequency the net time-averaged DEP force on the particle is zero.

1.6.2 AC electroosmosis

ACEO is an electrokinetic flow caused by the interaction of the electric double layer above an electrode with the tangential component of an external AC electric field, as shown in Fig. 5. (b). The double layer follows the switching polarity of the applied electrical potential. The counterions are then driven by the electric field, collide with and transfer momentum to water molecules, thus producing a hydrodynamic flow. The ACEO force is exerted near the electrode surface where the double layer is located. Due to a non-slip boundary condition at the electrode surface, the maximum flow velocity is outside of the double layer at the shear surface. When the electric potential applied to the electrodes is reversed, both the direction of the electric field and the polarity of the double layer charge reverse, resulting in a unidirectional fluid flow.[12,22] Fluid outside the double layer is driven parallel to the electrode surface at a velocity given by the Helmholtz-Smoluchowski equation

$$|v| = \frac{\varepsilon_0 \varepsilon_m \zeta}{\eta} E_t \tag{3}$$

where E_t is the tangential component of the E-field in the double layer, and η is the medium viscosity. In the Debye-Hückel approximation $e\zeta/k_BT<1$,

$$\zeta = \lambda_D E_n \tag{4}$$

where E_n is the normal component of E at the shear surface. Assuming E_t is constant

inside the double layer, Eq.(3) and (4) yield

$$|v| = \frac{\varepsilon_0 \varepsilon_m}{\eta} \lambda_D E_t E_n \propto E^2 \tag{5}$$

i.e. the electroosmotic flow velocity is quadratic in the magnitude of the electric field at the shear surface.[20] E_t and E_n are most intense near the electrode gap and diminish with distance from the gap. By ignoring the wall effect, spherical colloidal particles of radius r suspended in ACEO flow experience a Stokes force $6\pi\eta rv$, which is thus proportional to the flow velocity in Eq.(5)

$$F_{ACEO} = 6\pi r \varepsilon_0 \varepsilon_m \lambda_D E_t E_n \tag{6}$$

1.7 Polarization of rods

For the purpose of simplicity, people always start with modeling a system with spherical symmetry when addressing unknowns of a physical mechanism. We follow the same path by first studying how spherical particles interact with the external electric field in dielectrophoresis and AC electroosmosis. Then we extend our interests to particles with cylindrical symmetry: rods. Importantly, the electrical polarizability of a particle strongly depends on its geometrical features. While the polarizability of a spherical particle is mainly contributed by that of the interfacial double layer (within our context), a rod may inherently be easily polarized along its longitudinal direction due to its large aspect ratio.

Single walled carbon nanotubes (SWCNT), belong to a type of rods with small diameter and large aspect ratio. Viewed as potential building blocks for interconnections in very-large-scale integration, they have attracted widespread

research interest. The tube's typical diameters are in the scale of 1 nm, their length can be hundreds of nm or several μm.

Depending on how a graphene sheet is wrapped to form a SWCNT, as shown in Fig. 7, SWCNTs with different chiralities may display diverse electrical properties. Specifically, they either belong to the semiconducting or the metallic groups.[23] When the tubes are placed in an AC electric field, they may or may not be highly polarized, depending on their frequency-dependent dielectric properties. These interesting properties mostly attributed by the intrinsic material instead of their surrounding environment inspire great scientific curiosity about how SWCNTs may response to a nonuniform electric field.[24]

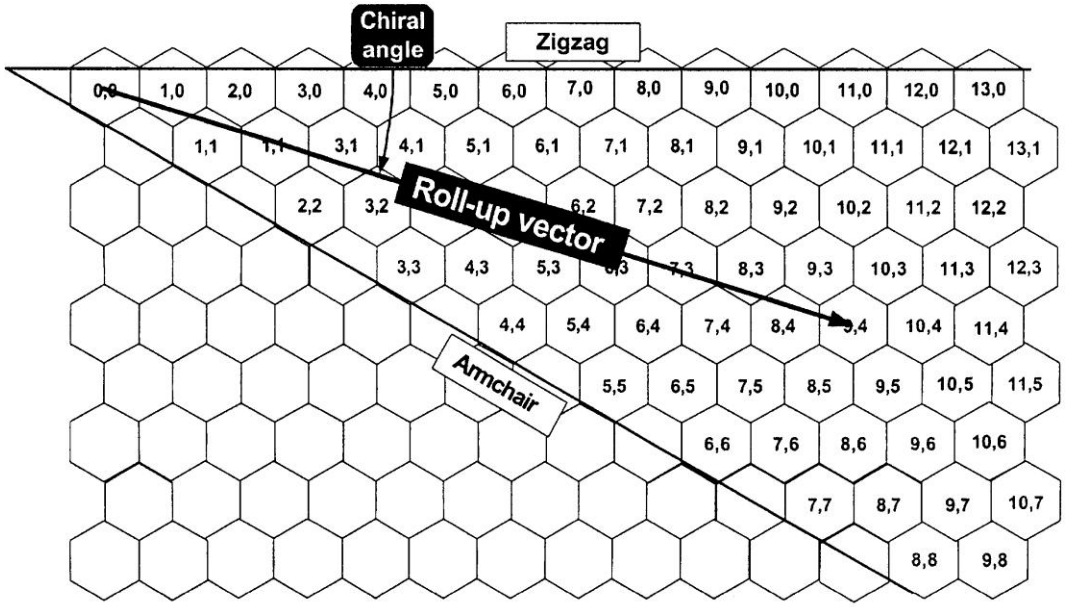

Fig. 7 The chirality of a single-walled carbon nanotube
(n,m) indices used to characterize the chirality of a single-walled carbon nanotube.[25]

1.8 Structure of this thesis

In Chapter 1, we discussed the significance of the electrical double layer in electrokinetic mechanisms. However, independent studies of AC electrokinetics such as dielectrophoresis and AC electroosmosis, were impeded by the fact that the two mechanisms can both occur in the same experimental/application environment. In Chapter 2, we introduce the materials and methods of sample preparation and optical tweezers, which were applied to investigate DEP and ACEO. In Chapter 3, we propose a unique technique, optical tweezers-based single-particle force spectroscopy, to isolate DEP and ACEO. This method extracts individual contributions from ACEO and DEP on a single spherical probe particle. From there, we are able to inspect the frequency dependence of DEP in Chapter 4, and the special dependence of ACEO in Chapter 5. In Chapter 6, we extend our studies to the interaction of SWCNTs with an external electric/optical field.

2 EXPERIMENTAL TECHNIQUES

2.1 Colloidal suspensions

2.1.1 Colloidal samples

Colloid samples were made by diluting commercial polymer microsphere samples with deionized water. We started with polystyrene microsphere suspensions in water, packaged at 10% solids by weight (Thermo Scientific, 5000 Series). They have a refractive index of 1.59 at 589 nm (our working laser beam has wavelength of 1064 nm) and a density of 1.05 g/cm^3. The purchased suspensions include less than 0.5% dispersant/surfactant or preservative, of which the content is unknown. Their contribution to the final ionic strength of colloidal samples remained unclear. We obtained deionized water with a resistivity of 18.3 MΩ/cm (Barnstead Easypure RF Lab Water System), and then had it stored in 50 ml centrifuge tubes (BD Falcon).

A low concentration (0.001% w/v) particle suspension was used to isolate individual particles as force probes. We ignored the particle-particle interaction, by realizing that the distance between neighboring particles were always orders of magnitude larger than the Debye length scale, even in liquid medium of extremely low ionic strength. An evaluation is shown in Appendix A.

All the colloid samples were made in 1000 μL volume at room temperature of 20 ℃~25 ℃. Two micropipettes that handle different liquid volumes of 2~20 μL and 20~200 μL were used for the purpose. First, we released a calculated amount of deionized water in a 2000 μL test tube. A colloidal suspension to be diluted was shaken for ~30 seconds by use of a vortex mixer (Barnstead 16700 mixer) to avoid inhomogeneous particle distribution. The suspension liquid was then drawn from the

center of its container and driven in the 2000 μL test tube containing deionized water. We rinsed off the interior of the disposable pipette tip with the new sample solution, by pressing and releasing the micropipette a couple of times.

2.1.2 Medium conductivity measurements

We used an Accumet AP85 meter with its conductivity/TDS/temperature probe for medium conductivity measurements. The meter was prepared for conductivity calibration in the 0 to 1999 μS/cm range, with a 1413 μS/cm standard solution. When doing so, we thoroughly rinsed the probe with deionized water and then a small amount of 1413 μS/cm calibration standard. We dipped the probe into the calibration standard, and made sure that the probe tip was immersed beyond the upper steel band. We gently stirred the probe to create a homogenous sample and waited for the measurements to stabilize. Then we adjusted the reading to match the value of the calibration standard.

Before conducting a measurement of a sample medium with the calibrated meter, we first thoroughly rinsed the probe with the deionized water. The probe was then air dried with N_2 gas. To avoid contamination or dilution of the sample, we rinsed the probe with a small volume of the sample liquid. We dipped the probe into the sample, with the probe tip immersed above the upper steel band. The medium conductivity was within the range 0.8~2.1 μS/cm. The meter readings were low (~0.8 μS/cm) at first and stabilized at higher values (~2.1 μS/cm) when we gently stirred the probe and waited for a couple of minutes. Since our solution was an extremely low concentration electrolyte, that the G-C model is a reasonable approximation when approaching the view of the electrical double layer.

2.2 Microelectrode chamber design and fabrication

2.2.1 Microelectrode substrate

Measurements of nonlinear electrokinetics such as DEP and ACEO require a highly nonuniform electric field. The condition was achieved by fabricating a pair of gold microelectrodes with sharp tips on a glass substrate, as shown in Fig. 8. Ti/Au (10 nm/200 nm) microelectrodes were deposited on a microscope cover glass (Fisher Scientific Inc., 12-545-J 22X60-1) by standard photolithography,* as shown in Appendix B.

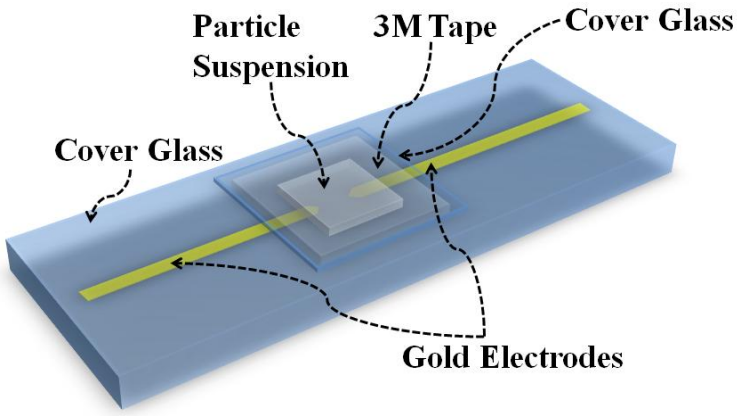

Fig. 8 Schematic diagram of the sample chamber

2.2.2 Microelectrode chamber

We used 100 μm-thick 3M Scotch tapes as spacers to create a microelectrode chamber, as shown in Fig. 8. We cut off an area of 0.5 cm×0.5 cm from the tape and apply the rest to the glass substrate while exposing the gap between the two electrode tips. We cleaned the gap area by rubbing it with a cotton swab and 99% ethanol

* We thank Dr. Pochin Kuo, Dr. Yi Hu, and Dr. Markus Gnerlich for providing the DEP electrodes.

solution. After the ethanol solution was air dried in a couple of seconds, we injected 20 μL of the sample liquid in the chamber with a micropipette. A piece of cover glass (Fisher Scientific Inc., 12-545-101 22CIR.-1) was cleaned with 99% ethanol and air dried. It was then slowly laid on top of the gap area in order to avoid the formation of air bubbles within the chamber. By gently pressing down the cover glass, we absorbed the extra liquid squeezed out of the gap area with a cotton swab. While keeping the cover glass gently pressed, we sealed the chamber at the edge of the cover glass with vacuum grease (Dow Corning, DC-976), to prevent "ionic" pollution.

2.2.3 Coordinates

We use Cartesian coordinates and define the origin as the midpoint between the two electrode tips on the glass substrate plane, as shown in Fig. 9. From the origin and directed towards the right electrode tip is the x axis; the y and z axes are correspondingly directed following the right hand rule. We designate the distance between the origin and the particle position projected along the x axis as "x," and the particle suspension height above the substrate surface as "z." The gap between the two electrode tips was 28μm. In our experiments, x fell in the range of (0, 14) μm. The thickness of the electrode chamber was 100μm, therefore z fell in the range of (0, 100) μm.

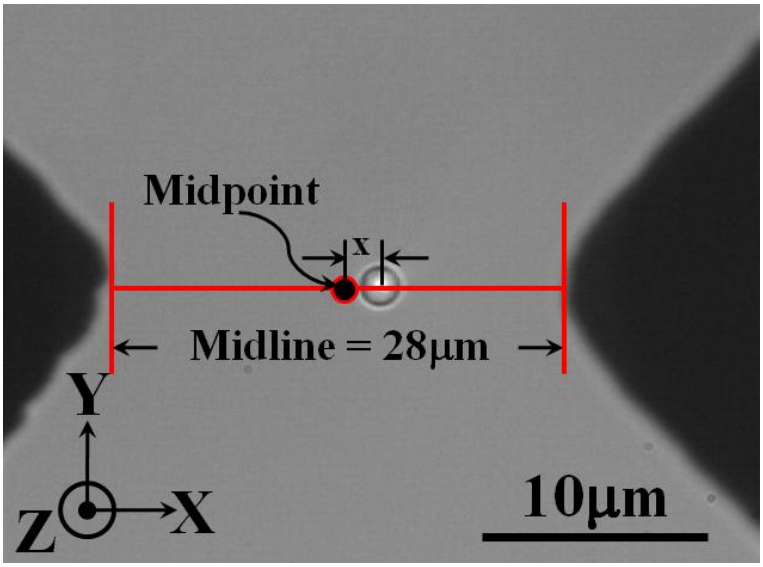

Fig. 9 Top view of the electrode chamber

The triangle dark blocks are the gold electrodes. A polystyrene particle of 1050 nm in radius is placed along the midline, and near the z axis. The image was taken with bright field microscopy.

2.3 Optical tweezers-based single-particle force spectroscopy

2.3.1 Gradient force and scattering force

The use of a highly focused laser beam, later referred to as optical tweezers, to trap micron and sub-micron particles due to its optical gradient and scattering forces was first reported by Arthur Ashkin.[26] A focused laser beam contains a strong electric field gradient, with the gradient minimum located at the focal point. Dielectric particles that are more polarizable than their surrounding medium at optical frequencies, (in other words, with higher refractive indices) are attracted by the "gradient force" along the field gradient to the focal point, thus lowering the total electrostatic energy. The refractive index of polystyrene particles at optical frequencies is 1.59, which is higher than that of water (1.33). Given the refractive index difference, particles "prefer" to stay at the center of the optical trap, where the electric field gradient is zero. Meanwhile, particles also experience anti-trapping

"scattering forces" by receiving the proton momentum. Protons push the particles along the direction of beam propagation. Therefore, the optical tweezers' trapping center is in practice not at the focal point. Instead, it is displaced slightly downstream along the direction of the beam propagation, as shown in Fig. 10.

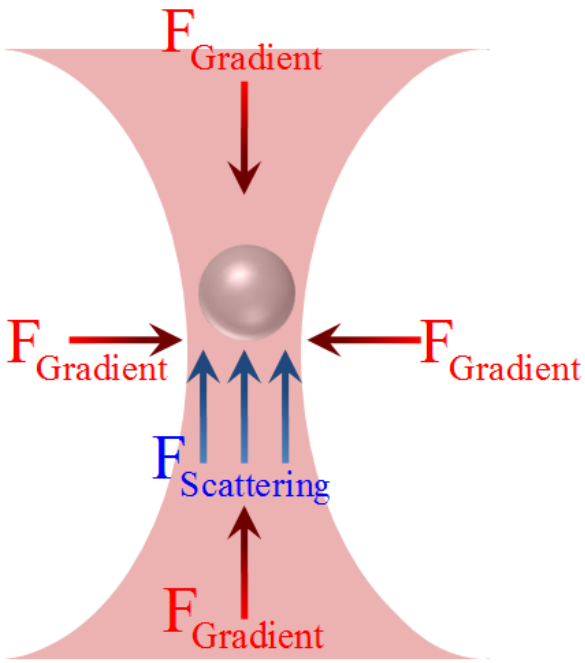

Fig. 10 Optical trapping of a micron-sized single particle
While the gradient force is exerted on the particle to hold it at the focal point of the laser beam, the scattering force slightly pushes the particle downstream along the beam propagation direction.

2.3.2 Characterization and calibration of trapping energy

Optical tweezers can be used as force sensors that are capable of detecting pico-Newton forces experienced by trapped particles.[27] An optical trap is approximated as a Gaussian potential well. Particles situated at the trapping center, (the bottom of the potential well) can be moved by external forces that are balanced by the restoring force of the tweezers.[11] If the particle displacement is a small fraction of the width of the Gaussian potential well, the restoring force can be written as

$F_{external} = k_{OT}x$ as a first order approximation, where k_{OT} is the spring constant or stiffness of the optical tweezers, and x is the displacement of the particle from the trapping center, as illustrated in Fig. 11.[11]

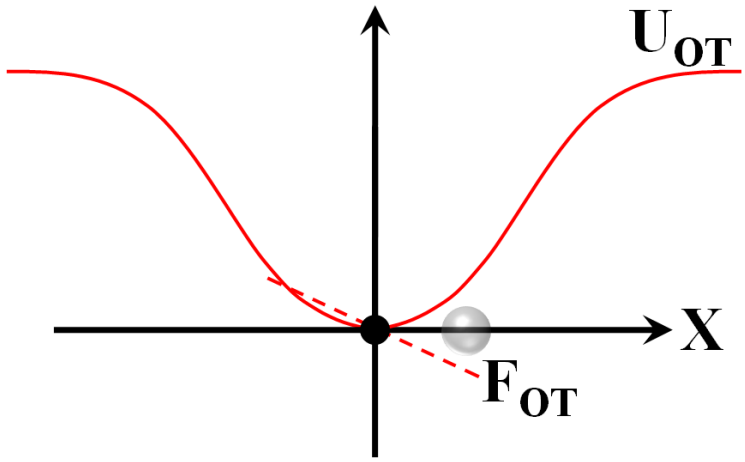

Fig. 11 The Gaussian potential well of optical tweezers
In the first order approximation, a particle that is deviated by an external force away from the laser's focal point experiences a restoring force by optical tweezers that is proportional to the displacement.

2.3.3 Optical Setup

Fig. 12 is a schematic of the optical tweezers-based single-particle force sensor. A 1064 nm laser beam (Diode-Pumped Solid-State Laser) forms the optical tweezers. The beam was first expanded to overfill the back aperture of the objective of ~0.8 cm in diameter. It was then sent through a high numerical aperture oil immersion objective lens (100X, N.A. = 1.3). This ensured the isotropic trapping stiffness in the direction transverse to the beam propagation. We used a half-wave plate to rotate the direction of the linear polarization of the laser beam. Together with a polarized beam splitter, we were able to let through only a part of the total light intensity and hence control the trapping power after the objective.

We tracked the particle motion with a 980 nm laser beam (Diode Laser), which was collimated collinear and parfocal to the tweezers' beam. The two laser beams were combined by a longpass filter (Thorlabs FEL1000), which is highly reflective at 980 nm, and highly transmissive at 1064 nm. The tracking beam was diffracted by the particle held by the trapping beam, and the particle movement was projected on a transverse plane referenced to the propagation of the beams. The particle motion was collected by a condenser (N.A = 0.9) and thereafter detected by a quadrant photodiode (QPD) (Hamamatsu S7479). A shortpass filter (Thorlabs FES1000) was used to block the 1064 nm trapping beam from entering the QPD. To prevent the 980nm beam from interfering with the trapping effect, it was attenuated so that its power was two orders of magnitude lower than that of the 1064 nm laser. Our particle tracking system provides spatial resolution in the subnanometer range.

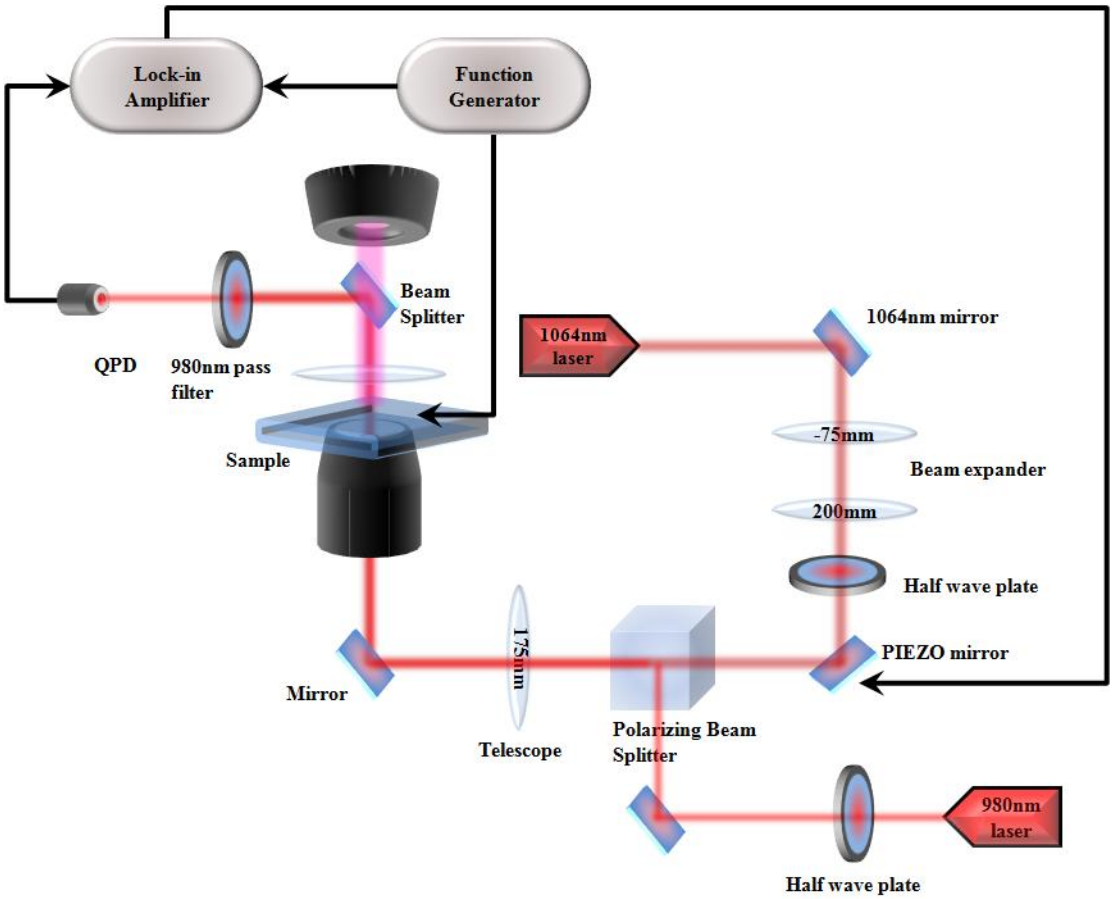

Fig. 12 Setup of optical tweezers-based single-particle force spectroscopy

2.3.4 Particle tracing and image analysis

A QPD converts the diffracted light of the 980 nm tracking laser beam into a voltage signal, which is then recorded by a lock-in amplifier for data analysis. Three steps were necessary to calibrate from this output voltage the particle displacement that is transverse to the laser propagation (QPD voltage in "V" ↔ Particle displacement in "nm"):

Particle displacement (nm) ↔ Particle displacement (pixel)

Particle displacement (pixel) ↔ PIEZO mirror voltage (V)

PIEZO mirror voltage (V) ↔ QPD voltage (V)

First we calibrated the conversion between the displacement measured in nanometer and pixel by using bright field microscopy and imaging a standard Ronchi ruling (5,000 lines/inch). This gave a conversion rate of 95.25 nm/pixel. Secondly we used a lock-in amplifier and applied 1 V to drive a piezoelectric mirror that reflects the optical trapping beam. The displacement of the reflected focal light spot was traced by a CCD camera and recorded in pixels. Given the conversion rate obtained in the first step, we derived the displacement in nm. Finally, we returned to the relation between the piezoelectric mirror voltage driven by the lock-in amplifier and the QPD voltage output read by the same lock-in amplifier. This was to solve for the linear range of QPD voltage as a function of the particle displacement, which follows Hooke's Law. We inspected the linear trapping range for a polystyrene particle driven by the PIEZO mirror at an amplitude of 0.5 V, and collected the variation range of the QPD voltage.

2.3.5 Determination of k_{OT}

We calibrate the spring constant k_{OT} by the method of optical forced oscillation. A trapped particle is forced into oscillation at the amplitude of ~20 nm by a piezoelectric electric mirror that reflects the trapping beam. The piezoelectric mirror is controlled by a functional generator built within a lock-in amplifier. The total force on the trapped particle is composed of two terms: (1) optical tweezers' restoring force, which follows Hooke's Law within a limited displacement range (the first order approximation as previously described), and (2) liquid medium's viscous damping force $6\pi\eta r\dot{x}$, which follows Stokes' law. The equation of motion is:

$$F_{external} = m\ddot{x} = k_{OT}(Ae^{i\omega t} - x) - 6\pi\eta(\omega)r\dot{x} \quad (7)$$

where m is the mass of the particle, x is the particle displacement relative to the center of the oscillatory optical tweezers, A and ω are the amplitude and frequency of the oscillatory trapping beam, respectively, t is time, η is the liquid medium viscosity, and r is the particle radius.

We neglect the inertia term $m\ddot{x}$ on the left side of the equation, because of a low Reynolds number $6\pi\eta(\omega)r\dot{x} \gg m\ddot{x}$. The general solution of the steady state is $x(\omega, t) = D(\omega)e^{i[\omega t - \varphi(\omega)]}$, where both the amplitude D and phase ϕ are obtained from a lock-in amplifier. By solving the differential equation we obtain:

$$D(\omega) = \frac{Ak_{OT}}{\sqrt{k_{OT}^{\ 2} + (6\pi\eta r\omega)^2}} \quad (8)$$

$$\varphi(\omega) = \tan^{-1}\left(\frac{6\pi\eta r\omega}{k_{OT}}\right) \quad (9)$$

Eqs. (8) and (9) are fit to the experimental data of the amplitude D(ω) and the relative phase ϕ(ω) as a function of frequency of the oscillation of a trapped polystyrene particle to produce the value of k_{OT}. The two independent fittings gave k_{OT} values that agree with each other within 10%. One example of a 750 nm polystyrene particle in deionized water that has a viscosity 0.852 mPa·s gives k_{OT} = 11.4 pN/μm from D vs. ω, and k_{OT} = 10.1 pN/μm from ϕ vs. ω, as shown in Fig. 13 and Fig. 14.

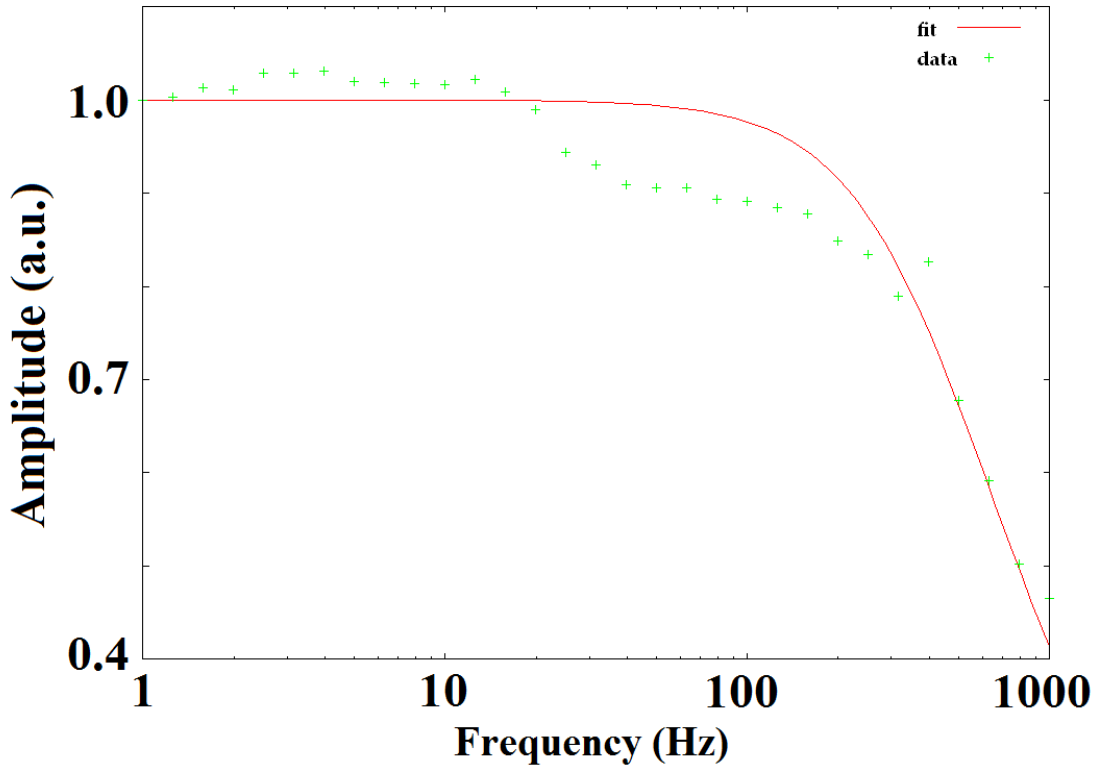

Fig. 13 Fitting of D(ω)

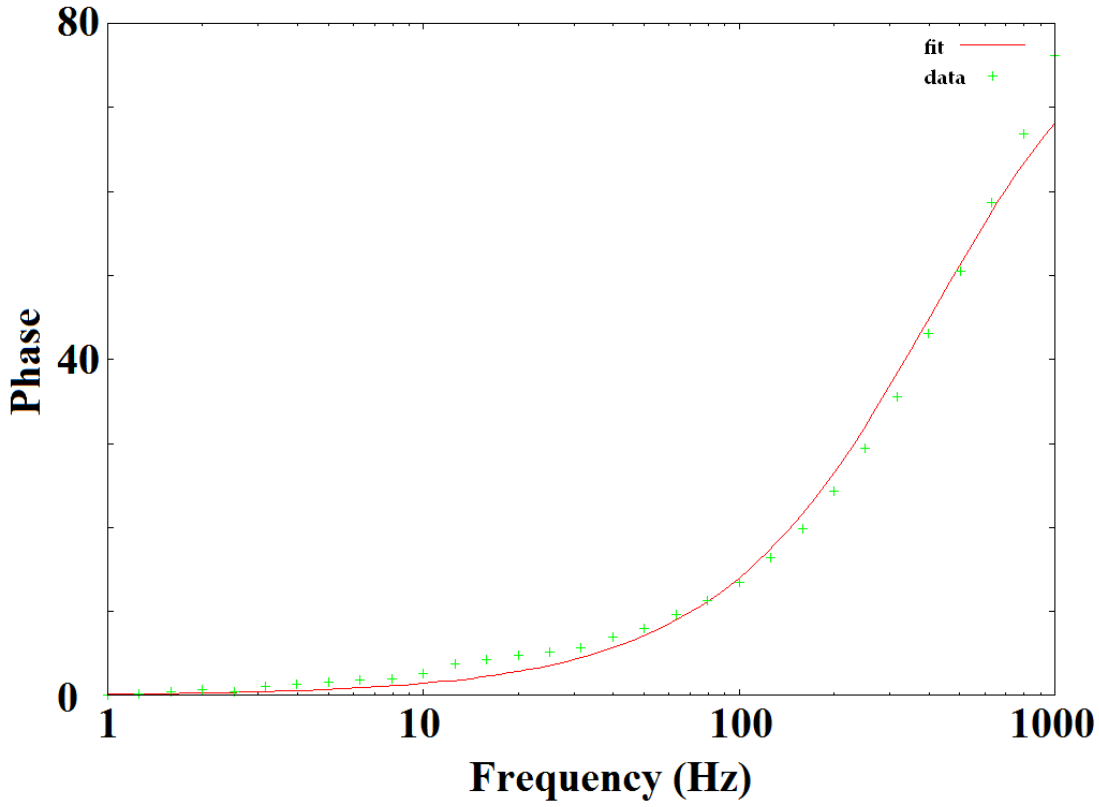

Fig. 14 Fitting of $\phi(\omega)$.

3 SEPARATION OF DIELECTROPHORESIS AND AC ELECTROOSMOSIS

3.1 Introduction

Forces of electrical origin in aqueous suspensions have been widely investigated for the purpose of transporting, sorting and positioning particles on microfluidic devices.[13,14,15,16] Incorporation of AC electrokinetic mechanisms, such as dielectrophoresis and AC electroosmosis, in lab-on-a-chip systems has attracted widespread interest, because there is no need for mechanical pumps to generate flows hence particle motion.[17,18,19,20,21]

As described in Chapter 1, DEP is a phenomenon in which a force is exerted on a dielectric particle when it is subjected to a nonuniform electric field. The DEP force experienced by a charged colloidal particle suspended in liquid medium is frequency dependent. The force switches direction and is zero at a specific frequency, namely the crossover frequency f_C.

ACEO is a nonlinear phenomenon of induced-charge electroosmotic flow around electrodes applied with an alternating voltage. The flow is induced by the counterion motion along the electrode surface driven by an external field. A maximum flow velocity is observed outside of the double layer.

The commonly adopted method to study either DEP or ACEO is "video microscopy", also called "particle-image velocimetry".[15] In this method, force information is obtained by visualizing tracer particles' displacement driven by those forces in liquid suspensions using a CCD camera. During the process, complication factors, such as thermal fluctuation, heat induced convection and other

electrostatic/electrokinetic forces, are not eliminated to guarantee selective measurements.[28,29,30,31,32,33] We demonstrate quantification methods with high selectivity for both DEP and ACEO on individual particles. The technique allows independent discussions of each mechanism in Chapter 4 and Chapter 5, respectively.

We apply optical tweezers-based force spectroscopy with lock-in phase-sensitive detection. First we discriminate ACEO and DEP from forces that are not quadratic in the magnitude of the electric field. Then we determine the DEP crossover frequency, i.e. the frequency at which the DEP force on the probe particle vanishes. By measuring the force on the particle at its DEP crossover frequency, we observe the effects solely due to ACEO. Isolation of ACEO from DEP is accomplished by taking advantage of the fact that ACEO depends on $|\vec{E}|^2$, which varies spatially, whereas the DEP crossover frequency of the probe particle is independent of $|\vec{E}|$, and therefore doesn't change with location.

3.2 Experimental details

3.2.1 Particle motion calculation

An AC voltage of 3 Volt peak-to-peak (3Vpp) is applied to the opposing microelectrodes. The resulting forces on the particle, which could involve DEP, ACEO and potentially other electrokinetic/electrostatic mechanisms, cause the particle to deviate from the center of the optical trap, as shown in Fig. 15. For selective measurements, the field is AM modulated using a lock-in amplifier (Stanford Research SR830) at a frequency two orders of magnitude lower than the working frequencies of DEP or ACEO (typically larger than 1 kHz) to avoid interference. A lock-in amplifier is commonly used to extract amplitude and phase

information of an oscillatory signal at a constant reference frequency for signal mixed with noises. At twice the AM modulation frequency, we measure E^2-dependent forces. In our experiment these forces are exclusively due to ACEO and DEP, which are both along the x direction due to the geometrical symmetry.

$$F_{E^2} = F_{ACEO} + F_{DEP} \tag{10}$$

The total force F_{total} exerted on the particle is contributed by (1) optical tweezers' restoring force $k_{OT}x$, which follows Hooke's Law within a limited displacement range, (2) liquid medium's viscous damping force $6\pi\eta r\dot{x}$, and (3) electrokinetic forces of DEP and ACEO $F_{ACEO+DEP}$. The force balance is manifested in Fig. 15. We write the equation of motion in one dimension as

$$F_{external} = m\ddot{x} = F_{ACEO+DEP}(x) + k_{OT}x + 6\pi\eta r\dot{x} \tag{11}$$

where m is the mass of the particle, x is the displacement of the particle from the optical tweezers' focal point, k_{OT} is the spring constant of optical tweezers' restoring force, η is the liquid medium viscosity, and r is the particle radius. Before solving the equation of motion we first derive the expression for $F_{ACEO+DEP}$ as a function of the AC electric field.

An AM modulated electric field can be written as a function of time:

$$E(t) = E_0 e^{i\omega_M t} e^{i\omega_{DEP} t} \tag{12}$$

where ω_M is the AM frequency and ω_{DEP} is the DEP working frequency. According to Eq. (1), the DEP force on a spherical probe particle is:

$$F_{DEP} = 2\pi r^3 \varepsilon_0 \varepsilon_m \, \mathrm{Re}\{K(\omega_{DEP})\} \nabla {E_0}^2 e^{i2\omega_M t} e^{i2\omega_{DEP} t} \tag{13}$$

For $\omega_{DEP} > 1\mathrm{kHz}$, when the particle is too sluggish to respond to the high frequency of the alternating voltage, Eq. (13) is simplified by omitting the last term $e^{i2\omega_{DEP} t}$ to:

$$F_{DEP} = 2\pi r^3 \varepsilon_0 \varepsilon_m \, \mathrm{Re}\{K(\omega_{DEP})\} \nabla E_0^{\,2} e^{i2\omega_M t} \tag{14}$$

According to Eq. (6), the ACEO force on a spherical probe particle is:

$$F_{ACEO} = 6\pi r \varepsilon_0 \varepsilon_m \lambda_D E_0^{\,2} e^{i2\omega_M t} e^{i2\omega_{ACEO} t} \sin\theta\cos\theta \tag{15}$$

where θ is the intersection angle between the direction of the electric field and the reference electrode surface. The $\sin\theta$ and $\cos\theta$ terms are for the normal and tangential components of the electric field, respectively.

For $\omega_{ACEO} > 1\mathrm{kHz}$, when the particle is too sluggish to respond to the high frequency of the alternating voltage, Eq. (15) is simplified by omitting the last term $e^{i2\omega_{ACEO} t}$ to:

$$F_{ACEO} = 6\pi r \varepsilon_0 \varepsilon_m \lambda_D E_0^{\,2} e^{i2\omega_M t} \sin\theta\cos\theta \tag{16}$$

By combing Eq. (14) and Eq. (16), the total electrokinetic force from ACEO and DEP is time-dependent:

$$F_{ACEO+DEP} = F_0 e^{i2\omega_M t} \tag{17}$$

where the amplitude is $F_0 = 2\pi r^3 \varepsilon_0 \varepsilon_m \, \mathrm{Re}\{K(\omega_{DEP})\} \nabla E_0^{\,2} + 3\pi r \varepsilon_0 \varepsilon_m \sin 2\theta \, \lambda_D E_0^{\,2}$.

Now we return to the motion equation. We rewrite the equation as:

$$F_{external} = m\ddot{x} = F_0 e^{i2\omega_M t} + k_{OT} x + 6\pi\eta r \dot{x} \tag{18}$$

The general solution to a driven, damped harmonic oscillator model goes as:

$$x = \frac{F_0 e^{i(2\omega_M t - \varphi)}}{\sqrt{(k_{OT} - 4m\omega_M^{\,2})^2 + (6\pi\eta r)^2 (2\omega_M)^2}} \tag{19}$$

where $\varphi = \arctan\left(\frac{12\pi\eta r\omega_M}{k_{OT} - 4m\omega_M^{\,2}}\right)$ is the phase delay.

Under experimental conditions of $k_{OT} >> 4m\omega_M^{\,2}$ and $k_{OT} >> 12\pi\eta r\omega_M$, the general solution is approximated as:

$$k_{OT} x = F_0 e^{i2\omega_M t} = F_{ACEO+DEP} \tag{20}$$

The calibration of the spring constant k_{OT} was completed by oscillating a particle in water in the absence of an external electric field, as discussed in section 2.3.5. Both the amplitude and phase of the particle displacement are used to determine the spring constant of the optical trap. Once the system is properly calibrated, we convert displacement readings at twice the AM frequency to absolute forces by Eq. (20).

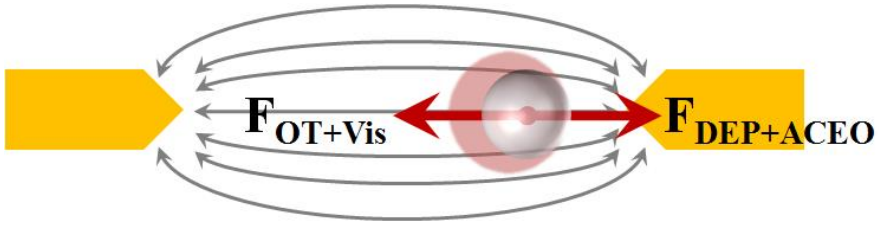

Fig. 15 Top view of optical tweezers-based force sensor

A polystyrene bead (grey sphere) deviates from the focal point of the optical tweezers within the trapping volume (pink disk) under the effects of the DEP force and ACEO flow. When the particle is in steady state, the total electrokinetic forces $F_{DEP+ACEO}$ (red arrow pointing to the right) are balanced by the optical tweezers' restoring force F_{OT} and the liquid medium's viscous damping force F_{Vis} (red arrow pointing to the left).

3.2.2 Experimental hardware connections and control by Labview

Shown in Fig. 16 are connections between hardware and software components of the experiment. The Labview software writes to the function generator's frequency address, sending a command of generating a sinusoidal oscillation with a variable frequency that starts from 1 kHz. The amplitude of the oscillation is manually set to be of 3Vpp to produce sufficiently strong electrokinetic forces. This oscillation wave is amplitude modulated at the frequency of 37 Hz. It is at least two orders of magnitude lower than the DEP frequency to avoid interference. The AM modulated AC voltage is applied to the pair of the opposing microelectrodes, and the AM frequency is fed to the lock-in amplifier as the reference frequency. The particle motion detected by a QPD is collected by the lock-in amplifier to extract

E^2-dependent forces. The Labview software reads both output portals of the lock-in amplifier to obtain information for the voltage amplitude and the phase delay. The voltage information can be converted into force information by procedures described in Section 2.3.4.

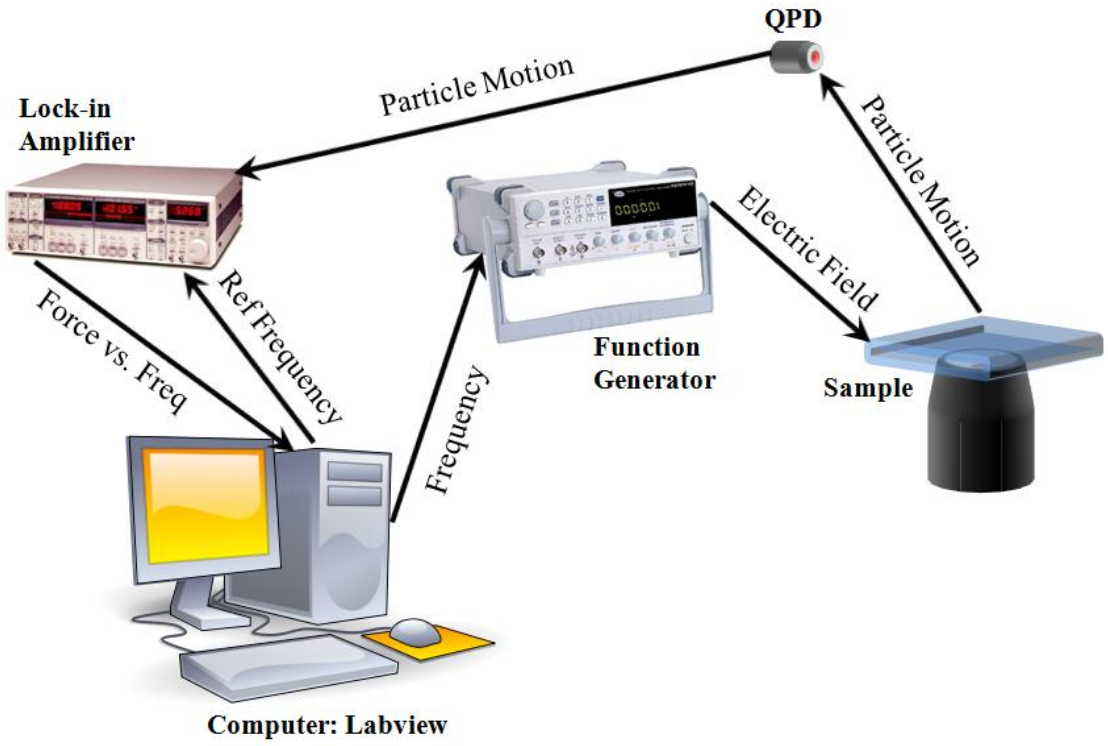

Fig. 16 Experimental hardware connections and control by Labview software

3.2.3 Trapping an individual particle with optical tweezers

We locate the position of the electrode gap under the microscope objective lens with a bright view CCD camera. From there we search for individual particles suspended at a height of 10~20μm above the glass surface, by moving the microscope stage back and forth. The height restriction was chosen to optimize the effectiveness of the optical trapping and to avoid the wall effect on the particle motion. Once

finding a particle near the gap, we slowly move the stage and ultimately position the trapped particle to the designated location for measurements.

3.3 Results and discussion

3.3.1 Analysis of E^2-dependent forces

At any given location in the sample chamber, we define the "apparent crossover frequency" as the frequency at which F_{E^2} in Eq.(20) reverses sign (the frequency of zero E^2-dependent force). The amplitude and phase outputs of a lock-in amplifier are shown in Fig. 17 and Fig. 18. In amp vs. freq plots, the force magnitude decreases monotonically before reaching a minimum and then increases monotonically. In phase vs. freq plots, the relative phase remains steady before shifting by $180°$ and then remains steady again. We search for the frequency, at which the force amplitude reaches minimum and force phase switches by 180°.

Near the electrode tips, both DEP (large gradient of the square of the electric field) and ACEO (abundant counterions) are strong, as shown in Fig. 17. Due to the presence of ACEO, apparent crossover frequencies measured near electrode tips may differ from the DEP crossover frequency.

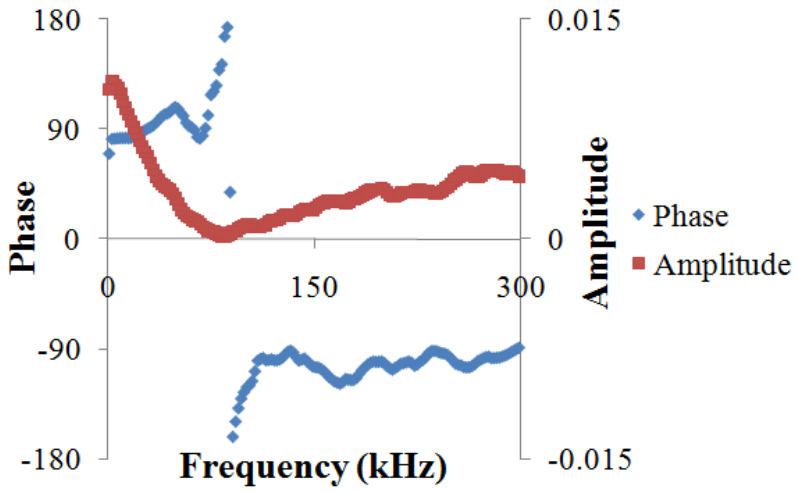

Fig. 17 Data analysis for strong E^2-dependent forces

Apparent crossover frequency measured of a 483 nm polystyrene particle at the position (x = 11.0 μm, z = 7 μm).

When the signal is small, we observe noisy curves in both relations of amp vs. freq and phase vs. freq. And it becomes hard for the lock-in amplifier to "capture" the weak signal that oscillates at twice the modulation frequency. Two approaches were taken to address this technical issue. First, by increasing the lock-in amplifier's integral time from 0.1s to 1s, we improved the signal/noise ratio. Second, by scanning force vs. frequency "less often", (eg. by increasing the scanning interval from 2 kHz to 20 kHz), we "manually" smooth out the data curve through sacrificing the frequency resolution moderately, as shown in Fig. 18.

Near the z axis, both DEP (diminishing gradient of the square of the electric field) and ACEO (undetectable due to geometrical symmetry) are weak. Due to the presence of ACEO, apparent crossover frequencies measured near the z axis reveal the actual value of the DEP crossover frequency.

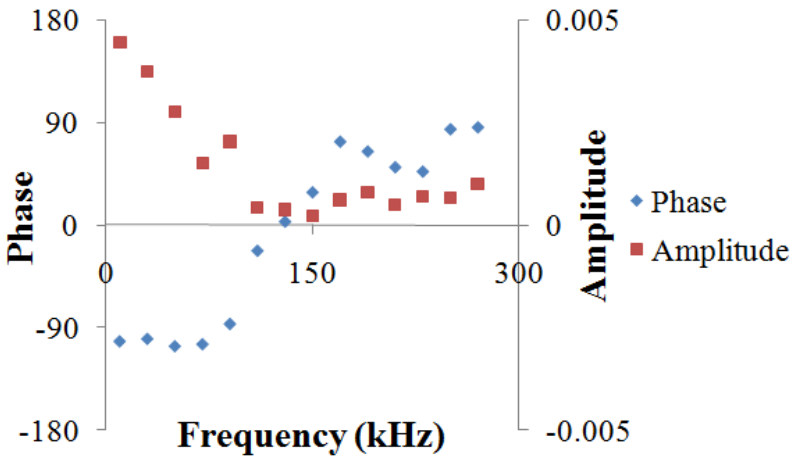

Fig. 18 Data analysis for weak E^2-dependent forces

Apparent crossover frequency measured of a 483 nm polystyrene particle at the position (x = 3.1 μm, Z = 9 μm).

3.3.2 Isolated DEP crossover frequencies for polystyrene probes

The apparent crossover frequency equals the DEP crossover frequency only when the ACEO contribution to F_{E^2} is zero. Since the ACEO force is spatially- as well as frequency-dependent, the apparent crossover frequency varies with location in the chamber. Measured values of apparent crossover frequencies varied from several kHz to hundreds of kHz, indicating that the DEP force and the ACEO force were both present, as shown in Fig. 19. If DEP were dominant over the effect from ACEO, we would obtain same measured values of apparent crossover frequencies at any location we place the probe particle. On the other hand, if ACEO were dominant over the effect from DEP, we wouldn't observe the phenomenon of crossover.

To isolate the DEP crossover frequency from ACEO effects, we measure the frequency of zero force at locations approaching the z axis. In this region, by symmetry, ACEO flows primarily along the -z direction; and thus doesn't contribute to the force measurement in the x direction. However, also by symmetry, $\nabla|\vec{E}|^2$ and

hence F_{DEP} in the x direction approach zero along the z axis, which makes the force measurement difficult. To compromise the needs of minimizing the contribution from ACEO and of ensuring reliable force detection, we determined the DEP crossover freqency as the limiting value of the frequency of minimum force and force reversal as the z axis was approached asymptotically, as shown in Fig. 19.

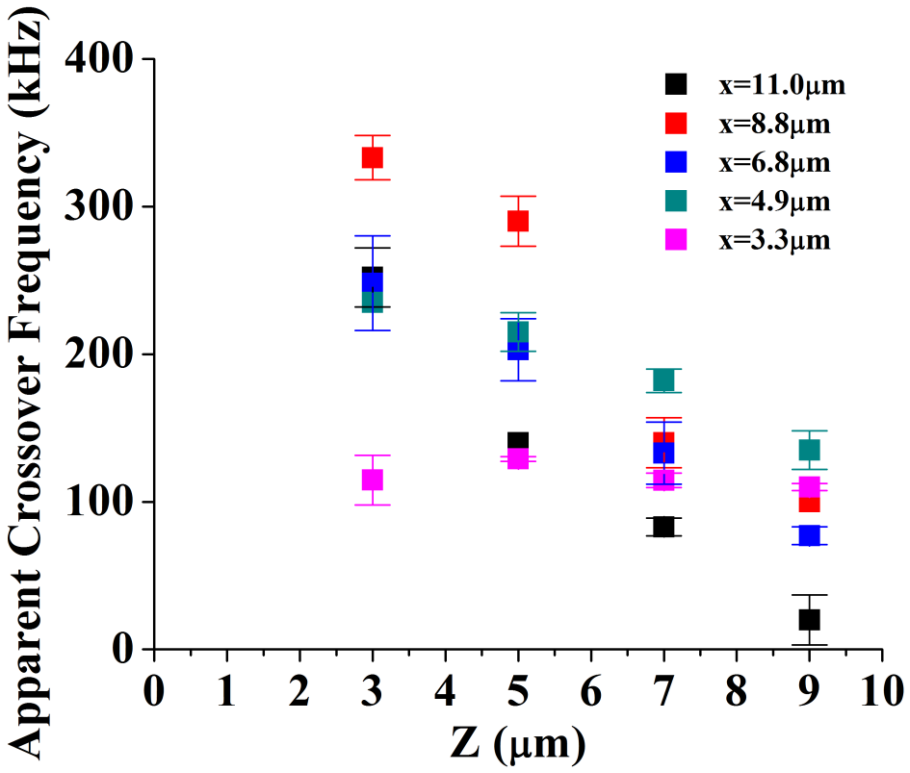

Fig. 19 Apparent crossover frequencies

Apparent crossover frequencies measured of a 483 nm particle at different locations in the sample chamber. The DEP crossover freqency was determined by the limiting value of the apparent crossover frequency at x = 3.3 μm.

The ACEO-free DEP crossover frequencies for a set of submicron- and micron-sized polystyrene beads were found at 25 ℃: 151.4 ± 12.2 kHz (370 nm), 117.0 ± 8.2 kHz (483 nm), 71.8 ± 10.5 kHz (650 nm), 50.7 ± 10.7 kHz (750 nm), 23.7 ± 4.0 kHz (1050 nm) and 11.4 ± 2.6 kHz (1450 nm). The size of the particles were measured in diameter.

Further analysis of the electrokinetics of DEP will be discussed in Chapter 4.

3.3.3 Isolated AC electroosmotic flow

The above polystyrene particle are used as force probes at their isolated DEP crossover frequencies, when DEP vanishes and the E^2-dependent force is solely contributed by ACEO. The AC electroosmotic force experienced by an individual particle is therefore obtained from the following reduced form:

$$F_{E^2}(f_C) = F_{ACEO}(f_C) \tag{21}$$

By extracting the particle displacement at its DEP crossover frequency and applying Hooke's law with precalibrated spring constant of optical tweezers, we obtain the force magnitude. The calculation of v_x from F_{ACEO} by Stokes' law is corrected for the hydrodynamic drag on the particle by the glass substrate using Faxén's law:[34]

$$F_{ACEO} \cong 6\pi\eta r v_x \left(1 - \frac{9}{16}\frac{r}{h} + \frac{1}{8}\frac{r^3}{h^3}\right)^{-1} \tag{22}$$

where F_{ACEO} is the x-component of the frictional force of the fluid on the particle, η is the fluid's dynamic viscosity, r is the radius of the spherical particle, and h is the distance between the center of the particle and the non-slip wall, as shown in Fig. 20.

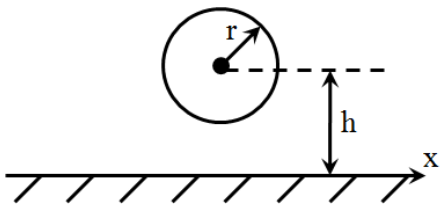

Fig. 20 A spherical particle near to a non-slip wall

Further analysis of the electrokinetics of ACEO will be discussed in Chapter 5.

3.4 Conclusions

By use of optical tweezers-based single-particle force spectroscopy with standard phase-sensitive detection, we separated ACEO and DEP of a probe particle. This is based on the concept that ACEO is spatially dependent whereas the DEP crossover frequency is not. We isolated DEP by probing its force in an area where ACEO is negligible due to the geometrical symmetry. This enables the determination of ACEO-free DEP crossover frequencies of individual probe particles. In a separate experiment, we isolated ACEO by measuring its force on a probe particle at the particle's DEP crossover frequency, at which DEP vanishes.

4 LOW-FREQUENCY DIELECTROPHORETIC RESPONSE OF A COLLOIDAL PARTICLE

4.1 Introduction

As described in Chapter 1, dielectrophoresis (DEP) is a frequency dependent directed motion of electrically polarizable particles in a nonuniform AC electric field.[9,10,11] For a charged colloidal particle suspended in liquid medium, the direction of the motion can reverse at a specific frequency, namely the crossover frequency f_C.[9,10] This direction reversal is believed to be due to the relaxation of the electrical double layer that forms at the particle-liquid interface.[11] The physical properties of the counterion movement and the relaxation of the double layer were explained in the theory proposed by Schwarz for low frequency dielectric dispersion (α-relaxation)[35] of colloidal particles in aqueous suspensions.[35] However, the detailed contribution of the double layer relaxation to DEP has not been systematically investigated. Specifically, among the major parameters that affect the process of α-relaxation, only the influence related to the particle size has been examined.[32,36,37] In order to further test the applicability of Schwarz's model to explain DEP, we apply the technique of optical tweezers-based DEP force spectroscopy to examine the effect of liquid medium viscosity and temperature. In contrast to traditional means of particle image velocimetry (PIV),[36] we use single particle DEP force spectroscopy to accurately determine the DEP crossover frequency while avoiding the effects of AC electroosmosis.[28,29,30,31] By inspecting a single particle's DEP crossover frequency as a function of particles radius, medium viscosity and temperature, we aim to evaluate the role of α-relaxation in the frequency dependence of DEP.

4.1.1 α-relaxation

The α-relaxation described by Schwarz models the counterion movement to be diffusion-controlled within the electric double layer. The double layer is polarized by the external AC field, and therefore has a concentration gradient of the counterions. Accordingly the double layer relaxation time is determined by the diffusion rate of the counterions. For particles that satisfy the condition $r \gg \lambda_D$, namely the particle size is much larger than the Debye length, the α-relaxation time is[35]

$$\tau_\alpha = \frac{1}{\omega_\alpha} = \frac{r^2}{2D} \tag{23}$$

where r is the particle radius, and D is the counterion diffusivity. If we assume the counterion diffusivity follows the Stokes-Einstein equation, the frequency of α-relaxation can be rewritten as

$$\omega_\alpha = \frac{1}{\tau_\alpha} = \frac{k_B T}{3\pi a r^2 \eta}, \tag{24}$$

where k_B is the Boltzmann constant, T is temperature and a is the counterion radius. Eq.(24) shows the frequency of α-relaxation to be inversely proportional to the square of the particle radius, and medium viscosity, and proportional to temperature.

4.1.2 DEP and α-relaxation

According to the Clausius-Mossotti relation shown in Eq. (2), the DEP force direction reversal occurs at the frequency when the complex permittivity of the suspended particle with its associated double layer exactly matches that of the suspension medium. According to Schwarz, the complex permittivity contributed by the double layer is[35]

$$\tilde{\varepsilon}_{DL} = \frac{1}{1+\omega\tau_\alpha}\frac{e^2 r\sigma_0}{k_B T}, \tag{25}$$

where ω is the angular frequency, e is the elementary charge, and σ_0 is the surface density of charge (ions per unit area). By omitting the intrinsic permittivity of the colloidal particle $\tilde{\varepsilon}_{p0}$, which is orders of magnitude smaller than the typical values of $\tilde{\varepsilon}_{DL}$ for micron sized colloidal particles in water, we define

$$\tilde{\varepsilon}_p = \tilde{\varepsilon}_{p0} + \tilde{\varepsilon}_{DL} \cong \tilde{\varepsilon}_{DL} = \frac{1}{1+j\omega\tau_\alpha}\frac{e^2 r\sigma_0}{k_B T}, \tag{26}$$

By rewriting the complex permittivity of the suspended particle and the suspension medium in the traditional form of $\tilde{\varepsilon}(\omega) \equiv \varepsilon - j\cdot(\sigma/\omega)$, we have

$$\tilde{\varepsilon}_p = \varepsilon_p - \frac{j}{\omega}\sigma_p = \frac{1}{1+\omega^2\tau_\alpha{}^2}\frac{e^2 r\sigma_0}{k_B T} - \frac{j}{\omega}\frac{\omega^2\tau_\alpha}{1+\omega^2\tau_\alpha{}^2}\frac{e^2 r\sigma_0}{k_B T} \tag{27}$$

where $\varepsilon_p = \frac{1}{1+\omega^2\tau_\alpha{}^2}\frac{e^2 r\sigma_0}{k_B T}$ and $\sigma_p = \frac{\omega^2\tau_\alpha}{1+\omega^2\tau_\alpha{}^2}\frac{e^2 r\sigma_0}{k_B T}$, and

$$\tilde{\varepsilon}_m = \varepsilon_m - j\frac{\sigma_m}{\omega} \tag{28}$$

By solving the Clausius–Mossotti relation at the DEP crossover frequency, we obtain the angular DEP crossover frequency as

$$\omega_{DEP} = \frac{1}{2\pi}\sqrt{\frac{(\sigma_p-\sigma_m)(\sigma_p+2\sigma_m)}{(\varepsilon_m-\varepsilon_p)(\varepsilon_p+2\varepsilon_m)}}, \tag{29}$$

where Eq.(27) and (28) are applied.

Or, the DEP crossover frequency is $f_{DEP} = \frac{\omega_{DEP}}{2\pi}$.

Eq. (29) indicates that the DEP crossover frequency depends on the particle size, temperature and the counterion diffusivity.

4.2 Results and discussions

4.2.1 Particle size dependence of DEP crossover frequency

By measuring the DEP force on a single particle as a function of the frequency of the applied electric field with the technique described in Section 3.3.2, we determine the particle's DEP crossover frequencies. For samples at 27℃ we obtained the DEP crossover frequencies for a group of differently sized particles, as shown in Fig. 21 and Table 1. The particles were polystyrene microsphere suspensions in water (Thermo Scientific, 5000 Series), originally packaged at 10% solids by weight, and diluted with DI water in volume by a factor of 10,000. The sample preparation follows the description in Section 2.1.1 and 2.1.2.

The relation between the DEP crossover frequency and the particle size was plotted in the logarithmic scale to examine the power law dependence. The slope in the graph, which indicates the exponent of the power relation, is close to -2 for particles with sizes larger than 1 μm; however, the slope appears to be less negative for submicron particles. The best fit for the entire data set gives an exponent of -1.8 ± 0.1, as shown in Fig. 21. Similar results were shown in previous experiments indicating the "-2" power dependence.[11,36] The agreement between the exponents of the power law dependence seems to suggest that ω_{DEP} coincides with ω_{α}, since the latter also has a "-2" power dependence as shown in Eq. (24). However, the diffusivity of the counterions within the double layer thus calculated from the experiments with Eq. (24) ($\sim 9\cdot10^{-8} m^2/s$) would be 10 times larger than the free proton diffusivity ($\sim 9\cdot10^{-9} m^2/s$) in water.[38] Instead, we use Eq. (29) to evaluate ω_{DEP}.

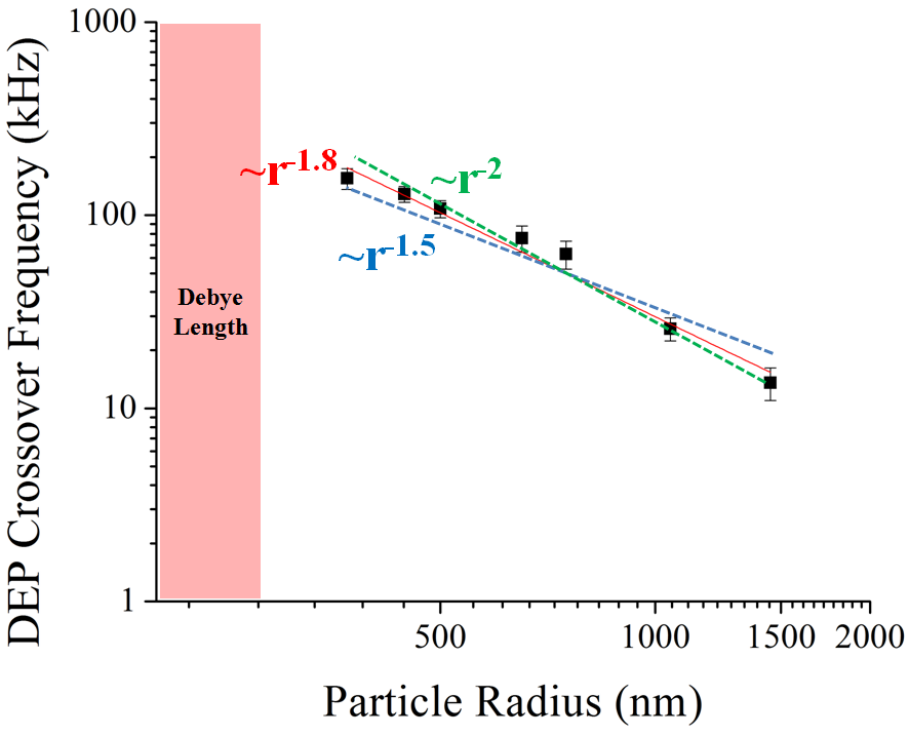

Fig. 21 DEP crossover frequency vs. particle size

DEP crossover frequency as a function of particle size in DI water at 27 ℃. The power law fitting of the data is shown by the red trendline. The exponent is -1.8±0.1. The power law relation with an exponent of -1.5 is shown by the blue dash trendline. The power law relation with an exponent of -2 is shown by the green dash trendline. The pink area indicates the scale smaller than the Debye length.

r (nm)	370	445	500	650	750	1050	1450
r CV(%)	≤3	≤3	≤3	≤5	≤4	≤5	≤5
f_C (kHz)	155.0	128.8	108.0	76.0	63.0	25.9	13.9
Δf_C (kHz)	18.9	12.0	11.0	11.9	10.4	3.5	2.6

Table 1 DEP crossover frequencies for different-sized polystyrene beads

By solving Eq. (29) with the measured f_{DEP}, as shown in Appendix D, we obtained a surface charge density of $\sigma_0 = 10^{16}/m^2$, which is a typical value for the electrical double layer on polystyrene latex particles; however, is one order of magnitude lower than the typical value for the "undisassociated counterions" given by

Schwarz.[35] Eq. (29) would predict an exponent of the power law dependence of ω_{DEP} on r to be within the range of -1 to -1.5, as shown in Eq. D (1), which disagrees with the experiment, as shown in Fig. 21.

4.2.2 Medium viscosity dependence of DEP crossover frequency

By following the arguments leading to Eq. (29), we expect from Eq. D (1) that ω_{DEP} to be proportional to ω_α. As ω_α is inversely proportional to the medium viscosity, we examine the dependence of DEP on viscosity by measuring the dielectrophoretic response of a 750 nm particle in different concentrations of glycerol in DI water. In essence, we are interested in understanding how viscosity may affect the proton diffusion in aqueous medium. With the viscosity in the range of 0.8 mPa·s to 8 mPa·s at 27℃ by adding 0 to 40% (volume) of glycerol to the DI water, the medium permittivity was in the range of 60~78. The medium conductivity of the glycerol solutions was found to be in the same range of 1~2 μS/cm. The DEP crossover frequency as a function of the medium viscosity is shown in Fig. 22, where the inverse proportionality agrees with the α-relaxation, suggesting the Stokes-like viscosity dependence of the proton diffusion.

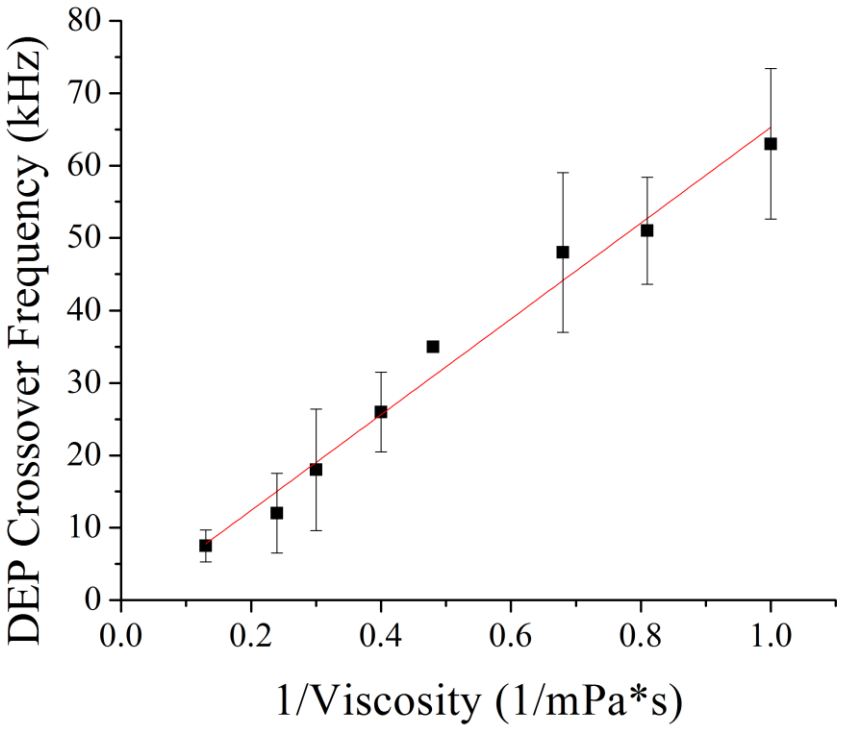

Fig. 22 DEP crossover freqeuncy vs. 1/Visocisty

DEP crossover freqeuncy of a 750nm polystyrene particle as a function of 1/(solvent viscosity) at 27 ℃. The linear fitting of the data is shown by the red trendline. The slope value is 64.9 ± 1.7Pa.

4.2.3 Temperature dependence of DEP crossover frequency

To examine the effect of temperature on DEP, we investigated the DEP crossover frequency of a 750 nm particle. We plot the crossover frequency as a function of the combined parameter of T/η (Temp/Vis), to account for the change in medium viscosity by temperature. The results from DI water for temperature in the range of 27 ℃ to 42 ℃ (blue shade area) and from glycerol solutions at 23 ℃ and at 27 ℃ (pink shade area) are shown in Fig. 23.

A linear relation at low T/η and a superlinear relation at higher T/η suggest that the proton diffusion doesn't follow the Stokes-Einstein relation. The superlinear relationship of diffusivity as a function of temperature was proposed by Schwarz as a consequence of activated counterion migration along the particle surface. According

to Schwarz, “since the fixed charges on the surface of the sphere are discretely distributed, the electric potential is changing periodically parallel to the surface. A counterion within the double layer must overcome potential barriers in order to follow an applied electric field. The height of the potential wall multiplied by the charge of the counterion yields the additional activation energy.” The temperature range of our experiment was too narrow to give an accurate determination of the activation process.

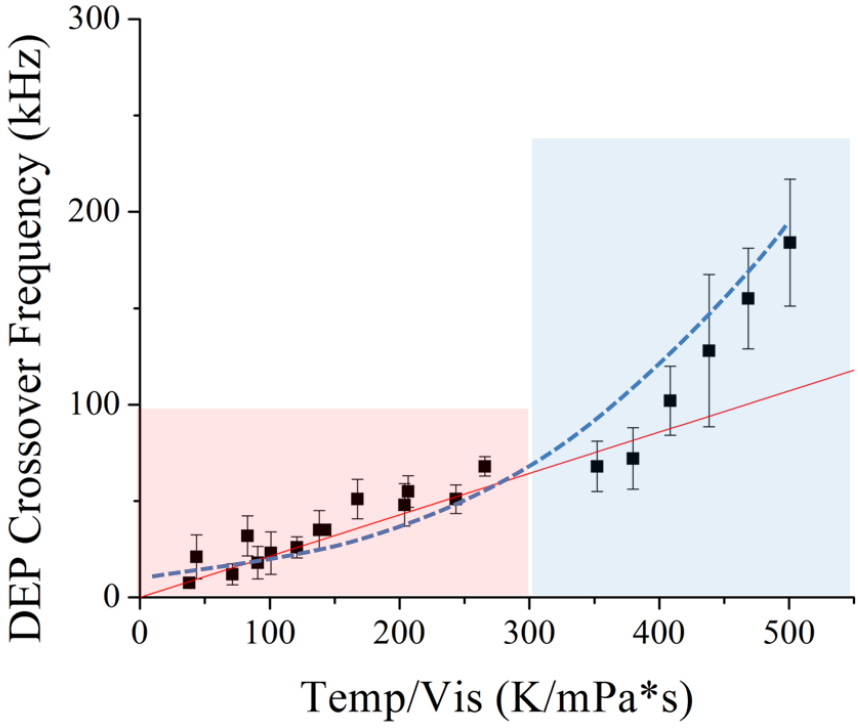

Fig. 23 DEP crossover freqeuncy vs. Temperature/Viscosity

DEP crossover freqeuncy of a 750 nm polystyrene particle as a function of the ratio of temperature/viscosity. The linear fitting of the low T/η data is shown by the red trendline. The superlinear relation is shown by the blue dash trendline.

4.3 Conclusions and outlook

The experiments that examined the dependence of the DEP crossover frequency on the particle size, the medium viscosity and temperature allowed us to evaluate the

roles of the counterion diffusion in the dielectrophoretic response of colloidal particles.

From the particle size dependence, we discovered a power law dependence of the DEP crossover frequency on particle radius with the exponent -1.8 ±0.1. While the result is close to the "-2" power dependence seen in the α-relaxation, the counterion diffusivity thus calculated was one order of magnitude higher than the free proton diffusivity. Using the dielectric function from the Schwarz model of a charged particle in the Clausius-Mossotti relation, we can solve for the DEP crossover frequency as a function of particle size and surface charge density. While the value of the surface charge density was reasonable, the exponent of the power law dependence on particle size was different from our experiments.

We also examined the dependence of the DEP crossover frequency on the medium viscosity. We observed an inversely proportional relation between the crossover frequency and the viscosity, which may suggest a Stokes-like process for the proton diffusion.

In studying the influence of temperature, we observed a nonlinear increase in the DEP crossover frequency with the increase of temperature. The relation being possibly related to the activation process of the double layer; may be better addressed by experimenting with a wider temperature range.

Accurate experiments with the technique of optical tweezers-based force spectroscopy enabled advancements of understanding the double layer migration in DEP. Comparisons between our experiments and the Schwarz model for the low frequency counterion relaxation suggests the significance of the double layer diffusion in DEP, however discrepancies occurred. Since the Schwarz model was established

under the condition of $r \gg \lambda_D$, future experiments in high salt solutions may better quantify the functional relations of the DEP crossover frequency.[†]

[†] A supplement clarifying the association of a high frequency dispersion of the electrical double layer the relaxation in DEP is shown in Appendix E.

5 MAPPING OF THE FLOW FIELD OF AC ELECTROOSMOSIS

5.1 Introduction

AC electroosmosis (ACEO) is a unidirectional fluid flow driven by the movement of ions near the surfaces of electrodes in an AC electric field.[12] Having advantages over mechanical pumps for lab-on-a-chip devices, ACEO has broad applications in microfluidics for particle transport, sorting,[13,21] and positioning.[20] However, the lack of a full understanding of the mechanism has impeded progress in designs of reliable ACEO-based devices.[7,39] In certain cases electrokinetic theory has been unable to account for experimental results. For example, recent models predict orders-of-magnitude higher flow velocities compared to measurements.[39] In addition, an experimentally observed flow reversal has not been satisfactorily explained theoretically.[7,39,40] The reconciliation of experiment with theory has been hindered by the fact that ACEO is often complicated by other electrokinetic effects, in particular by dielectrophoresis (DEP).[28,29,30,31,32,33] DEP is a force experienced by polarizable particles in a nonuniform electric field. In particle-image velocimetry (PIV) experiments, if nonuniform electric fields are present, it is difficult to distinguish the contributions of ACEO from those of DEP of the imaged particles.[31,41] We present a technique that distinguishes ACEO from all the other coexisting electrokinetic effects, including DEP.

5.2 Experimental details

5.2.1 Frequency dependence of AC electroosmosis

Following the isolation method of ACEO described in Section 3.3.3, we studied different sized probe particles at their DEP crossover frequencies to obtain the ACEO flow velocity as a function of frequency. In this plot, the flow velocity was measured at the same location (x = 10 μm, z = 3 μm) in the gap area between the electrode tips. The location was near the electrode tip (in the x direction) and the glass surface (in the z direction), and therefore was close to where the ACEO flow was originated. Fig. 24 shows a maximum magnitude of the x-component of the flow velocity $|v_x|$ at ~120 kHz. It was consistent with the data of Wang et al.[42] They demonstrated 120kHz as the most efficient frequency in a particle-free ACEO-based micropump, by using fluorescent dye molecules to trace the flow. In PIV experiments conducted by Green et al. with 577 nm tracer particles, the maximum flow strength was found to occur at a much lower frequency of ~10 kHz,[43] with DEP as a possible complicating factor. A similar with video microscopy on 2 μm latex particles gave an even lower frequency of ~100 Hz for the maximum flow strength,[28] which was possibly caused by even stronger complications caused by DEP on larger probe particles.

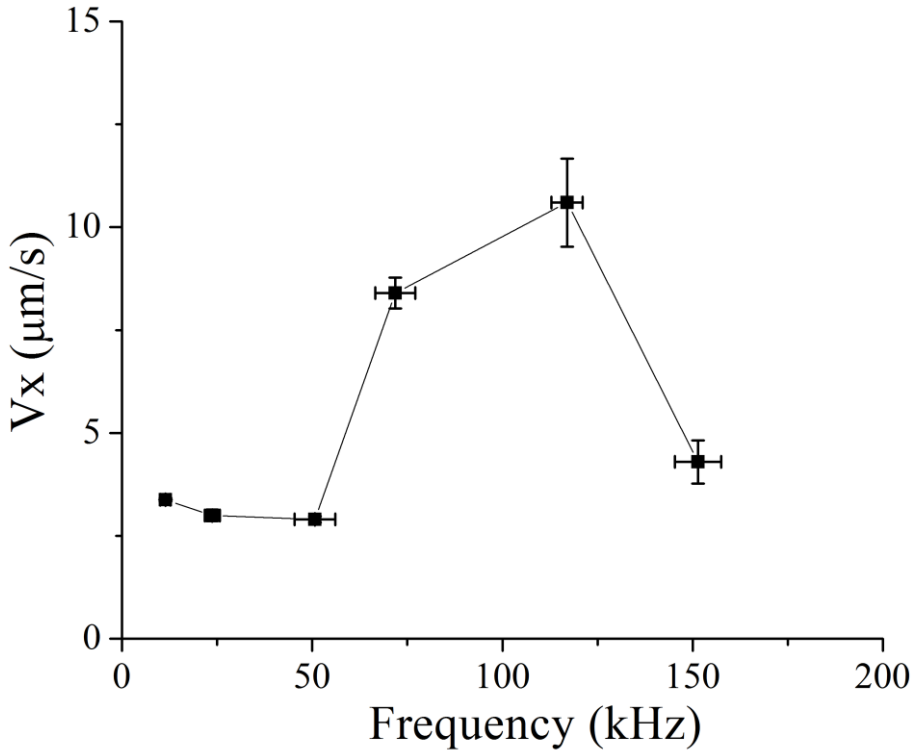

Fig. 24 X-component of the ACEO flow velocity vs. frequency

X-component of the ACEO flow velocity as a function of frequency at a fixed position (x ≅ 10μm, z ≅ 3μm). v_x is defined as positive moving away from the midpoint along the x-axis. The lines connecting the data points are merely to guide the eye.

5.2.2 Spatial dependence of AC electroosmosis

In the above section, multiple particles with different sizes were used as ACEO force probes at their DEP crossover frequencies to discover the frequency dependence of ACEO. Analytically, if a single probe particle (as a force probe at its DEP crossover frequency) is applied at different locations in the gap area between the electrode tips, it will reveal the spatial distribution of the flow. In Fig. 25 we mapped the spatial dependent v_x with a 483nm probe when ACEO was driven at the particle's crossover frequency of ~120kHz.

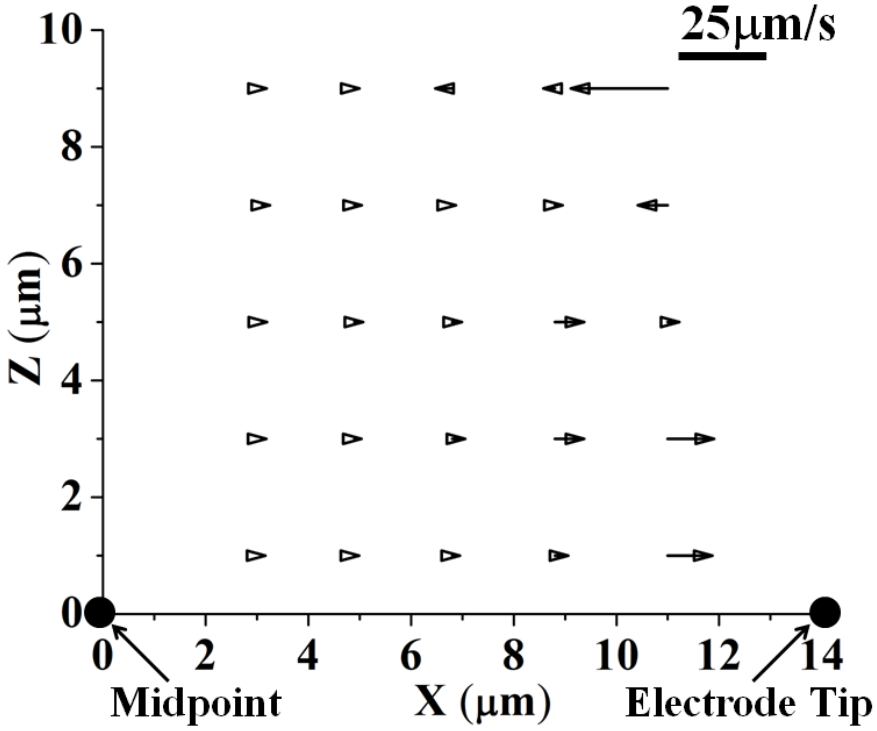

Fig. 25 X-component of the ACEO velocity field in the x-z plane
The left end of the x-axis is the midpoint of the electrode gap, and the right end is the electrode tip.

We examined the other two components of the ACEO flow velocity v_y and v_z, in the y and z directions, respectively, by utilizing the zero divergence of the flow velocity due to the incompressibility of the liquid medium.

$$\nabla \cdot \vec{v} = \frac{\partial v_x}{\partial x} + \frac{\partial v_y}{\partial y} + \frac{\partial v_z}{\partial z} = 0 \tag{30}$$

The magnitude of the y-component of the flow velocity $|v_y|$ is zero in the x-z plane due to the geometrical symmetry of the electrodes. Given by the continuity of the flow velocity field, we infer that the first order derivative $\partial v_y/\partial y$ has to be zero where $|v_y|$ reaches minimum/zero. Eq. (30) in the x-z plane is therefore reduced to

$$\frac{\partial v_x}{\partial x} + \frac{\partial v_z}{\partial z} = 0 \tag{31}$$

By utilizing the distribution of v_x found within the gap area, and applying Dirichlet boundary conditions [$v_x = 0$ and $v_z = 0$ at $z = 0$, and $v_x = 0$ at $x = 0$] to Eq.(31), we calculated a complete ACEO velocity field (v_x, v_z) in the x-z plane, as shown in Fig. 26. The numerical approach is demonstrated in Appendix F.

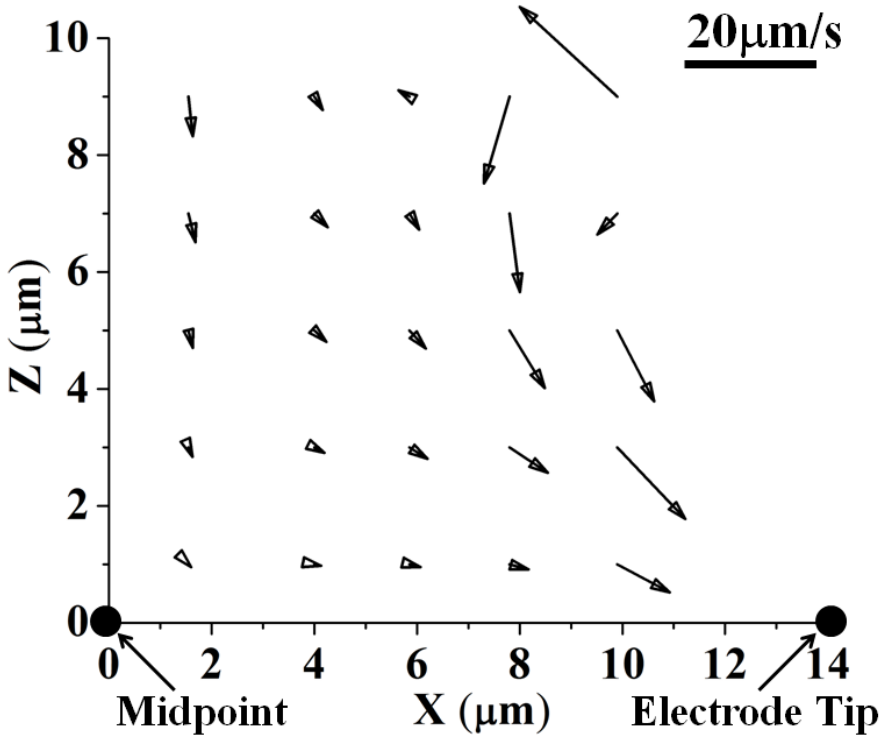

Fig. 26 ACEO velocity field in the x-z plane

ACEO velocity field calculated from Fig. 25 using Eq. (31). By symmetry, $v_y=0$ in the x-z plane. The left end of the x-axis is the midpoint of the electrode gap, and the right end is the electrode tip.

5.3 Results and discussion

5.3.1 2D mapping of the AC electroosmotic flow field

We discovered the macroscopic distribution of the ACEO flow velocity, which was faster near the electrodes and weaker near the z axis. This agrees with the electrokinetic theory that ACEO is driven by the counterion migration near the electrode surface.

5.3.2 Comparison of ACEO between experiments and theory

The Helmholtz-Smoluchowski velocity calculated from Eq. (5) is 354 μm/s. We assume the relative permittivity of the medium to be $\varepsilon_m = 78$, and medium viscosity to be $\eta = 1$ mP·s. The Debye length was calculated to be $\lambda_D \cong 200$ nm (Appendix C), assuming our medium to be deionized water in equilibrium with atmospheric CO_2, which is consistent with our conductivity measurement. In the COMSOL Multiphysics simulation of the electric field, we defined the voltage across the electrodes to be 3Vpp and the gap between the electrode tips to be 28μm. The two components of the electric field near the electrode tip were calculated by COMSOL Multiphysics (Version 3.5a, as shown in Appendix G) to be $E_t = 0.7\times10^5$ V/m and $E_n = 0.39\times10^5$ V/m. The zeta potential thus calculated from Eq. (4) is 7.6mV, which satisfies the requirement for the Debye-Hückel approximation.

Shown below are detailed calculations based on simulation results of COMSOL Multiphysics.

We calculate $|v| = \frac{\varepsilon_0\varepsilon_m\zeta}{\eta} E_t$ at the position of (x = 14.2μm, z = 200nm)

According to the simulation result of the tangential component of the electric field $E_t(z)$:

$$E_t(x = 14.2\mu m, z = 200nm) \cong 0.7\cdot10^5 V/m$$

According to the simulation result of the normal component of the electric field $E_n(z)$:

$$E_n(x = 14.2\mu m, z = 200nm) = 0.39\cdot10^5 V/m$$

To calculate the zeta potential across the 200nm-thick double layer, we approximated the distribution of the normal field E_n as homogeneous:

$$\varsigma = \int_0^{200\text{nm}} E_z(z)dz \cong E_z(z = 200\text{nm}) \cdot 200\text{nm} = 0.39 \cdot 10^5 \text{V/m} \cdot 200\text{nm} = 0.0078\text{V}$$

Therefore:

$$\left|v\right|_{\text{ACEO}} = \frac{\varepsilon_0 \varepsilon_m \zeta}{\eta} E_t = \frac{8.854 \cdot 10^{-12} \cdot 78 \cdot 0.0078 \cdot 0.7 \cdot 10^5}{10^{-3}} = 354\mu\text{m/s}$$

Limited by the design of the electrode chambers, we weren't able to map the flow field right above the electrodes to capture the strongest ACEO velocity; that is, we were prevented from conducting a direct comparison between measured and calculated values of the Helmholtz-Smoluchowski velocity. To compensate for this limitation, we extrapolated the "Helmholtz-Smoluchowski velocity" from an exponential fitting of the velocity component v_x (z = 1 μm) (measured at the height of 1 μm) as a function of x, as shown in Fig. 27.

$$v_x(x = 14.2\mu\text{m}, z = 1\mu\text{m}) = 0.08 \cdot 1.6^{14.2} \cong 63.3\mu\text{m/s}$$

The extrapolated x-component of the flow velocity at (x = 14.2 μm, z = 1 μm) is in reasonable agreement with the Helmholtz-Smoluchowski velocity $\left|v\right|_{\text{ACEO}} = 354\mu\text{m/s}$. The difference can be explained by noting that $\left|v\right|_{\text{ACEO}}$ is outside the double layer and at a height of 200 nm; and the flow velocity may delay along the z direction.

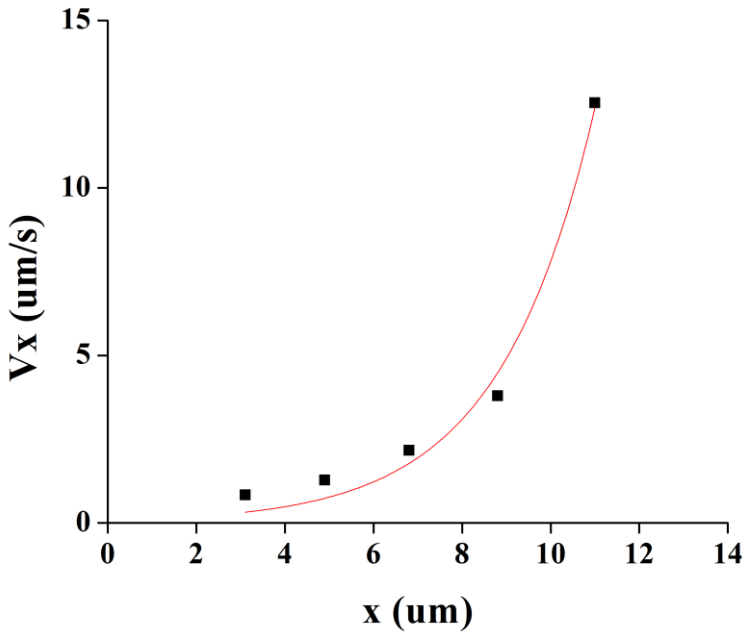

Fig. 27 Extrapolation of the ACEO velocity near the electrode tip

Exponential fitting (red line) of the velocity component v_x(z = 1 μm) as a function of x. The fitting equation is $v_x = 0.08 \cdot 1.6^x$ μm/s.

5.3.3 AC electroosmotic flow field in high electrolyte concentration

We applied the same approach with a 483nm probe to determine the ACEO flow profiles in three electrolyte solutions: (1) 0.2mM KCl at 253kHz, (2) 2mM KCl at 402kHz and (3) 20mM KCl at 1231kHz, which are the DEP crossover frequencies measured for this probe in these media. Among the flow fields thus mapped we observed no reversal of flow direction, suggesting that the previously unexplained phenomenon of ACEO flow reversal above 10kHz in high-salt solutions (~10mM)[7,39,40] may have been due to DEP.

5.4 Conclusions and outlook

By using different-sized charged colloidal particles as probes at their respective crossover frequencies, we measured the frequency dependence of the DEP-free ACEO velocity at a point above the electrodes near one electrode tip. A velocity maximum was found at ~120kHz. Near this frequency, we mapped the spatial distribution of the DEP-free ACEO flow velocity in the vicinity of conducting electrodes for, we believe, the first time. Our method provides a more detailed flow map than the ACEO flow field provided by PIV. This procedure is applicable to 3D mapping by use of a movable optical trap, and is also applicable to other frequencies by use of variously sized probe particles at their DEP crossover frequencies.

6 OPTOPHORESIS OF SWCNTS

6.1 Introduction

In Chapter 4, we established an understanding of the dielectric response of a single spherical colloidal particle with its associated double layer to an external electric field by use of optical tweezers-based force spectroscopy. A different type of response may possibly been seen in geometrically asymmetric particles, such as rod-shaped particles. Single-walled carbon nanotubes (SWCNTs), due to their high aspect ratio hence high polarizability, belong to the type and may display interaction with external fields through translation and rotation. Deemed as potential building blocks for nanoscale electronic devices, SWCNTs have been extensively studied for their manipulation. A recent work confirmed the feasibility of applying positive DEP to trap individual SWCNTs by use of a large gradient of the electric field.[24] Once a tube is trapped, its longitudinal axis will be oriented along the electric field by an electrostatic torque. Hence, not only is the approach able to enhance SWCNTs' local concentration, but their alignment could be accomplished as well.

As much research has been carried out to study the behavior of SWCNTs in electric fields,[44,45] we apply an analogous notion and investigate the "optophoresis" of SWCNTs. We use Raman spectroscopy and fluorescence spectroscopy to characterize the behavior of polarized SWCNTs in the vicinity of an optical trap. Specifically, we examine the notion that SWCNTs can be selectively trapped based on tube chiralities by an optical field gradient,[46] created by a focused laser beam; and anticipate simultaneous aligning of the tubes.

To quantify the trapping and aligning effects experienced by a SWCNT ensemble, we designed an experiment applying optical tweezers and inspecting

resonance Raman emission. We measure the Raman radial breathing mode (RBM) signal of SWCNTs as a function of the trapping laser power for different tube chiralities and concentrations. The research was aimed at achieving more complete understanding of separation/sorting phenomena of individual SWCNTs in an optical field.

6.2 Experimental details

Our experimental design was similar to that of the Osaka group's work[46] where a 633nm laser beam is used for both optical trapping and Raman excitation. We examine the RBM signal as a function of the trapping laser power, after the concentration of trapped SWCNTs reaches equilibrium by diffusion. Naively, the local tube concentration within the trapping volume is expected to increase with increased trapping laser power. Accordingly, its RBM scattering intensity will increase superlinearly with the increased laser power. On the other hand, if the suspended SWCNTs are repelled by the focused laser beam, the RBM scattering intensity will increase sublinearly or even decrease eventually with the increased laser power.

The above statements would be true if the Raman scattering cross-section is independent of the orientation of SWCNTs with respect to the excitation laser polarization. In reality, one cannot ignore the effect of trapping induced SWCNT reorientation. The Raman signal of SWCNTs depends on both their quantity and their orientation relative to the excitation laser beam polarization. We define the tube population to be N, and the angle between the tube's longitudinal axis and the

excitation beam polarization to be θ. The Raman scattering intensity is proportional to N, and to $\cos^4\theta$.[47]

In data analysis, we plot the ratio of Raman scattering intensity/laser power ("Raman/633nm power" or "the R-P ratio" or "the ratio") as a function of laser power (633nm power). For a dried sample of SWCNTs, the ratio doesn't vary with the change in the laser power. For suspended sample of SWCNTs, the ratio increases with the increase of the laser power if the tubes are trapped; and decreases if the tubes are repelled. Therefore, by inspecting the relation of Raman/633nm power vs. 633nm power, we may understand the dynamic behavior of suspended SWCNTs and how they interact with the optical field.

6.2.1 Optical setup

Shown in Fig. 28 is a schematic of optical tweezers coupled with Raman spectroscopy. Optical tweezers were built by use of a 633 nm laser beam. The beam was sent through the top objective lens (100X, N.A. = 1.3), after being expanded to overfill the back aperture of the objective. This ensures maximum trapping stiffness in the direction transverse to the beam propagation. The 633nm laser beam was used for both optical trapping and Raman excitation of suspended SWCNTs. The Raman scattering signal is collected with the same lens and a fiber (M14L05, Thorlabs) that connects to a Raman spectrometer. Two Raman edge filters of 45 ° and 90 °, were used to reject the 633nm trapping/excitation laser light.

We calculated the specifics of the fiber by assuming the focused laser beam has a Gaussian intensity distribution. As shown in Fig. 29, the beam waist w_0 is related to the beam divergence θ (in radians) by the relation of $\theta \cong \frac{\lambda}{\pi w_0}$. θ can be determined

by the focal length of the tube lens (f = 180mm) and the back aperture of the microscope objective, w_z = 4 mm.

$$\theta = \arctan(w_z / f) = 0.0222$$

$$w_0 \cong \frac{\lambda}{\pi\theta} = \frac{633\text{nm}}{\pi \cdot 0.0222} \cong 9\mu\text{m}$$

The numerical aperture is $NA = n \cdot \sin\theta = 1 \cdot \sin(0.0222) \cong 0.022$.

We chose a fiber with a core size of $50\,\mu\text{m}$ and numerical aperture of 0.22 NA (smallest for multimode fiber), to minimize the signal loss.

The concentration and orientation of suspended SWCNTs was quantified bythe RBM Raman scattering intensity and/or the fluorescence intensity.

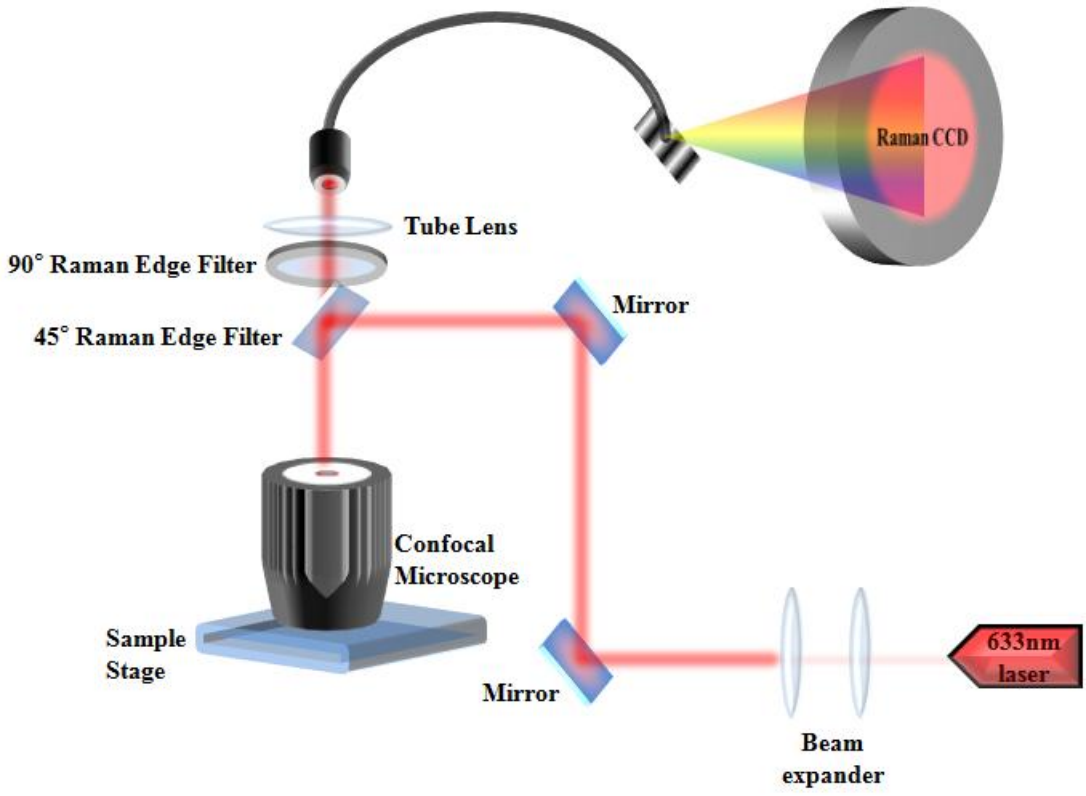

Fig. 28 Optical setup of Raman spectroscopy with optical tweezers

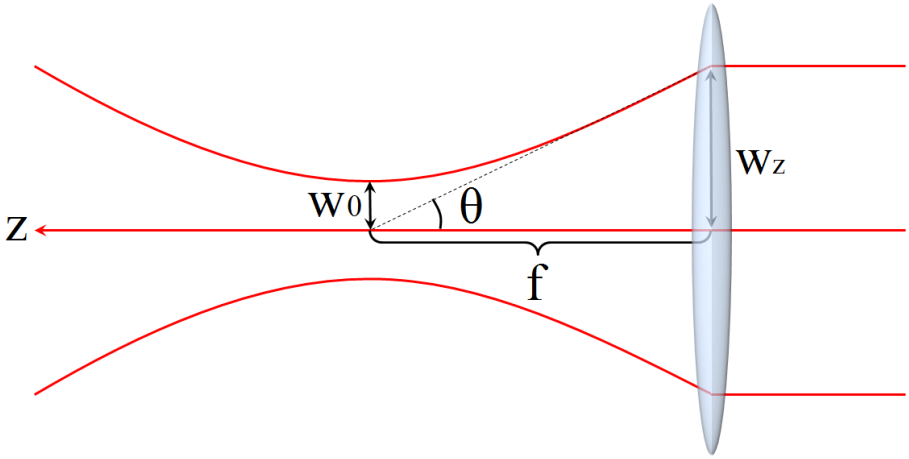

Fig. 29 Diagram of a focused Gaussian beam

The red lines and the red arrow illustrate the propagation of the 633nm laser light focused by the tube lens (blue oval).

6.2.2 SWCNT suspensions for Raman spectroscopy

Two types of chemical agents were used to stabilize SWCNT suspensions: sodium deoxycholate (DOC) or single-stranded DNA (ssDNA). DOC is an anionic dispersing agent used to stabilize CNT in water. The concentration of DOC has to be over 0.5% for a sufficiently strong stabilization effect. ssDNA forms a hybrid with a SWCNT through π-stacking between the bases of DNA and the tube's atomic structures. While we cannot avoid free DOC in DOC-SWCNT suspensions; there possibly can be no free ssDNA in ssDNA-SWCNT suspensions. Therefore, we expect ssDNA-SWCNT suspensions to be a "cleaner" system for Raman detections.

In this study, we used both semiconducting and metallic SWCNT samples. The semiconducting sample contains enriched (7,6) SWCNTs with small amount of other semiconducting chiralities such as (7,5). (7,6) has the E22 transition at 654 nm.[48] (7,5) has the E22 transition at 651 nm excitation.[48] The metallic sample ("GT" sample) contains ssDNA-SWCNTs of chiralities: (9,9), (10,10), (11,5) and (14,2). The metallic sample has the M11 transition in the 610-640 nm range.[48]

We applied resonance Raman spectroscopy for selective detection of SWCNTs with certain chiralities. The excitation wavelength 633 nm corresponds to the energy required for the electronic transition in these chiralities. The RBM peaks are associated with the vibration modes of SWCNTs in the direction of tube diameter. Since the tube diameter is related to its chirality, RBM are chiral specific.

6.2.3 Sample preparation

A sufficiently high concentration of dispersed SWCNT in liquid suspensions was necessary to enhance the Raman signal. The evaluation of the initial number of the SWCNTs within the optical tweezers' trapping volume is shown in Appendix H. Preparation of SWCNT suspensions was similar to the practice introduced with colloid samples, as described in Section 2.1.1. However due to the limited sample amount, diluted samples were made in smaller volumes of 50~200 μL. Rectangular capillary tubes (VitroTubes, 0.10×2.0 mm) were used to collect and store the SWCNT samples. The capillary was cemented on both its open ends using Paraffin wax (Sigma-Aldrich) so that the sample could be retained for months. Specific parameters of six samples and conditions for Raman spectroscopy are shown in .

6.3 Results and discussion

We show results for three sets of experiments. Each set includes semiconducting and metallic samples stabilized by the surfactant of: 1% DOC solution, variable concentration DOC solutions, and ssDNA, respectively.

6.3.1 DOC-SWCNT suspensions (1% DOC)

Sample 1: The Raman signal of semiconducting SWCNT suspensions in 1% DOC solutions is shown in Fig. 30. The R-P ratio increased with the increase of the laser power and then decreased with the increase of the laser power. The transition happened at different laser powers for SWCNT suspensions of different concentrations: a lower transition power for a more concentrated sample.

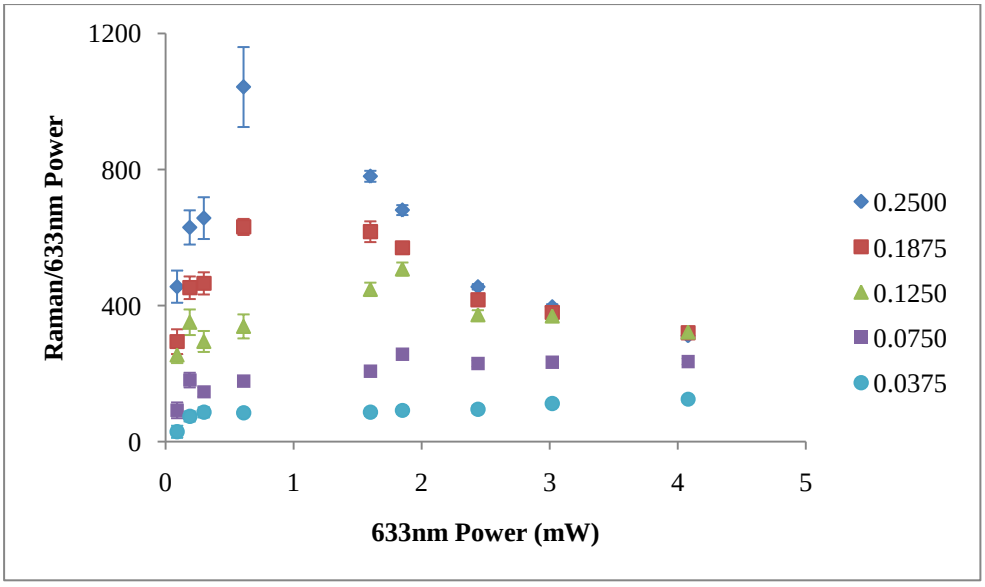

Fig. 30 The Raman signal of sample 1
The legend contains five concentrations of SWCNT suspensions in the unit of mg/ml.

Sample 2: The Raman signal of metallic SWCNT suspensions in 1% DOC solutions displayed a monotonic dependence on the laser power, as shown in Fig. 31. The R-P ratio increased with the increase of the laser power. The relative increase was different for SWCNT suspensions of different concentrations: a larger relative increase for a more concentrated sample. Specifically, little if any increase of the R-P ratio was observed in the most dilute (15%) sample, indicating no trapping. However, the relative increase of the particle number density within the trapping volume supposedly is higher for more dilute samples.[49]

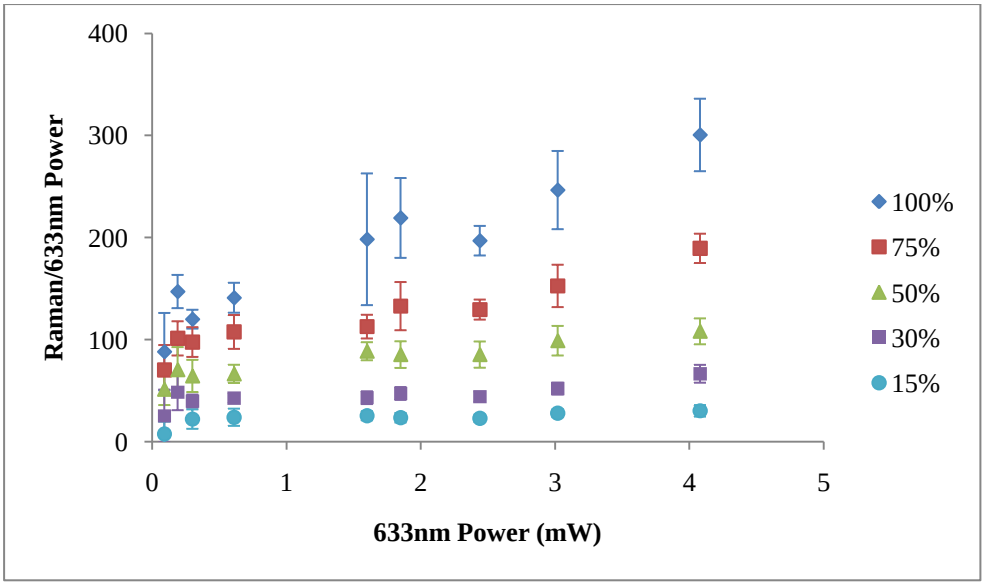

Fig. 31 The Raman signal of sample 2

The legend contains five concentrations of SWCNT suspensions.

6.3.2 DOC-SWCNT suspensions (variable DOC concentration)

To assess the roles of DOC micelles in the Raman signal of SWCNT suspensions in 1% DOC solutions, we perform Raman spectroscopy on SWCNT suspensions by maintaining the concentration of SWCNTs, and varying the concentration of DOC.

Sample 3: The Raman signal of semiconducting SWCNT suspensions (0.075 mg/ml) in variable concentrations of DOC solutions is shown in Fig. 32. The R-P ratio increased with the increase of the laser power and then decreased with the increase of the laser power. The significance of the transition was different for SWCNT suspensions of different DOC concentrations: a more noticeable transition for lower DOC concentration.

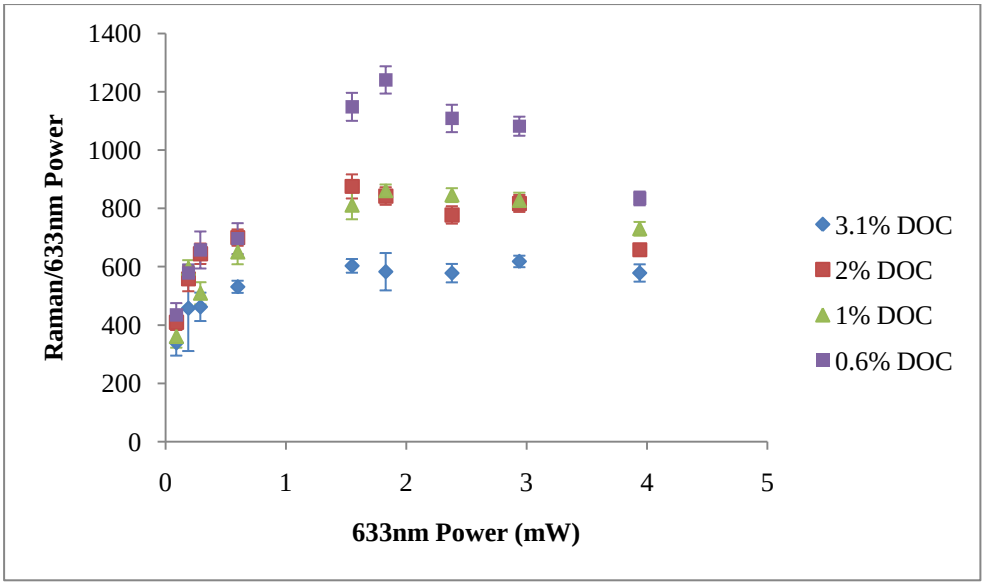

Fig. 32 The Raman signal of sample 3

The legend contains four DOC concentrations.

Sample 4: The Raman signal of metallic SWCNT suspensions (50%) in DOC solutions of variable concentrations displayed a monotonic dependence on the laser power, as shown in Fig. 33. The R-P ratio increased with the increase of the laser power. No significant difference was observed in SWCNT suspensions of different DOC concentrations.

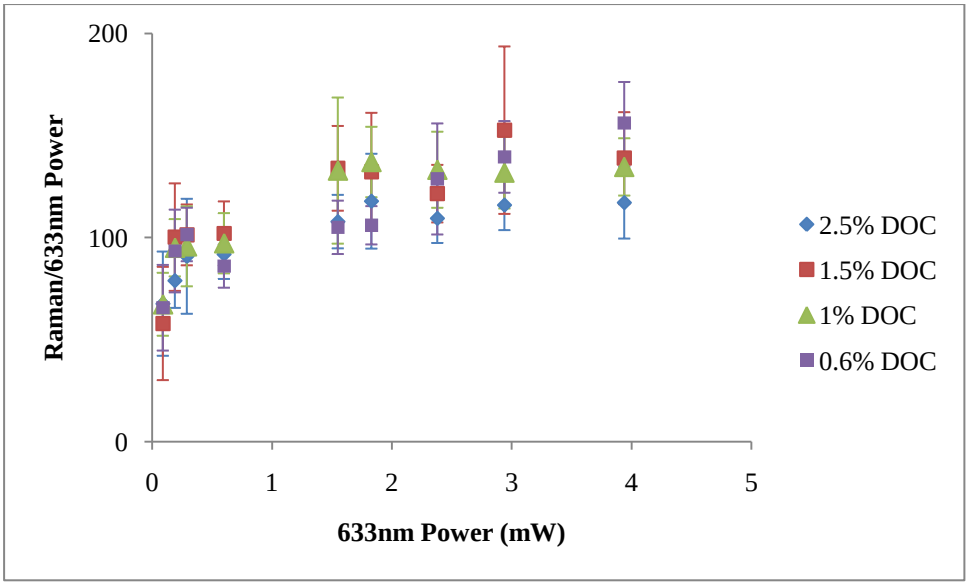

Fig. 33 The Raman signal of sample 4

The legend contains four DOC concentrations.

6.3.3 ssDNA-SWCNTs suspensions

To avoid effects due to DOC, we perform Raman spectroscopy on ssDNA-SWCNT suspensions.

Sample 5: The Raman signal of semiconducting ssDNA-SWCNT suspensions displayed a monotonic dependence on the excitation laser power, as shown in Fig. 34. The R-P ratio decreased with the increase of the laser power. The relative decrease was different for SWCNT suspensions of different concentrations: a larger relative decrease for a more concentrated sample, suggesting optical repelling (a negative potential well). However the relative decrease of the particle number density within the repelling volume is supposedly higher for more dilute samples.[49]

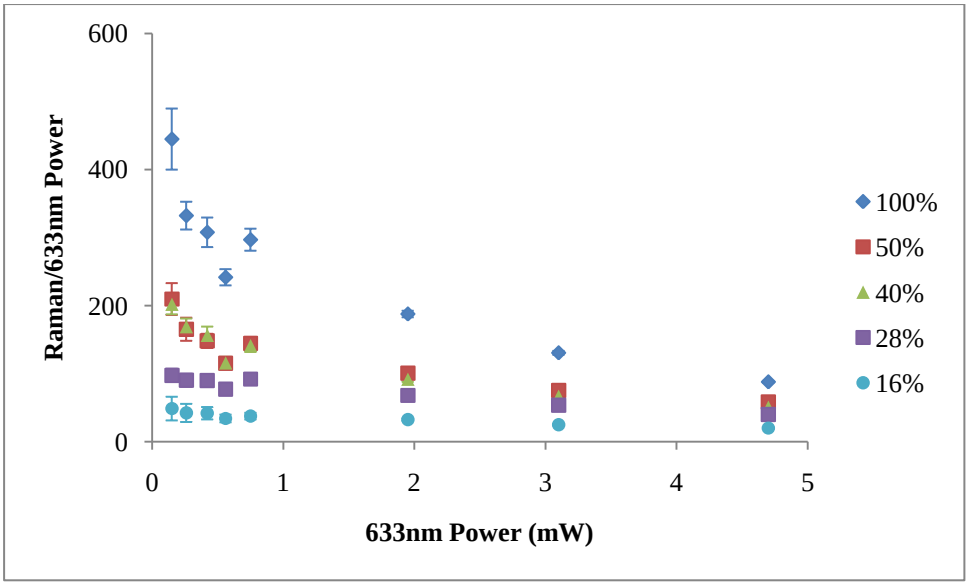

Fig. 34 The Raman signal of sample 5

The legend contains five concentrations of SWCNT suspensions.

Sample 6: The Raman signal of metallic ssDNA-SWCNT suspensions displayed a monotonic dependence on the excitation laser power, as shown in Fig. 35. The R-P ratio slightly decreased with the increase of the laser power.

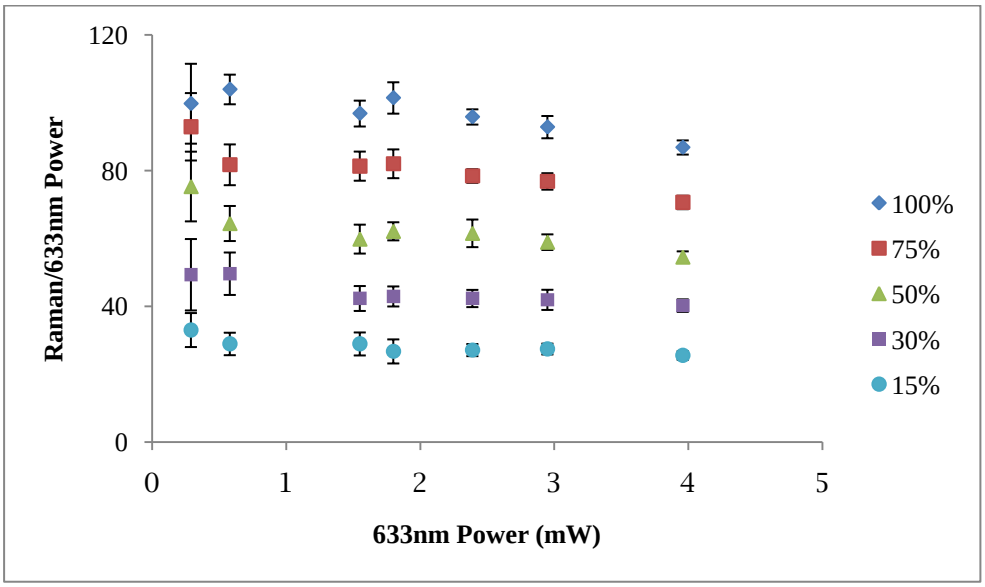

Fig. 35 The Raman signal of sample 6

The legend contains five concentrations of SWCNT suspensions.

6.3.4 Concentration and Orientation of SWCNTs

Based on the Raman signal of ssDNA-SWCNT suspensions, we proposed two interpretations for the R-P ratio as a function of the laser power. An naïve explanation is that both semiconducting and metallic SWCNTs were repelled by the focused 633 nm laser beam, as shown in Fig. 36 (a). In other words, the concentration of SWCNTs within the trapping volume, indicated by the R-P ratio, decreased with the increase of the laser power. On the other hand, one needs to consider the potential involvement of the orientation factor θ. While SWCNTs crowded towards the optical trap, they could however be aligned orthogonal to the laser beam polarization direction, as shown in Fig. 36 (b). That is, the population factor N increase negated by the orientation factor θ.

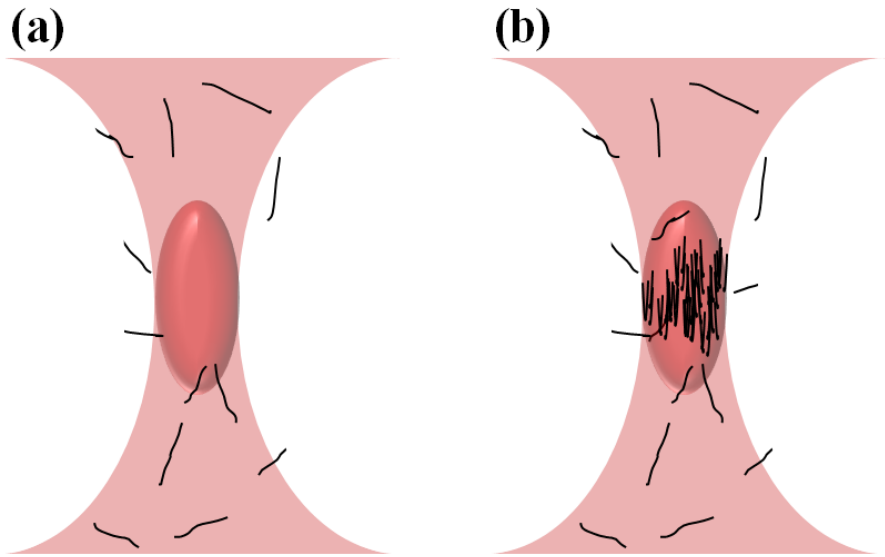

Fig. 36 Possible behavior of ssDNA-SWCNTs in optical tweezers

Two possible scenarios of how ssDNA-SWCNT suspensions respond to a focused 633 nm laser beam. SWCNTs are either (a) repelled by the beam, with the trapping volume (pink oval at the beam neck) evacuated; or (b) they crowd towards the trap and align along the direction of the beam propagation (orthogonal to the beam polarization).

6.4 Conclusions and outlook

By performing Raman spectroscopy on SWCNT suspensions, we inspected the Raman scattering intensity as a function of laser power. SsDNA proved to be a better agent than DOC in avoiding SWCNT aggregative, since the latter could affect the Raman signals of SWCNTs. While optical repelling was suggested by naively interpreting the Raman signal decrease with the increase of the laser power, two factors of tube concentration and orientation, however, were not distinguished by apply Raman spectroscopy alone. Fluorescence spectroscopy, as a direct indicator of the local number density of the SWCNTs, could potentially be coupled with Raman spectroscopy to “visualizing” the “optophoresis” of suspended SWCNTs in an optical field.

7. CONCLUSIONS AND OUTLOOK

Optical tweezers-based single particle force spectroscopy, coupled with phase sensitive detection was applied to isolate two commonly coexistent AC electrokinetic mechanisms of DEP and ACEO. By extracting the individual contribution of DEP and ACEO on a single probe particle, we explained the migration of the polarized electrical double layer associated with the particle. We verified the significance of the Schwarz model in the dielectrophoretic response of a single particle to a nonuniform electric field, by proving the diffusion-controlled motion of the double layer along the particle perimeter. We also completed an unambiguous mapping of the AC electroosmotic flow field by tracing the motion of different sized probe particles in the two dimensional space. We extended our studies to electrically polarized single-walled carbon nanotubes, by analyzing their migration and orientation at optical frequencies, with the assistance of combined Raman spectroscopy and fluorescence microscopy. Future research that may provide more perspective of the AC electrokinetics experienced by polarizable particles is discussed below.

7.1 DEP crossover frequency in electrolytes

7.1.1 Medium conductivity

The influence of a critical parameter of medium conductivity was not included in the examination of applying Schwarz model to explain the electrical double layer relaxation in DEP of a single particle. While medium conductivity isn't expressive in Eq. (24), hence not directly related to the counterion diffusion; it may significantly affect the condition of $r \gg \lambda_D$. For micron and submicron colloidal particles, the

Debye length is much smaller than the particle size in concentrated electrolytes (I > ~1 mM), where the Debye length is less than 50 nm. In our experiment, the Debye length (λ_D = ~200 nm, as calculated in Appendix C) was comparable to the radius of the smallest particle (r = 370 nm). Based on the measurements of the DEP crossover frequency, we conclude diffusion may not prevail in the dispersion of the double layer when the Debye length is close to the particle size. To further testify the conclusion, we may further investigate the dominance of the counterion diffusion as a function of medium conductivity by measuring the DEP crossover frequencies of colloidal particles suspended in liquid medium of different salt concentrations. Presumably, a better accordance of the dielectrophoretic response of colloidal particles with the Schwarz model will be seen in salty solutions.

7.1.2 Hofmeister series

The Hofmeister series[50,51] is referred to as a classification of ions in order of their ability to interact with water molecules and lower the solubility of proteins in aqueous solutions. Ions of the same valence may be slightly different in their ability to attract water molecules: K+ > Na+, Cl- > Br-. While the mechanism of the Hofmeister series is not entirely clear, it may be inteprated by studying the ion dispersion in DEP by measuring the DEP crossover frequencies in electrolytes containing different salts.

7.2 Mapping of the flow field of ACEO above the electrodes

The electrode chamber design prevented us from measuring the “driving force” of ACEO above the electrodes on a single probe particle trapped by optical tweezers. A direct examination of Eq. (3) given by the the Helmholtz-Smoluchowski equation,

as a consequence, was unavailable. By constructing a chamber with transparent ITO electrodes, optical tweezers-based force spectroscopy can be coupled to measure unambiguous ACEO flow above the electrodes. This will allow us to better examine the classical theory on ACEO in two ways: a comparison between the flow velocity measured outside the double layer and the calculated Helmholtz-Smoluchowski velocity, and a comparison between the flow field measured above the electrodes and the field simulated by COMSOL Multiphysics.

7.3 Optical trapping induced orientation of SWCNTs

Raman spectroscopy alone was not able to differentiate two factors of tube concentration and orientation in an optical field. Fluorescence spectroscopy, as a direct indicator of the local number density of the SWCNTs, may become an essential tool for understanding the "optophoresis" of suspended SWCNTs.

7.3.1 Optical setup

Shown in Fig. 37 is a schematic of confocal microscopy coupled with Raman and fluorescence spectroscopy. The confocal part of the microscope is used for fluorescence detection. The fluorescent excitation laser beam is sent through the bottom objective lens (100X, N.A. = 1.3) to excite the sample. The fluorescence will be collected with the same bottom lens through an adjustable pinhole with a default diameter of 205μm. An OD 6 notch filter is used to reject the 633nm trapping laser light, before the signal is detected by a photomultiplier.

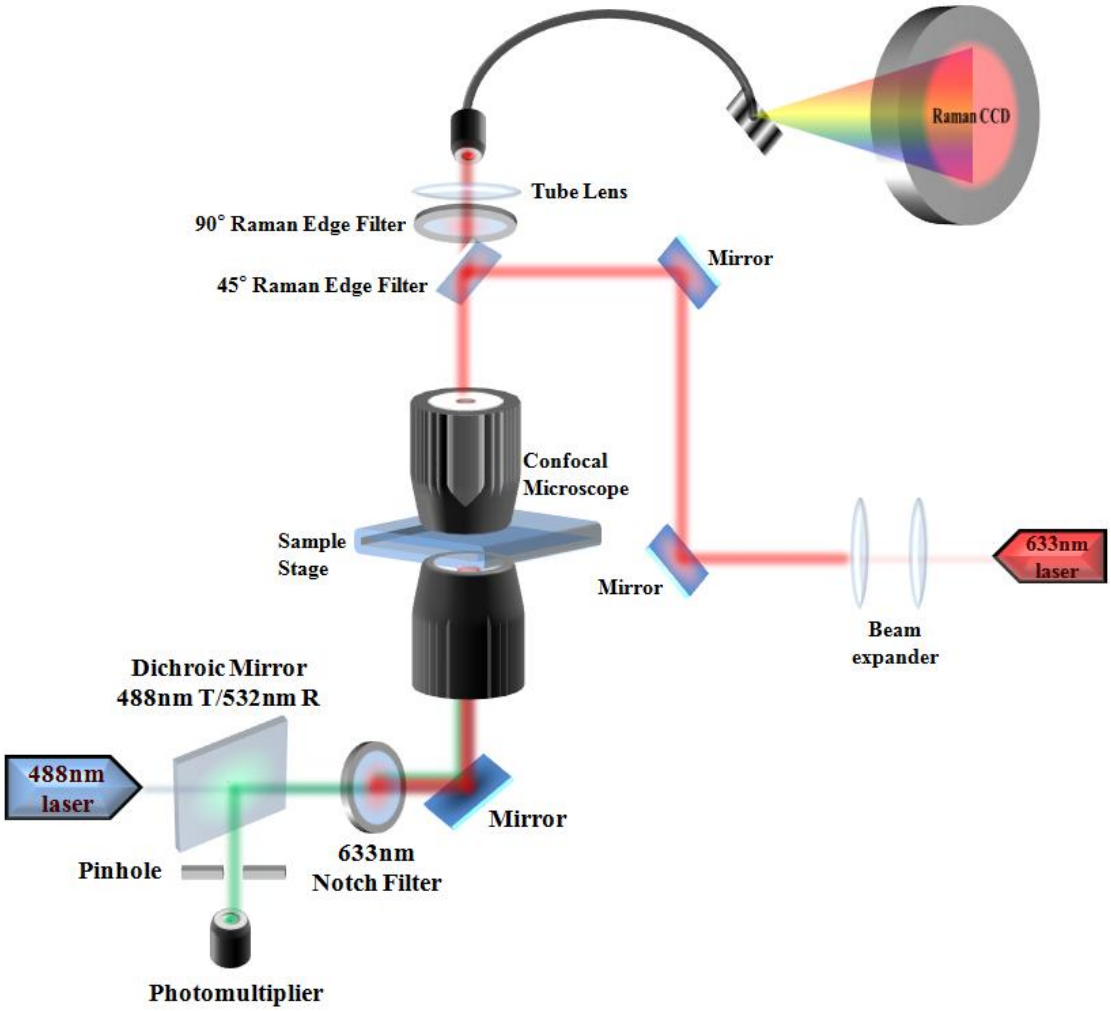

Fig. 37 Optical setup of Raman and fluorescence spectroscopy and confocal microscopy for quantifications of the SWCNT concentration and orientation.

7.3.2 Fluorescence Spectroscopy on ssDNA-SWCNT suspensions

SWCNTs don't naturally fluoresce. Therefore ssDNA labeled with fluoro-dye can be used tag SWCNTs. To increase the efficiency of labeling, Polymer "spacers" of several nm long can be used to connect the labeled ssDNA with the tubes, to diminish the quenching effects of SWCNTs. The fluoro-dye can be excited by a 488 nm laser beam, which is focused by the bottom objective and coupled with the 633 nm optical tweezers, as shown in Fig. 37. By scanning over the entire optical trapping

volume, we may probe the potential increase or decrease of the fluorescence intensity, as shown in Fig. 38 and Fig. 39.

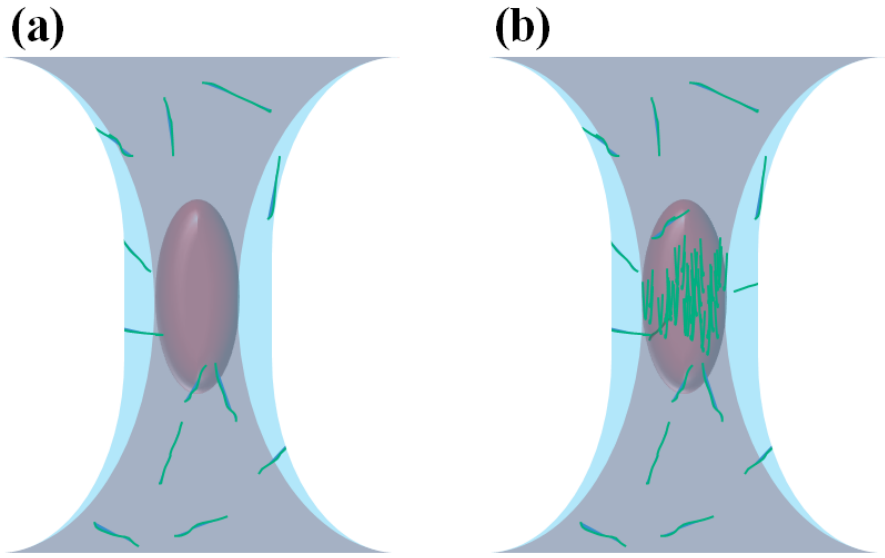

Fig. 38 Possible behavior of labeled ssDNA-SWCNTs in optical tweezers

Two possible scenarios of how labeled ssDNA-SWCNT suspensions respond to a focused 633 nm laser beam. Confocal microscopy with a 488 nm excitation laser beam was used to scan over the entire optical trapping volume, to detect spatial distribution of fluorescence.

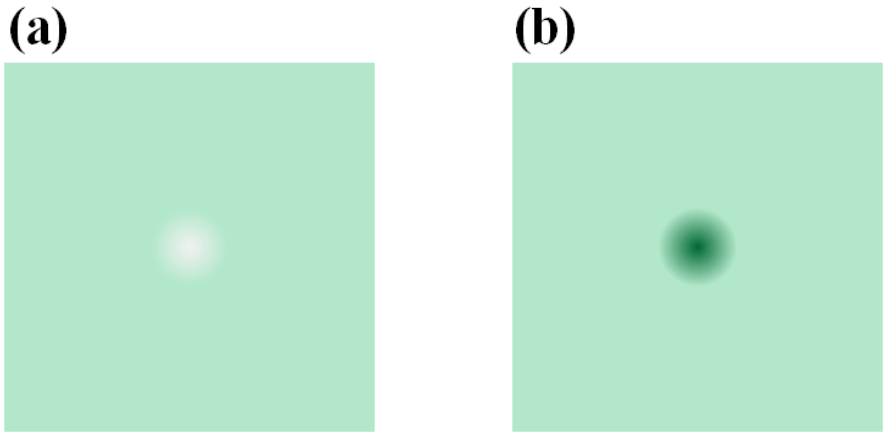

Fig. 39 Fluorescence spectrsocopy on labeled ssDNA-SWCNTs

Fluorescence scan inside and outside the optical trap. (a) Weaker fluorescence is detected within the trapping volume if the labeled ssDNA-SWCNTs are repelled by the beam; and (b) stronger fluorescence is detected within the trapping volume if the labeled ssDNA-SWCNTs are attracted by the beam.

APPENDICES

Appendix A

Estimation of the distance between neighboring particles

Both the water and the colloidal particle density are known:

$$\rho_{water} = 1 g/cm^3 \quad \text{and} \quad \rho_{particle} = 1.05 g/cm^3$$

We start with a particle suspension with 10% weight concentration:

$$10\% = \frac{W_{particle}}{W_{particle} + W_{water}} = \frac{V_{particle} \cdot \rho_{particle}}{V_{particle} \cdot \rho_{particle} + V_{water} \cdot \rho_{water}}$$

$$10\% = \frac{V_{particle} \cdot 1.05 g/cm^3}{V_{particle} \cdot 1.05 g/cm^3 + V_{water} \cdot 1 g/cm^3}$$

This gives the water/particle ratio and hence the suspension/particle ratio in volume:

$$V_{water} = 9.45 V_{particle} \quad \text{and} \quad V_{suspension} = V_{water} + V_{particle} = 10.45 V_{particle}$$

By using an example of 750nm particles, we write the total volume of particles as:

$$V_{particle} = N_{particle} \cdot \frac{4}{3}\pi(750nm)^3$$

We derive the particle number density:

$$\frac{N_{particle}}{V_{suspension}} = \frac{V_{particle}}{\frac{4}{3}\pi(750nm)^3 \cdot 10.45 V_{particle}} \cong 8.5 \cdot 10^8 / cm^3$$

Therefore the particle number density of a colloidal suspension that is diluted by volume from the original sample a factor of 10^4 times is:

$$\frac{N_{particle}}{V_{solution}} = 8.5 \cdot 10^4 / cm^3$$

From this we obtain the average distance between two neighboring particles:

$$d_{particle-particle} = \left(\frac{V_{solution}}{N_{particle}} \right)^{1/3} = \left(\frac{cm^3}{8.5 \cdot 10^4} \right)^{1/3} \cong \boxed{228\mu m}$$

Since 228μm is much larger than the Debye length of several hundred nanometers' thick, the particle-particle electrostatic interaction can be ignored.

Appendix B

Standard photolithography

A typical photolithography process includes steps of substrate cleaning, spin coating, pre-baking, exposure, stripping, etching, post-baking and development, as shown in Fig. 40. First, the glass substrate is prepared for later photoresist applications by surface cleaning and/or dehydration baking. A high quality two-layer film, a 200nm-thick gold film on top of a 10nm-thick titanium film, is grown on top of the glass substrate by chemical vapor deposition. Titanium is used as an adherent to help hold the gold film, thus the gold doesn't easily peel off from the glass substrate. Negative photoresist SU-8 is spin coated on the top of the gold layer. The glass slide is pre-baked so that the solvent in the photoresist evaporates; thus enhancing the attachment of the photoresist to the gold layer. Pre-bake typically lasts 10~30 min at 90~100 ℃. A mask with desired patterns is aligned to the glass slide, when the negative photoresist (containing a crosslinker, which will be activated during exposure) is exposed to a UV light source. The developer solution is applied by either spray or immersion while the unexposed area of the photoresist dissolves in the developer. The slide is again baked, typically for 10~30min at 100~140 ℃ in order that the remaining developer evaporates. A dry/wet etch is applied to the slide to achieve the desired pattern of the Ti/Au layer by removing the bare areas of Ti/Au. They are revealed after the photoresist is stripped off.

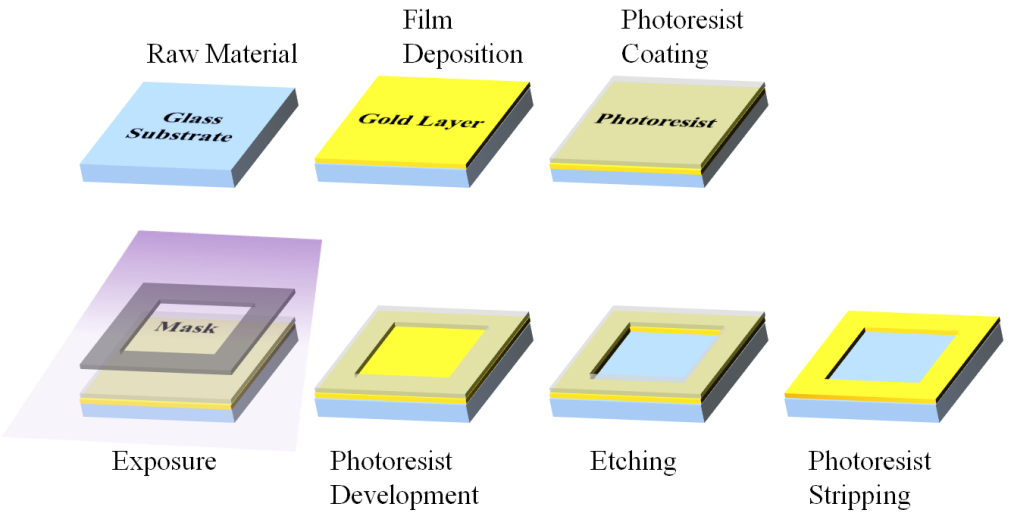

Fig. 40 A standard process of photolithography

Appendix C

Estimation of λ_D

We evaluate the Debye length to examine the validity of the condition $a \gg \lambda_D$. We assume our medium to be DI water in equilibrium with atmospheric CO_2.

Henry's law states: At a constant temperature, the amount of a given gas that dissolves in a given type and volume of liquid is proportional to the partial pressure of that gas in equilibrium with that liquid. Its mathematical form is:

$$p = k_H \cdot [gas]$$

where p is the partial pressure of the gas above the solution, [gas] is the molar concentration of the gas dissolved in the liquid, and k_H is a constant that depends on the gas, the liquid and the temperature, and known as Henry's law constant.

$k_H(CO_2)$ = 29.4 L·atm/mole in water at 25 ℃. The partial pressure of CO_2 is 391 ppm = $3.91 \cdot 10^{-4}$ atm. We apply Henry's Law to derive the molar concentration of CO_2 dissolved in water:

$$p_{CO_2} = 3.91 \cdot 10^{-4}\,\text{atm} = k_H \cdot [CO_2] = 29.4\,\text{L} \cdot \text{atm/mol} \cdot [CO_2]$$

$$[CO_2] = \frac{3.91 \cdot 10^{-4}\,\text{atm}}{29.4\,\text{L} \cdot \text{atm/mol}} = 1.33 \cdot 10^{-5}\,\text{mol/L}$$

The reaction in water is:

$$CO_2 + H_2O \rightleftarrows H_2CO_3 \rightleftarrows H^+ + HCO_3^-$$

meaning CO_2 exists in water in both forms of gas and carbonic acid.

The equilibrium constant for the acid dissociation is:

$$K_{a1} = \frac{[H^+][HCO_3^-]}{[H_2CO_3 + CO_2(\text{liquid})]} = 4.46 \cdot 10^{-7}\,\text{mol/L}$$

where $[H_2CO_3 + CO_2(\text{liquid})] = [CO_2] = 1.33 \cdot 10^{-5}\,\text{mol} / \text{L}$.

From above we get an equation containing two variables that we need to solve for:

$$[H^+][HCO_3^-] = 4.46 \cdot 10^{-7}\,\text{mol} / \text{L} \cdot 1.33 \cdot 10^{-5}\,\text{mol} / \text{L} = 5.93 \cdot 10^{-12}\,\text{mol}^2 / \text{L}^2$$

Two more equations are necessary to solve the relation between $[H^+]$ and $[HCO_3^-]$.

The dissociation constant of water into components of H^+ and HCO_3^- is (at 25 ℃)

$$K_w = [H^+][OH^-] = 1.2 \cdot 10^{-14}\,\text{mol}^2 / \text{L}^2,$$

as the second equation.

And the global neutrality of charge gives

$$[H^+] = [OH^-] + [HCO_3^-],$$

as the third equation.

We rewrite the three equations to solve three unknown quantities $[H^+]$, $[OH^-]$ and $[HCO_3^-]$.

$$[H^+][HCO_3^-] = 5.93 \cdot 10^{-12}\,\text{mol}^2 / \text{L}^2$$

$$K_w = [H^+][OH^-] = 1.2 \cdot 10^{-14}\,\text{mol}^2 / \text{L}^2$$

$$[H^+] = [OH^-] + [HCO_3^-]$$

The solutions are:

$$[H^+] = 2.44 \cdot 10^{-6}\,\text{mol} / \text{L}$$

$$[OH^-] = 4.92 \cdot 10^{-9}\,\text{mol} / \text{L}$$

$$[HCO_3^-] = 2.42 \cdot 10^{-6}\,\text{mol} / \text{L}$$

From here we notice the molar concentration of $[OH^-]$ can be neglected.

We calculate the pH value of the solution as:

$$pH = -\log[H^+] = 5.6$$

An agreement with the value found using the pH test paper was shown.

We calculate the ionic strength of the solution by considering all the ions present:

$$I = \frac{1}{2}\sum_{i=1}^{n}[gas_i]z_i^{\ 2} = \frac{1}{2}\{[H^+]\cdot 1^2 + [OH^-]\cdot(-1)^2 + [HCO_3^{\ -}]\cdot(-1)^2\}$$

$$= \frac{1}{2}\{2.44\cdot 10^{-6}\,mol/L + 4.92\cdot 10^{-9}\,mol/L + 2.42\cdot 10^{-6}\,mole/L\} = 2.44\cdot 10^{-6}\,mol/L$$

Therefore, the Debye length is calculated as:

$$\lambda_D = 0.304/\sqrt{I} = 194.6nm \cong 200nm$$

We verify the above evaluations by comparing the result to the experimental value of medium conductivity. Here we use the following equivalent conductivities L at infinite dilution (also called limiting molar conductivities):

$$L_{[H^+]} = 349.7S/cm$$

$$L_{[OH^-]} = 198S/cm$$

$$L_{[HCO_3^{\ -}]} = 44.5S/cm$$

The medium conductivity is calculated to be:

$$\begin{aligned}\sigma &= L_{[H^+]}\cdot[H^+] + L_{[OH^-]}\cdot[OH^-] + L_{[HCO_3^{\ -}]}\cdot[HCO_3^{\ -}]\\ &= 349.7S/cm\cdot 2.44\cdot 10^{-9}\,mol/L\\ &+198S/cm\cdot 4.92\cdot 10^{-12}\,mol/L\\ &+44.5S/cm\cdot 2.42\cdot 10^{-9}\,mol/L\\ &= 0.96\mu S/cm\end{aligned}$$

The value falls in the experimental range of 0.8~2.1 μS/cm.

From the above calculations, we conclude $r \gg \lambda_D$ was a crude approximation in our experiments, where the particle radius fell in the range of 370~1450 nm.

Appendix D

Estimates of DEP crossover frequency ω_{DEP}

By plugging Eq. (27) and (28) into Eq. (29)

$$\omega_{DEP} = \frac{1}{2\pi}\sqrt{\frac{(\frac{\omega^2\tau_\alpha}{1+\omega^2\tau_\alpha{}^2}\frac{e^2 r\sigma_0}{k_B T} - \sigma_m)(\frac{\omega^2\tau_\alpha}{1+\omega^2\tau_\alpha{}^2}\frac{e^2 r\sigma_0}{k_B T} + 2\sigma_m)}{(\varepsilon_m - \frac{1}{1+\omega^2\tau_\alpha{}^2}\frac{e^2 r\sigma_0}{k_B T})(\frac{1}{1+\omega^2\tau_\alpha{}^2}\frac{e^2 r\sigma_0}{k_B T} + 2\varepsilon_m)}},$$

where $\varepsilon_m = 78\varepsilon_0$ and $\sigma_m \cong 2\mu S/cm$.

For convenience, we divide both the numerator and denominator in the square root by ε_0.

$$\omega_{DEP} = \frac{1}{2\pi}\sqrt{\frac{(\frac{\omega^2\tau_\alpha}{1+\omega^2\tau_\alpha{}^2}\frac{e^2 r\sigma_0}{\varepsilon_0 k_B T} - \frac{\sigma_m}{\varepsilon_0})(\frac{\omega^2\tau_\alpha}{1+\omega^2\tau_\alpha{}^2}\frac{e^2 r\sigma_0}{\varepsilon_0 k_B T} + 2\frac{\sigma_m}{\varepsilon_0})}{(\frac{\varepsilon_m}{\varepsilon_0} - \frac{1}{1+\omega^2\tau_\alpha{}^2}\frac{e^2 r\sigma_0}{\varepsilon_0 k_B T})(\frac{1}{1+\omega^2\tau_\alpha{}^2}\frac{e^2 r\sigma_0}{\varepsilon_0 k_B T} + 2\frac{\varepsilon_m}{\varepsilon_0})}}$$

We define $x = \frac{e^2\sigma_0 r}{\varepsilon_0 k_B T}$, the DEP crossover frequency is rewritten as

$$\omega_{DEP} = \frac{1}{2\pi}\sqrt{\frac{(\frac{\omega^2\tau_\alpha}{1+\omega^2\tau_\alpha{}^2}x - \frac{\sigma_m}{\varepsilon_0})(\frac{\omega^2\tau_\alpha}{1+\omega^2\tau_\alpha{}^2}x + 2\frac{\sigma_m}{\varepsilon_0})}{(78 - \frac{1}{1+\omega^2\tau_\alpha{}^2}x)(\frac{1}{1+\omega^2\tau_\alpha{}^2}x + 156)}}$$

We evaluate the quantities in the equation for 750 nm particle at 27°: (for convenience we omit all the SI untis)

According to Eq. (23), $\tau_\alpha = \frac{r^2}{2D} = \frac{(750\cdot 10^{-9})^2}{2\cdot 9.31\cdot 10^{-9}} = 3\cdot 10^{-5}$

The frequency range for a 750 nm particle is ~50 kHz,

$\omega^2\tau_\alpha{}^2 = (3\cdot 10^{-5})^2(100\cdot 10^3\pi)^2 = 89$ and is much bigger than 1.

Therefore, $\frac{\omega^2\tau_\alpha}{1+\omega^2{\tau_\alpha}^2} \cong \frac{\omega^2\tau_\alpha}{\omega^2{\tau_\alpha}^2} = \frac{1}{\tau_\alpha}$

Assuming a typical surface charge value $\sigma_0 = 10^{16}/\mathrm{m}^2$,

$$x = \frac{e^2\sigma_0 r}{\varepsilon_0 k_B T} = \frac{(1.6\cdot10^{-19})^2\cdot10^{16}\cdot750\cdot10^{-9}}{8.854\cdot10^{-12}\cdot1.38\cdot10^{-23}\cdot300} = 5238$$

$\frac{\omega^2\tau_\alpha}{1+\omega^2{\tau_\alpha}^2} x \cong \frac{x}{\tau_\alpha} = (3\cdot10^{-5})^{-1}\cdot5238 = 1.7\cdot10^8$ and $\frac{\sigma_m}{\varepsilon_0} = \frac{2\cdot10^{-4}}{8.854\cdot10^{-12}} = 2.2\cdot10^7$

Therefore, $\frac{\omega^2\tau_\alpha}{1+\omega^2{\tau_\alpha}^2} x \gg \frac{\sigma_m}{\varepsilon_0}$

$$(\frac{\omega^2\tau_\alpha}{1+\omega^2{\tau_\alpha}^2} x - \frac{\sigma_m}{\varepsilon_0})(\frac{\omega^2\tau_\alpha}{1+\omega^2{\tau_\alpha}^2} x + 2\frac{\sigma_m}{\varepsilon_0}) \cong (\frac{\omega^2\tau_\alpha}{1+\omega^2{\tau_\alpha}^2} x)^2 \cong \frac{x^2}{{\tau_\alpha}^2} = x^2{\omega_\alpha}^2$$

$\frac{1}{1+\omega^2{\tau_\alpha}^2} x \cong \frac{x}{\omega^2{\tau_\alpha}^2} = \frac{5238}{(2\pi\cdot50\cdot10^3\cdot3\cdot10^{-5})^2} = 59$ is comparable to 78 and 156.

Therefore, we keep all the terms in the denominator and try solving

$$\omega = \frac{1}{2\pi}\sqrt{\frac{x^2{\omega_\alpha}^2}{(78-\frac{x{\omega_\alpha}^2}{\omega^2})(156+\frac{x{\omega_\alpha}^2}{\omega^2})}}\,.$$

The solution is $\omega = \omega_{DEP}$.

$$\omega^2 = \frac{1}{4\pi^2}\frac{x^2{\omega_\alpha}^2}{(78-\frac{x{\omega_\alpha}^2}{\omega^2})(156+\frac{x{\omega_\alpha}^2}{\omega^2})}$$

$$4\pi^2\omega^2(78-\frac{x{\omega_\alpha}^2}{\omega^2})(156+\frac{x{\omega_\alpha}^2}{\omega^2}) = x^2{\omega_\alpha}^2$$

$$4\pi^2\omega^2[78(156+\frac{x{\omega_\alpha}^2}{\omega^2}) - \frac{x{\omega_\alpha}^2}{\omega^2}(156+\frac{x{\omega_\alpha}^2}{\omega^2})] = x^2{\omega_\alpha}^2$$

$$4\pi^2\omega^2[12168+78\frac{x{\omega_\alpha}^2}{\omega^2} - 156\frac{x{\omega_\alpha}^2}{\omega^2} - \frac{x^2{\omega_\alpha}^4}{\omega^4}] = x^2{\omega_\alpha}^2$$

$$4\pi^2\omega^2[12168-78\frac{x\omega_\alpha{}^2}{\omega^2}-\frac{x^2\omega_\alpha{}^4}{\omega^4}]=x^2\omega_\alpha{}^2$$

$$48672\pi^2\omega^2-312\pi^2x\omega_\alpha{}^2-\frac{4\pi^2x^2\omega_\alpha{}^4}{\omega^2}=x^2\omega_\alpha{}^2$$

$$48672\pi^2\omega^4-(312\pi^2x\omega_\alpha{}^2+x^2\omega_\alpha{}^2)\omega^2-4\pi^2x^2\omega_\alpha{}^4=0$$

The general solution of the polynomial equation is:

$$\omega^2=\frac{312\pi^2x\omega_\alpha{}^2+x^2\omega_\alpha{}^2\pm\sqrt{(312\pi^2x\omega_\alpha{}^2+x^2\omega_\alpha{}^2)^2+4\cdot48672\pi^2\cdot4\pi^2x^2\omega_\alpha{}^4}}{2\cdot48672\pi^2}$$

$$\omega^2=\frac{312\pi^2x\omega_\alpha{}^2+x^2\omega_\alpha{}^2\pm\sqrt{97344\pi^4x^2\omega_\alpha{}^4+x^4\omega_\alpha{}^4+624\pi^2x^3\omega_\alpha{}^4+778752\pi^4x^2\omega_\alpha{}^4}}{97344\pi^2}$$

Therefore, $\omega^2=\frac{312\pi^2x\omega_\alpha{}^2+x^2\omega_\alpha{}^2\pm\sqrt{876096\pi^4x^2\omega_\alpha{}^4+x^4\omega_\alpha{}^4+624\pi^2x^3\omega_\alpha{}^4}}{97344\pi^2}$

Rewrite the equation as a function of r by defining:

$x=\frac{e^2\sigma_0}{\varepsilon_0k_BT}r=\frac{(1.6\cdot10^{-19})^2\cdot10^{16}}{8.854\cdot10^{-12}\cdot1.38\cdot10^{-23}\cdot300}r=7\cdot10^9r=ar$, where $a=7\cdot10^9$.

$\omega_\alpha=\frac{2D}{r^2}=2\cdot9.31\cdot10^{-9}r^{-2}=1.8\cdot10^{-8}r^{-2}=br^{-2}$, where $b=1.8\cdot10^{-8}$.

$x\omega_\alpha=7\cdot10^9r\cdot1.8\cdot10^{-8}r^{-2}=126r^{-1}=cr^{-1}$, where c = 126.

$$\omega^2=\frac{312\pi^2bcr^{-3}+c^2r^{-2}\pm\sqrt{876096\pi^4b^2c^2r^{-6}+c^4r^{-4}+624\pi^2bc^3r^{-5}}}{97344\pi^2}$$

Then we evaluate the terms in the square root in the numerator:

$876096\pi^4b^2c^2r^{-6}=876096\pi^4\cdot(1.8\cdot10^{-8})^2\cdot126^2\cdot(750\cdot10^{-9})^{-6}=2.5\cdot10^{33}$

$c^4r^{-4}=126^4\cdot(750\cdot10^{-9})^{-4}=8\cdot10^{32}$

$624\pi^2bc^3r^{-5}=624\pi^2\cdot1.8\cdot10^{-8}\cdot126^3\cdot(750\cdot10^{-9})^{-5}=9.3\cdot10^{32}$

Therefore, $876096\pi^4b^2c^2r^{-6}>624\pi^2bc^3r^{-5}>c^4r^{-4}$

We evaluate the terms out of the square root:

$$312\pi^2 bcr^{-3} = 312\pi^2 \cdot 1.8\cdot 10^{-8} \cdot 126 \cdot (750\cdot 10^{-9})^{-3} = 1.7\cdot 10^{16}$$

$$c^2 r^{-2} = 126^2 \cdot (750\cdot 10^{-9})^{-2} = 2.8\cdot 10^{16}$$

Therefore, $c^2 r^{-2} > 312\pi^2 bcr^{-3}$

From this, the dominant dependence of the angular DEP crossover frequency on r is,

$$\omega^2 \sim \frac{\sqrt{876096\pi^4 b^2 c^2 r^{-6}}}{97344\pi^2} = \frac{936}{97344} bcr^{-3} \quad \text{and hence}$$

$$\omega \sim \sqrt{bc} r^{-1.5} = \sqrt{2D\cdot 2D\cdot \frac{e^2\sigma_0}{\varepsilon_0 k_B T}} r^{-1.5} = 2e\sqrt{\frac{\sigma_0}{\varepsilon_0 k_B}} \frac{D}{\sqrt{T}} r^{-1.5}$$

$$\omega_{DEP} \sim \frac{D}{\sqrt{T}} r^{-1.5} \qquad (1)$$

Alternatively, we can express the dominant dependence of the angular DEP crossover frequency on the angular frequency of α-relaxation as

$$\omega_{DEP} = \sqrt{\frac{936}{97344}} \sqrt{\frac{e^2\sigma r}{\varepsilon_0 k_B T}} \omega_\alpha \qquad (2)$$

We calculate the theoretical value for the angular DEP crossover frequency

$$\omega^2 \cong \frac{1.7\cdot 10^{16} + 2.8\cdot 10^{16} + \sqrt{2.5\cdot 10^{33} + 8\cdot 10^{32} + 9.3\cdot 10^{32}}}{97344\pi^2} = 1.1\cdot 10^{11}$$

$f_{DEP} = \frac{\omega_{DEP}}{2\pi} = \frac{\sqrt{1.1\cdot 10^{11}}}{2\pi} = 53863 \cong 54\text{kHz}$, which is close to the measured value of 63 ± 5 kHz.

For r = 500 nm, $f_{DEP} \cong 92\text{kHz}$, which is close to the measured value of 108 ± 5 kHz.

Appendix E

High frequency limit of the Schwarz Model

A high frequency dispersion of the electrical double layer, β-relaxation,[32,52] has also been assigned to explain previous dielectrophoretic measurements of colloidal particles in different regimes of particle radius and medium conductivity. β-relaxation occurs when the frequency is sufficiently high when diffusion is no more a prevailing process of the counterion movement. It considers the migration of a symmetrically distributed double layer as a surface current tangential to the perimeter of the particle. (This is true under the premise of $a \gg \lambda_D$.) The particle suspension is therefore considered a series RC circuit. β-relaxation time, hence the charging/discharging time constant of the RC circuit, is determined by the combined dielectric properties of the medium and the particle,

$$\tau_\beta = \frac{\varepsilon_0(\varepsilon_p + 2\varepsilon_m)}{\sigma_p + 2\sigma_m} \tag{3}$$

where ε_0 is the vacuum permittivity, ε_m is the relative permittivity and σ is the conductivity. The subscript p and m denote particle and medium, respectively. The total particle conductivity σ_p is a combination of the native particle conductivity σ_0 and the conductivity of the double layer K_{DL}.

$$\sigma_p = \sigma_0 + \frac{K_{DL}}{r} \tag{4}$$

where σ_0 is usually negligible for dielectric particles. The surface conductance contributed by the double layer is however considerable. For highly deionized (DI) water of a resistivity of 18.3 MΩ/cm, $(K_S+K_D)/r \gg \sigma_m$. For low conductivity solutions, such as those used in our experiments, $(K_S+K_D)/r$ and σ_m can be comparable in

magnitude. According to O'Konski,[53] K_S+K_D is proportional to the counterion mobility u within the double layer, $K_S+K_D = e(s_+u_+z_+ + s_-u_-z_-)$, where e is the elementary charge, s is the counterion number density and z is the absolute value of the valence. The subscript + and – denote cations and anions，respectively, if only two types of ions exist in the solution. We can rewrite the surface conductance as

$$K_S + K_D = \frac{e^2}{6\pi\eta}\left(\frac{s_+z_+}{a_+} + \frac{s_-z_-}{a_-}\right) \tag{5}$$

where a is the counterion radius and η is viscosity. From Eq. (3), (4) and (5), the frequency of β-relaxation is

$$f_{C,\beta} = \frac{1}{2\pi\tau_\beta} \cong \frac{1}{2\pi\varepsilon_0(\varepsilon_p + 2\varepsilon_m)}\left[\frac{e^2}{6\pi\eta r}\left(\frac{s_+z_+}{a_+} + \frac{s_-z_-}{a_-}\right) + 2\sigma_m\right] \tag{6}$$

For a highly conductive medium when $(K_S+K_D)/r \ll \sigma_m$, the first term in the bracket falls out. Therefore the β-relaxation frequency has no dependence on the particle radius. For extremely low conductivity solutions, $(K_S+K_D)/r \gg \sigma_m$, the β-relaxation frequency is approximated as

$$f_{C,\beta} \cong \frac{e^2}{12\pi^2\varepsilon_0(\varepsilon_p + 2\varepsilon_m)}\left(\frac{s_+z_+}{a_+} + \frac{s_-z_-}{a_-}\right)\frac{1}{\eta r}, \tag{7}$$

showing an inverse proportional relation with particle radius and medium viscosity; and is independent of temperature. From the DEP crossover frequencies found in the three controlled experiments by varying the parameters of particle size, the medium viscosity and temperature, we believe the double layer relaxation in DEP isn't attributed by β-relaxation.

Appendix F

The numerical approach of Eq. (31)

The distribution of v_x measured within the gap area is expressed in a generalized form as shown in Table 2. The subscripts (1, 2, …, n-1, n) and (1, 2, …, j-1, j) are integers, and indicate the order of the coordinates in the x and z directions, respectively. Specifically, x_1 is the closest to the electrode tip and x_n is the closest to the mid axis; z_1 is the closest to the glass substrate and z_n is the farthest from the glass substrate.

	x_n	x_{n-1}	…	x_2	x_1
z_j	$V_{x\|n,j}$	$V_{x\|n-1,j}$		$V_{x\|2,j}$	$V_{x\|1,j}$
z_{j-1}	$V_{x\|n,j-1}$	$V_{x\|n-1,j-1}$		$V_{x\|2,j-1}$	$V_{x\|1,j-1}$
…					
z_2	$V_{x\|n,2}$	$V_{x\|n-1,2}$		$V_{x\|2,2}$	$V_{x\|1,2}$
z_1	$V_{x\|n,1}$	$V_{x\|n-1,1}$		$V_{x\|2,1}$	$V_{x\|1,1}$

Table 2 X-components of the ACEO flow velocity at different locations (x_n, z_j)

By taking first order/linear approximation, we define:

$$v_{x|n-0.5,j} = (v_{x|n,j} + v_{x|n-1,j})/2$$

as the x-component of the flow velocity at the location of ($x_{n-0.5}$, z_j), where $x_{n-0.5} = (x_n + x_{n-1})/2$.

Table 2 is thus expanded to Table 3.

	x_n	$x_{n-0.5}$	x_{n-1}	...	x_2	$x_{1.5}$	x_1
z_j	$v_{x\|n,j}$	$v_{x-0.5\|n,j}$	$v_{x\|n-1,j}$		$v_{x\|2,j}$	$v_{x\|1.5,j}$	$v_{x\|1,j}$
z_{j-1}	$v_{x\|n,j-1}$	$v_{x-0.5\|n,j-1}$	$v_{x\|n-1,j-1}$		$v_{x\|2,j-1}$	$v_{x\|1.5,j-1}$	$v_{\|1,j-1}$
...							
z_2	$v_{x\|n,}$	$v_{x-0.5\|n,2}$	$v_{x\|n-1,2}$		$v_{x\|2,2}$	$v_{x\|1.5,2}$	$v_{x\|1,2}$
z_1	$v_{x\|n,1}$	$v_{x-0.5\|n,1}$	$v_{x\|n-1,1}$		$v_{x\|2,1}$	$v_{x\|1.5,1}$	$v_{x\|1,1}$

Table 3 Linear extension of Table 2 along the x axis

Then we apply Eq. (31) and derive the z-component of the flow velocity as:

$$v_{z|n-0.5,j+0.5} = -(v_{x|n,j} - v_{x|n-1,j}) \cdot (z_{j+0.5} - z_{j-0.5}) / (x_n - x_{n-1}) + v_{z|n-0.5,j-0.5}$$

By approximating $z_{j+0.5} - z_{j-0.5} \cong x_n - x_{n-1}$, the z-component of the flow velocity at (n - 0.5, j + 0.5) is:

$$v_{z|n-0.5,j+0.5} \cong v_{x|n-1,j} - v_{x|n,j} + v_{z|n-0.5,j-0.5}$$

This can be illustrated by a sketch of the flux continuity equation, as shown in Fig. 41.

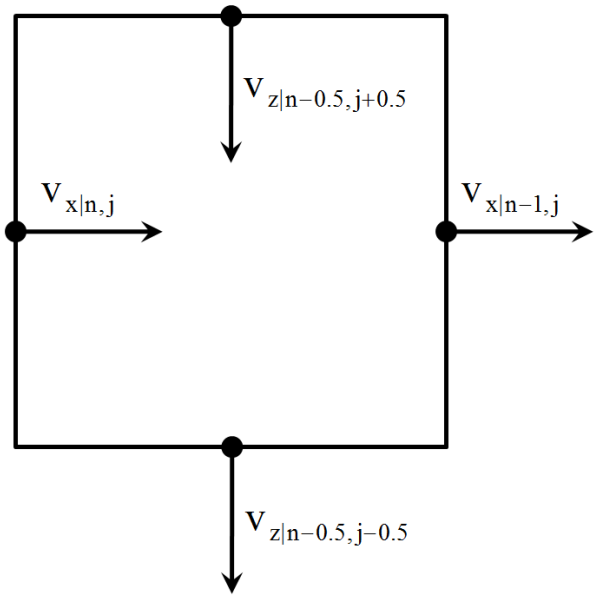

Fig. 41 Fluid flux continuity

Fluid flux passing through a close surface. The amount of the fluid is conserved, therefore the amount of the fluid that passes inside the region equals the amount that passes outside.

The magnitude of the velocity at ($x_{n-0.5}$, $z_{j+0.5}$) is therefore:

$$v_{n-0.5,j} = \sqrt{v_{x|n-0.5,j}^{2} + v_{z|n-0.5,j}^{2}}$$

Appendix G

COMSOL simulation of the electric field

In order to better understand the electrokinetics of AC electroosmosis and hence effectively guide future designs of ACEO-based microfluidic devices, one can resort to simulations to obtain the distribution of the electric field and thereafter calculate the corresponding ACEO. COMSOL Multiphysics, a commercial simulation software based on the finite element method, is commonly adopted to serve the purpose.

The routine steps of COMSOL modeling include: (1) choice of modes/platforms, (2) quantification of parameters/constants, (3) construction of geometrical designs, (4) definition of boundary conditions, (5) specification of subdomains (regarding their physical properties), and (6) meshing and solving. The physical model is mainly characterized by how the geometrical structure is designed and how the boundary conditions. Therefore, among the listed steps, (3) and (4) could be especially significant for the final simulation solutions. For this reason, we will discuss these two steps in detail and cover the others briefly in deriving the Helmholtz-Smoluchowski velocity in ACEO, expressed as Eq. (5).

(1) Choice of Modes/Platforms: Certain simplification is achieved by choosing a DC electrostatic mode instead of a frequency-dependent AC electrostatic mode. To verify the feasibility of the DC electrostatic mode, we evaluate the electric potential drop across the double layer. If the potential drop is much smaller than that across the bulk solution at the working frequency of ~120 kHz, we may confirm that the application of an AC electrostatic mode is unnecessary. Accordingly, having the electric double layer modeled as a dielectric layer that is in series with the bulk solution also becomes redundant. Here we estimate the resistances and capacitances

across the pair of the electrode, as shown in Fig. 42. At 120kHz (the frequency of the maximum ACEO), the impedance of the double layer as a capacitor is about four orders of magnitude lower than the resistance of the bulk water.

The impedance of the double layer is:

$$\frac{1}{\omega C} = \frac{\lambda_D}{2\pi f \varepsilon_0 \varepsilon_m A} = \frac{200\text{nm}}{2 \cdot \pi \cdot 120\text{kHz} \cdot 8.854 \cdot 10^{-12}\,\text{F/m} \cdot 78 \cdot \text{A}} = \frac{3.8 \cdot 10^{-5}}{\text{A}}\,\Omega \cdot \text{m}^2$$

The resistance of the bulk water is:

$$R = \rho \frac{L}{A} = \frac{1}{1\mu\text{S/cm}} \frac{28\mu\text{m}}{A} = \frac{2.8 \cdot 10^{-1}}{A}\,\Omega \cdot \text{m}^2$$

where the Debye length λ_D = 200 nm (calculated in Section 4.3.1), ε_0 is the vacuum permittivity, ε_m is the relative permittivity of the double layer (at the DEP crossover frequency, we assume it is the same as the dielectric constant of water ε_w = 78), A is the side wall area of the electrodes, ρ is the resistivity of the bulk solution (reciprocal of conductivity, which we use 1μS/cm, falling in the range calculated in Section 4.3.1), and L = 28 μm is the gap distance between the electrode tips.

From the above calculations, we derive $R \gg \frac{1}{\omega C}$, so the voltage drop across the double layer is a negligible fraction of that across the bulk solution.

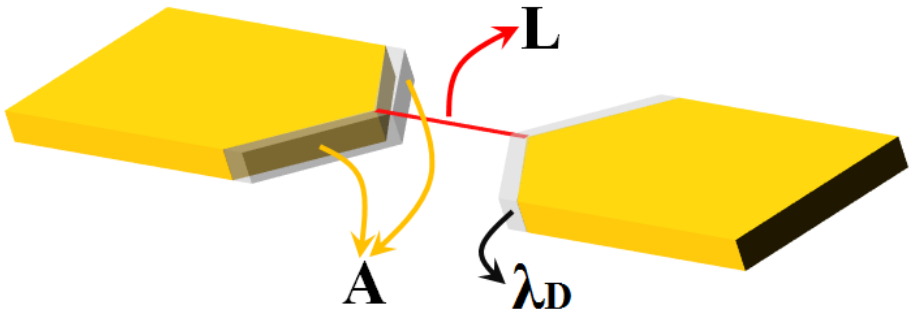

Fig. 42 Electric double layer as a dielectric layer

The electric double layer on the side the electrodes (yellow blocks) modeled as a dielectric layer that is in series with the bulk solution.

(2) Quantification of parameters/constants, including the vacuum permittivity $\varepsilon_0 = 8.854 \cdot 10^{-12}$ F/m and the Boltzmann constant $k_B = 1.38 \cdot 10^{-23}$ m^2 kg s^{-2}.

(3) Construction of geometrical designs: Due to the geometrical symmetry, a two dimensional simulation of the electric field distribution in the x-z plane is sufficient for later calculations of the Helmholtz-Smoluchowski velocity. We applied built-in CAD tools to draw a structure with four subdomains, as shown in Fig. 43. Two gold electrodes were graphed as rectangles with width of 100μm and thickness of 200nm. To avoid singularities in numerical calculations, rounded electrode tips with a curvature of 200nm were used, as shown in Fig. 44.

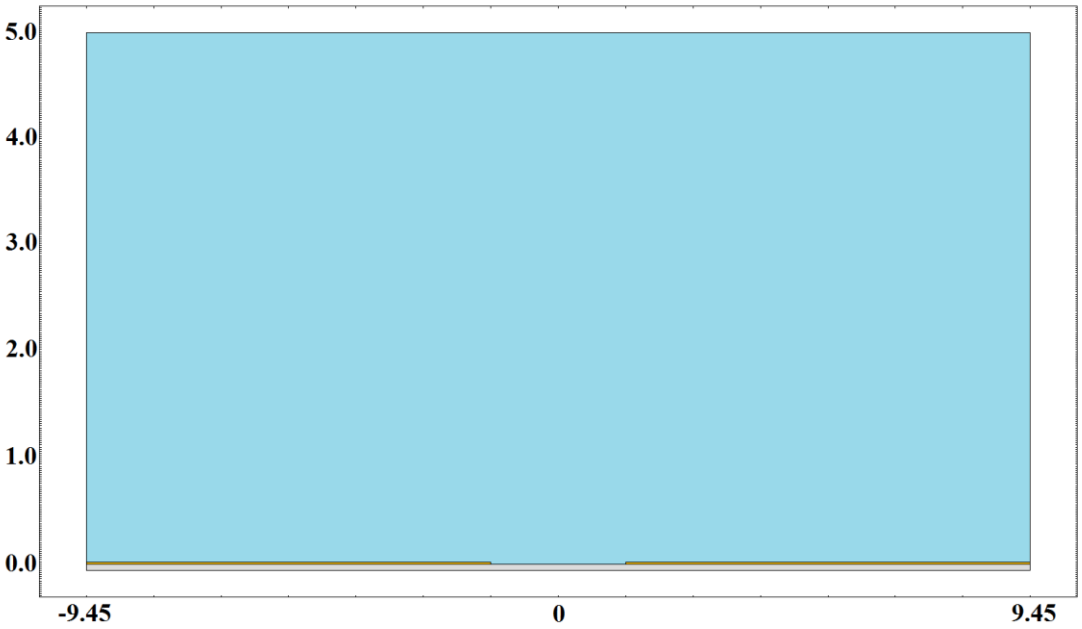

Fig. 43 Electrode chamber drawn with CAD

Four subdomains include the liquid medium (blue block), a pair of 200nm-thick gold electrodes (symmetric thin yellow stripes) and the glass substrate (grey stripe). Both the horizontal and vertical axes are scaled to $\times 10^{-5}$m.

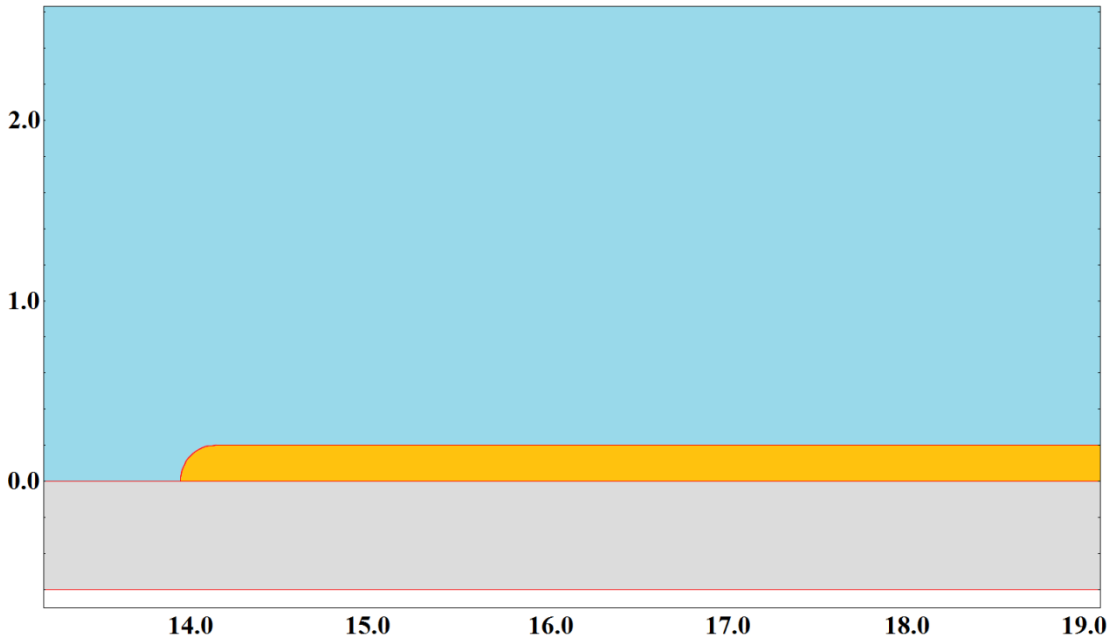

Fig. 44 The right planar electrode drawn with CAD

The right planar electrode with a curved tip. Three subdomains include the liquid medium (blue block), the right 200nm-thick gold electrode (yellow bar) and the glass substrate (grey block). Both the horizontal and vertical axes are scaled to $\times 10^{-6}$m.

(4) Definition of the boundary conditions: DC electrostatic boundaries were used to solve the electric field. Four types of boundary conditions, denoted by four colors, were applied to the interior and exterior boundaries, as shown in Fig. 45. An electric potential of $\mp$1.5 V was applied to the left and right gold electrodes. Zero charge was applied to the chamber's side, top, and bottom walls. A continuity boundary was applied to the gap area between the electrode tips.

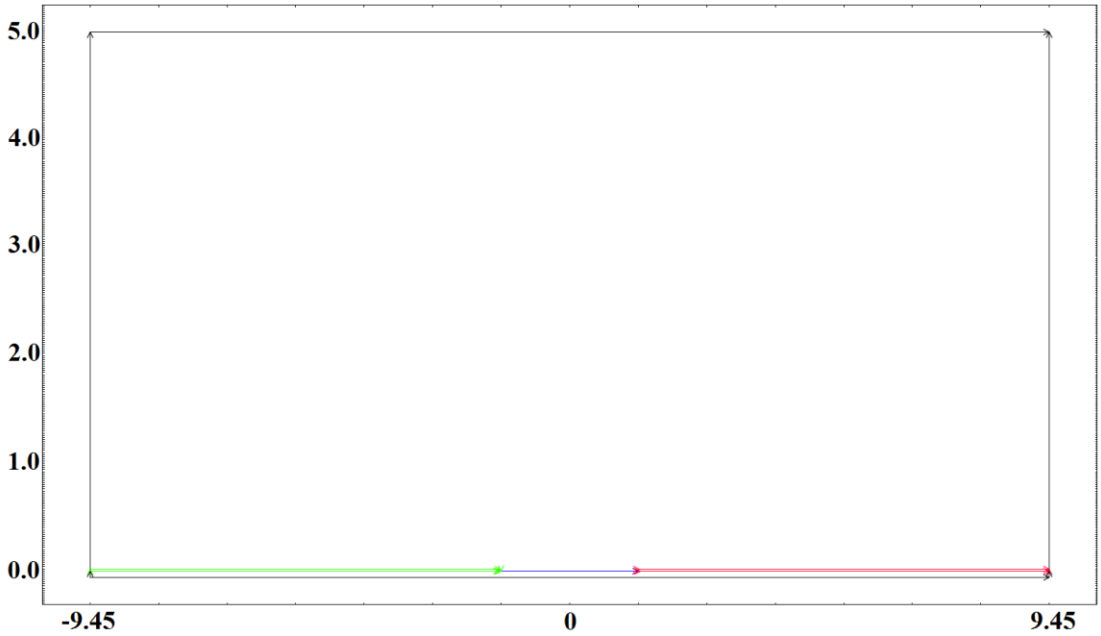

Fig. 45 Interior and exterior boundary conditions

Four types of boundary conditions include: zero charge/symmetry (black); -1.5V (Green); 1.5V (Red); Continuity (Blue). Both the horizontal and vertical axes are scaled to $\times 10^{-5}$m.

(5) Specification of subdomains: We specify the physical/material properties of four subdomains, by defining electric parameters of permittivity and conductivity. From the built-in material library, “gold” was assigned to the two electrodes, “water” to the solution, and “silica glass” to the substrate.

(6) Mesh and solve: Default/triangle-shaped meshing was initialized and then refined for all the four sub-domains, as shown in Fig. 46. Boundary meshing, which is capable of addressing extremities of the surface geometries, was applied to the top surface of the thin electrodes. The simulation of the electric field was solved in the two dimensional electrostatic mode. The x- and z- components of the electric field were extracted, as shown in Fig. 47 and Fig. 48.

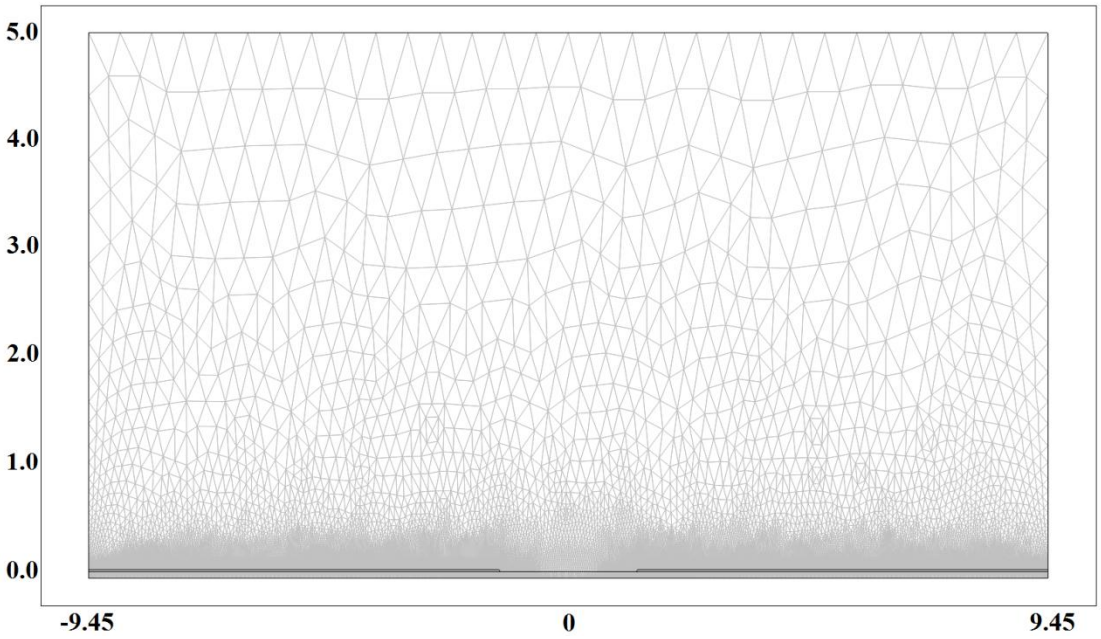

Fig. 46 Meshing of subdomains

Both the horizontal and vertical axes are scaled to $\times 10^{-5}$m.

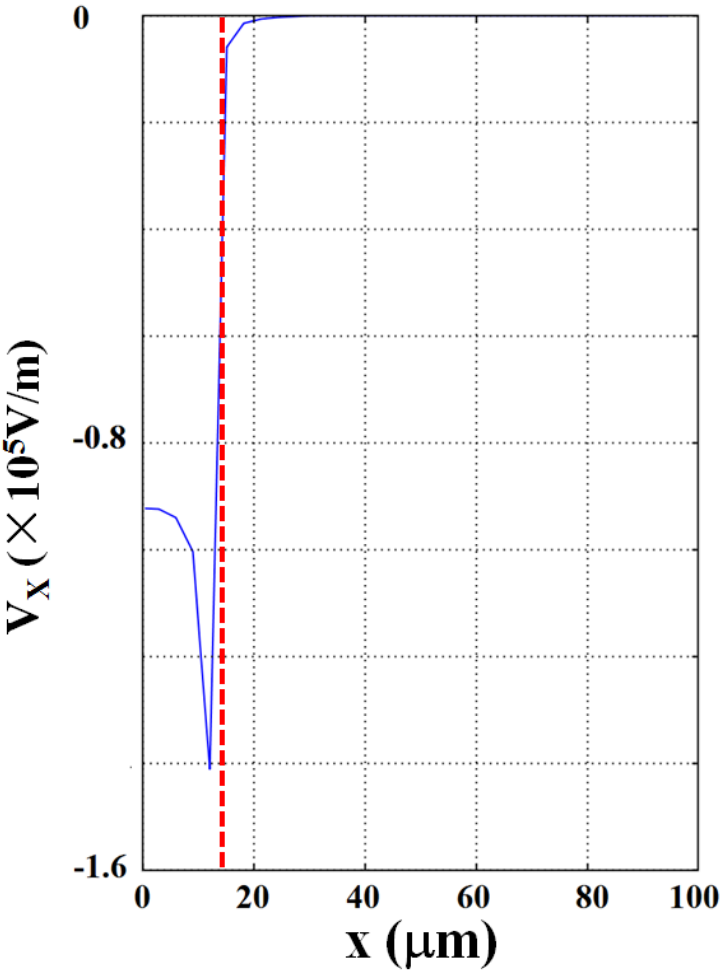

Fig. 47 Simulated x-component of the electric field

The x-component of the electric field as a function of x at z = 200 nm above electrode surface. The position of the right electrode tip is referenced by the red dashed line.

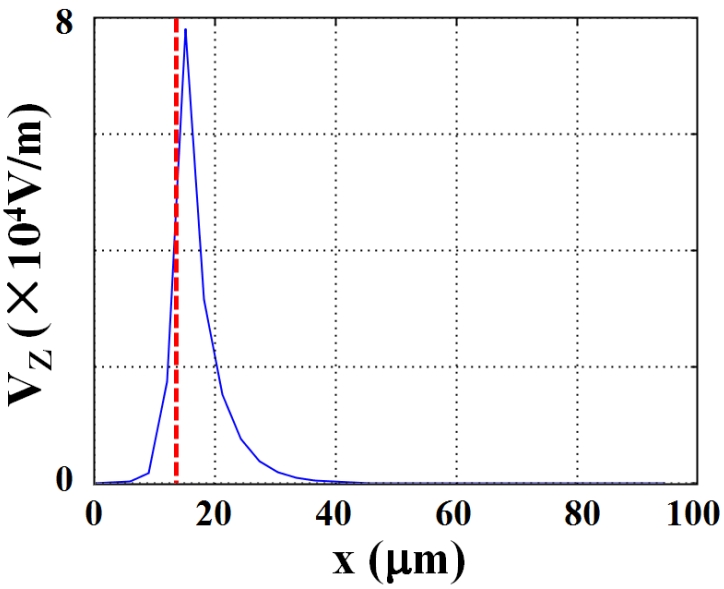

Fig. 48 Simulated z-component of the electric field

The z-component of the electric field as a function of x at z = 200 nm above electrode surface. The position of the right electrode tip is referenced by the red dashed line.

Appendix H

Initial number density of SWCNTs

A sufficiently high concentration of dispersed SWCNT in liquid suspensions was necessary to enhance the Raman signal. We evaluate the initial number of the SWCNTs within the optical tweezers' trapping volume. We start with the known densities of water and SWCNTs:

$$\rho_{water} = 1\text{g}/\text{cm}^3 \quad \text{and} \quad \rho_{SWCNT} = 1.3\text{g}/\text{cm}^3$$

We estimate the weight of a 500nm long (7,5) SWCNT.

The diameter of the (7,5) SWCNT is:

$$d_{SWCNT} = \frac{0.246\text{nm}}{\pi}\sqrt{n^2 + nm + m^2} = \frac{0.246\text{nm}}{\pi}\sqrt{7^2 + 7\cdot 5 + 5^2} = 0.82\text{nm}$$

The tube weighs:

$$W_{SWCNT} = \rho_{SWCNT} V_{SWCNT} = 1.3\text{g}/\text{cm}^3 \cdot 500\text{nm} \cdot \pi \cdot (\frac{0.82\text{nm}}{2})^2 = 1.7\cdot 10^{-19}\text{g}$$

For SWCNT suspensions with a w/v concentration of 0.0125 mg/ml, the number density is:

$$N_{SWCNT} = \frac{C_{SWCNT}}{W_{SWCNT}} = \frac{0.0125\text{mg}/\text{ml}}{1.7\cdot 10^{-19}\text{g}} \cong \boxed{7.3\cdot 10^{13}/\text{ml}}$$

The shape of an optical trap is often pictured as a prolate ellipsoid. For convenience we treat it as a sphere in calculating its volume. The beam width at the focal point is ~1μm, hence the radius of the sphere is ~0.5 μm:

$$V_{OT} = \frac{4}{3}\pi \cdot (0.5\mu\text{m})^3 = 0.52\cdot 10^{-12}\text{cm}^3$$

Therefore, the number of SWCNTs within the optical trapping volume is:

$$n_{SWCNT} = N_{SWCNT} \cdot V_{OT} = 7.3 \cdot 10^{13} / ml \cdot 0.52 \cdot 10^{-12} cm^3 \cong \boxed{38}$$

Appendix I

Specifics of SWCNT samples and Raman spectroscopy

Specific parameters of six samples of SWCNT suspensions, including electrical properties, major chiralities, concentration, dispersed surfactant and surfactant concentration are listed in Table 4. The exposure time for the Raman spectroscopy and the excitation power of the 633nm laser beam are listed in Table 5.

Sample	Electrical Property	Major Chiralities	SWCNT Concentration	Surfactant	DOC Concentration
1	Semiconducting	(7,6) (7,5)	0.25mg/ml 0.1875mg/ml 0.125mg/ml 0.075mg/ml 0.0375mg/ml	DOC	1%
2	Metallic		100%, 75%, 50%, 30%, 15%	DOC	1%
3	Semiconducting	(7,6) (7,5)	0.075mg/ml	DOC	0.6%, 1%, 2%, 3.1%
4	Metallic		50%	DOC	0.6%, 1.5%, 2.5%
5	Semiconducting	(7,6) (7,5)	100%, 50%, 40%, 28%, 16%	ssDNA	N/A

6	Metallic	(9,9) (10,10) (11,5) (14,2)	100%, 75%, 50%, 30%, 15%	ssDNA	N/A

Table 4 Specifics of the SWCNT suspension samples

Sample	Exposure Time (s)	Excitation Power (mW)
1	2	Min: 0.091, Max: 4.08
2	8	Min: 0.091, Max: 4.08
3	5	Min: 0.09, Max: 3.94
4	5	Min: 0.09, Max: 3.94
5	2	Min: 0.15, Max: 4.7
6	8	Min: 0.091, Max: 3.96

Table 5 Specifics of Raman spectroscopy

References

[1] H. Helmholtz, *Pogg. Ann.*, LXXXIX, 1853, 211.

[2] B. J. Kirby, *Micro- and Nanoscale Fluid Mechanics: Transport in Microfluidic Devices*, Cambridge University Press, 2010.

[3] G. Gouy, *Comt. Rend.*, 1909, 149, 654.

[4] G. Gouy, *J. Phys.*, 1910, 4, 9, 457.

[5] D. L. Chapman, *Phil. Mag.*, 1913, 6, 25, 475.

[6] O. Z. Stern, *Electrochem*, 1924, 30, 508.

[7] T. M. Squires, *Lab Chip*, 2009, 9, 2477-2483.

[8] W. B. Russel, D. A. Saville and W. R. Schowalter, *Colloidal Dispersions*, Cambridge University Press, 1989.

[9] T. B. Jones, *Electromechanics of Particles*, Cambridge: Cambridge University Press, 1995.

[10] H. A. Pohl, *Dielectrophoresis the behavior of neutral matter in nonuniform electric fields*, Cambridge University Press, 1978.

[11] M. Wei, J. Junio and H. Daniel Ou-Yang, *Biomicrofluidics*, 2009, 3, 012003.

[12] A. Ramos, H. Morgan, N. G. Green and A. Castellanos, *J. Colloid Interface Sci.*, 1999, 217, 420–422.

[13] H. Zhou and L. R. White, *J. Colloid and Interface Sci*, 2005, 285, 179-191.

[14] N. G. Green and H. Morgan, *J. Physics. D*, 1997, 30, 41-84.

[15] M. P. Hughes and H. Morgan, *J. Physics. D*, 1998, 31, 2205-2210.

[16] A. Rosenthal and J. Voldman, *Biophysical Journal*, 2005, 88, 2193-2205.

[17] L. Wang and A. P. Lee, *Material Research Society Symposium Proceedings*, 2007, 1004.

[18] H. Morgan and M. P. Hughes, *Biophysical Journal*, 1999, 77, 516-525.

[19] N. Lewpiriyawong and C. Yang, *Biomicrofludics*, 2008, 2.

[20] M. Lian and N. Islam, *J. Physics: Conference Series 34*, 2006, 589-594.

[21] P. Chiou and A. T. Ohta, *J. Microelectromechanical Sys.*, 2008, 17, 3.

[22] M. R. Bown and C. D. Meinhart, *Microfluid Nanofluid*, 2006, 2, 513-523.

[23] S. V. Rotkin, *Applied Physics of Carbon Nanotubes*, Springer, 2005.

[24] L. Dong, et al., *J. Phys. Chem. B*, 2005, 109.

[25] Retrieved April 16, 2012, from http://www.freepatentsonline.com/7074310.html

[26] A. Ashkin, *Phys. Rev. Lett.*, 1970, 24, 4, 156–159.

[27] J. R. Moffitt, Y. R. Chemla and D. Izhaky, C. Bustamante, *Proc. Natl. Acad. Sci. U.S.A.*, 2006, 103, 24, 9006–9011.

[28] B. C. Gierhart, D. G. Howitt, S. J. Chen, R. L. Smith and S. D. Collins, *Langmuir*, 2007, 23,

12450-12456.

[29] A. Jamshidi, P. J. Pauzauskie, P. J. Schuck, A. T. Ohta, P. Chiou, J. Chou, P. Yang and M. C. Wu, *Nature Photonics*, 2008, 2.

[30] H. Hwang, Y. H. Park and J. K. Park, *Langmuir*, 2009, 25, 6010–6014.

[31] R. Hölzel, N. Calander, Z. Chiragwandi, M. Willander and F. F. Bier, *Phys. Rev. Lett.*, 2005, 95, 12810.

[32] N. G. Green and H. Morgan, *J. Phys. Chem. B*, 1999, 103, 41-50.

[33] T. Honegger, K. Berton, E. Picard and D. Peyrade, *App. Phys. Lett.*, 2011, 98, 181906.

[34] J. Happel and H. Brenner, *Low Reynolds Number Hydrodynamics*, Dordrecht: Kluwer, 1991.

[35] G. Schwarz, *J. Phys. Chem.*, 1962, 66, 2636-2642.

[36] H. Park, M. Wei, and H. D. Ou-Yang, *Electrophoresis*, in press.

[37] S. Debesset, C. J. Hayden, C. Dalton, J. C. T. Eijkel and A. Manz, *Lab Chip*, 2004, 4, 396-400.

[38] Robert G. Mortimer, *Physical Chemistry*, Academic Press, 2000.

[39] M. Z. Bazant, M. S. Kilic, B. D. Storey and A. Ajdari, *Advances in Colloid and Interface Science*, 2009, 152, 48-88.

[40] P. Garcı´a-Sa´nchez, A. Ramos, N. G. Green and H. Morgan, *Langmuir*, 2008, 24, 9361-9369.

[41] R. W. Clarke, J. D. Piper, L. Ying and D. Klenerman, *Phys. Rev. Lett.*, 2007, 98, 198102.

[42] S. Wang, H. Chen and H. Chang, *Biomicrofludics*, 2007, 1, 034106.

[43] N. G. Green, A. Ramos, A. Gonza´lez, H. Morgan, and A. Castellanos, *Phys. Rev. E*, 2002, 66, 026305.

[44] A. Ural, Y. Li, and H. Dai, *Appl. Phys. Lett.*, 2002, 81.

[45] C. Park, J. Wilkinson, S. Banda, Z, Ounaies, K. E. Wise, G. Sauti, P. T. Lillehei, and J. S. Harrison, *Journal of Polymer Science: Part B: Polymer Physics*, 2006, 44, 1751.

[46] T. Rodgers and S. Shoji, *Phys. Rev. Lett.*, 2008, 101.

[47] G. S. Duesberg, I. Loa, M. Burghard, K. Syassen, and S. Roth, *Phys. Rev. Lett.*, 2000, 85, 5436.

[48] R. B. Weisman and S. M. Bachilo, *Nano Lett.*, 2003, 3, 1235.

[49] J. Junio, J. Ng, J. A. Cohen, Z. Lin, and H. D. Ou-Yang, *Optical Letter*, 2011, 36, 1497.

[50] F. Hofmeister, *Arch. Exp. Pathol. Pharmacol.*, 1888, 24, 247-260.

[51] Y. Zhang and P. S. Cremer, *Current Opinion in Chemical Biology*, 2006, 10, 6, 658-663.

[52] A. Di. Biasio, L. Ambrosone and C. Cametti, *Biophysical Journal*, 2010, 99, 163-174.

[53] C. T. O'Konski, *J. Phys. Chem.*, 1960, 64, 605.

CURRICULUM VITAE

Jingyu Wang
116 E 4th ST 2F, Bethlehem PA 18015, USA
(610) 573-8157 rosette.wang@gmail.com

EDUCATION

08/2007 –08/2012	Ph.D., Department of Physics, Lehigh University, Bethlehem, PA, GPA: 3.9/4.0
09/2003 – 06/2007	B.S., Department of Microelectronics, Fudan University, Shanghai, China, GPA: 3.2/4.0

SKILLS

Technique	COMSOL Multiphysics, Labview, Microfluidic/Electrode Chamber Design/Fabrication, Photolithography, Raman Spectroscopy, Confocal Microscopy, Lock-in Phase Sensitive Detection
Computer	OrCAD, Visual Basic, C++, FPGA, Microsoft Office (Word, Excel, Powerpoint), Origin, Unix/Linux
Language	Chinese, English, Japanese

AWARDS

09/2011 – 09/2012	Honorary Sherman Fairchild Fellowship (Lehigh University, Bethlehem, PA)
09/2009 – 09/2011	Sherman and Fairchild Fellowship (Lehigh University, Bethlehem, PA)
09/2007 – 08/2012	Teaching/Research Assistantship (Department of Physics, Lehigh University, Bethlehem, PA)
02/2004 – 02/2005	Most Valuable Society: IV-Star Prize (Fudan University, Shanghai, China)

ACADEMIC EXPERIENCE

Lehigh University, Bethlehem, PA

05/2008 – present ***Optical Trapping and Manipulation of Single-Walled Carbon Nanotubes***

Developed a highly flexible micromanipulation technique of Single-Walled Carbon Nanotubes in liquid suspensions by use of a highly focusing laser beam. Carbon nanotubes that are mass manufactured in a mixture of different chiralities (electrical properties) are thus able to be selectively concentrated and orientated with great convenience in the optical field for further applications as building blocks for nanoelectronics.

05/2009 – 01/2011 ***Mapping AC Electroosmotic Flow at the Dielectrophoresis Crossover Frequency of a Colloidal Probe***

Developed a technique of mapping the AC electroosmotic flow field with high spatial resolution and selectivity against coexisting electrokinetics. The technique helps to reconcile the disagreement between the existing theory and previous experiments of AC electroosmosis, and guide future designs of efficient ACEO-based micropumping devices.

02/2009 – 01/2011 ***Low-frequency Dielectrophoretic Response of a Single Particle in Aqueous Suspensions***

By discovering the dielectrophoresis crossover frequencies of colloidal particles, we studied the interaction of the electrical double layer outside colloidal particles in aqueous suspensions with an electric field. The knowledge ma allow us to apply a very small voltage and noninvasively separate particles of different properties (size, material, surface charge) by exerting attractive forces on some and repulsive forces on the rest.

Fudan University, Shanghai, China

02/2007 – 06/2007 ***Fabrication of Conductive Glue Based Nanoimprint Technique Using SU-8 Photoresist***

Fabricated thin film electrodes with negative photoresist doped with silver nanoparticles by use of the simple and low-cost technique of Nanoimprint.

East China University of Science and Technology, Shanghai, China

07/2005 – 09/2006 ***Electric Conductivity of (0.4-x)P_2O_5-Fe_2O_3-PbO Semiconducting Glass***

Studied semiconducting glass's conductivity as a function of glass compositions, redox number and melting temperature, in order that the type of glass is effectively applied in fiber optics such as microchannel plate applications.

SELECTED CONFERENCE PRESENTATIONS

Optical Trapping and Manipulation of Single-Walled Carbon Nanotubes

03/2011 2012 APS March Meeting, Boston, MA

Mapping AC Electroosmotic Flow at the Dielectrophoresis Crossover Frequency of a Colloidal Probe

10/2011 2011 AIChE Annual Meeting, Minneapolis, MN

10/2011 83rd Annual Meeting of the Society of Rheology, Cleveland, OH

08/2010 2010 SPIE Optics + Photonics, San Diego, CA

Low-frequency Dielectrophoretic Response of a Single Particle in Aqueous Suspensions

10/2011 2011 AIChE Annual Meeting, Minneapolis, MN

03/2011 2011 APS March Meeting, Dallas, TX

LEADERSHIP & MEMBERSHIP

07/2011 – present	American Institute of Chemical Engineers / Member
07/2011 – present	Society of Rheology / Member
03/2009 – present	American Physical Society / Member
06/2006	3rd International Copper Interconnect and Related Technology Symposium, Shanghai, China / Student Volunteer
02/2004 – 02/2005	Astronomy Society, Fudan University, Shanghai, China / President Organized astronomical observations on and off campus. Raised total funds of $1400 from college, astronomical observatory and local industries.

PUBLICATIONS

- Low-frequency Dielectric Response of a Single Particle in Aqueous Suspensions (Jingyu Wang, H. Daniel Ou-Yang, in preparation, 2012)
- Mapping AC Electroosmotic Flow at the Dielectrophoresis Crossover Frequency of a Colloidal Probe (Jingyu Wang, Ming-Tzo Wei, H. Daniel Ou-Yang, in preparation, 2012)
- Optical Tweezers as a Force Sensor for Separating Dielectrophoresis and AC Electroosmosis Forces (Jingyu Wang, H. Daniel Ou-Yang, SPIE Proceedings, 7762, 2010)
- Study on the Electric Conductivity of PbO-Fe_2O_3-P_2O_5 Semiconducting Glass (Zhongjian Wang, Bo Jiang, Jingyu Wang and Zhaodi Jin, Glass and Enamel, 34, 2006)

TEACHING EXPERIENCE

Lehigh University, Bethlehem, PA

09/2007 – present	Full time physics lab instructor: General Physics Experiments Full time recitation instructor: General Physics Summer REU (Research Experiences for Undergraduates) instructor: Biophysical Projects

East China University of Science and Technology, Shanghai, China

06/2001 – 08/2001	Part time Chinese teacher: Chinese language/culture

REFERENCES

H. Daniel Ou-Yang
Professor, Department of Physics, Lehigh University
206 Fairchild Laboratory, Bethlehem PA 18015
(610) 758-3920
hdo0@lehigh.edu

Volkmar Dierolf
Professor and Chair, Department of Physics, Lehigh University
209 Fairchild Laboratory and 214 Lewis Laboratory, Bethlehem PA 18015
(610) 758-3915
vod2@lehigh.edu